6-17-2021

Investigation of single, binary, and ternary metal oxides of iridium, rhodium, and palladium for neural interfacing applications

Gregory Vincent Taylor
Rowan University

Recommended Citation

Taylor, Gregory Vincent, "Investigation of single, binary, and ternary metal oxides of iridium, rhodium, and palladium for neural interfacing applications" (2021). *Theses and Dissertations.* 2918.
https://rdw.rowan.edu/etd/2918

INVESTIGATION OF SINGLE, BINARY, AND TERNARY METAL OXIDES OF IRIDIUM, RUTHENIUM, RHODIUM, AND PALLADIUM FOR NEURAL INTERFACING APPLICATIONS

by

Gregory Vincent Taylor

A Dissertation

Submitted to the
Department of Physics and Astronomy
College of Science and Mathematics
In partial fulfillment of the requirement
For the degree of
Doctor of Philosophy in Materials Science and Engineering
at
Rowan University
May 7, 2021

Dissertation Chair: Jeffrey Hettinger, Ph.D.

Committee Members:
Wei Xue, Ph.D.
Lei Yu, Ph.D.
Samuel Lofland, Ph.D.

Dedications

In loving memory of my mother and father, Ruth, and Ernest Taylor.

Acknowledgments

I thank those who supported, assisted, and believed in me during my four years of pursuing my Ph.D. at Rowan University.

Chiefly I would like to thank my advisor, Professor Jeffrey Hettinger, for his belief and confidence in me, willingness to guide and mentor me, patience, creativity, and his sense of humor. My research trajectory has been shaped and guided by his expert mentorship, and without him I would not be writing this today.

I thank Johnson Matthey Inc. for providing me with funding for my Ph.D. through the Johnson Matthey Materials Science Graduate Assistantship.

I thank Dr. Shahram Amini, whose expertise, guidance, and vision as a businessman and a scientist helped secure my graduate studies and the research presented in this thesis.

I am grateful to my thesis committee members Professor Lei Yu, Professor Wei Xue, and Professor Samuel Lofland for their guidance, support, and encouragement.

I would like to give a special thanks to our close collaborators from Johnson Matthey including Saxon Tint, Hugh Hamilton, Andy Fones, and Ludovic Briquet for their expert insight, feedback, and the many fruitful discussions.

I acknowledge the assistance of the instrument coordinators Carl A. Lunk, and Dr. Ted Scabarozi Jr.

Abstract

Gregory Vincent Taylor
INVESTIGATION OF SINGLE, BINARY, AND TERNARY METAL OXIDES OF IRIDIUM, RUTHENIUM, RHODUIM, AND PALLADIUM FOR NEURAL INTERFACING APPLICATIONS
2020-2021
Jeffrey Hettinger, Ph.D.
Doctor of Philosophy

In this thesis, thin film single, binary, and ternary metal oxides of iridium (Ir), ruthenium (Ru), rhodium (Rh), and palladium (Pd) were synthesized for use as electrode/microelectrode coatings for neural interfacing applications using DC reactive magnetron sputtering. Synthesis conditions which enhanced the electrochemical properties of films as measured by cyclic voltammetry and electrochemical impedance spectroscopy in a phosphate buffered saline solution of the single metal oxides were identified to be 30 mTorr working pressure, 20% oxygen partial pressure, and cathode power densities ≤ 4.9 W/cm^2. These parameters were then used to develop the binary and ternary metal oxide films. The binary metal oxides studied included $Ir_{(1-x)}M_x$ where M = Pd, Rh, Ru, and the ternary metal oxides studied included $Ir_{(1-x-z)}M_xM'_z$, where M,M´ = Pd, Rh, and Ru. The binary metal oxide concentrations which produce robust microstructures and exceptional electrochemical performance have been identified to be $x \geq 0.5$ for $Ir_{(1-x)}Rh_xO_y$, $x \geq 0.34$ for $Ir_{(1-x)}Ru_xO_y$, and $x \geq 0.14$ for $Ir_{(1-x)}Pd_x O_y$. Similar compositional regions have been identified for the ternary metal oxide systems, these include $x \geq 0.16$ and $z \geq 0.05$ for $Ir_{(1-x-z)}Pd_xRu_zO_y$, $x \geq 0.13$ and $z \geq 0.04$ for $Ir_{(1-x-z)}Pd_xRh_zO_y$, and $x \geq 0.23$ or $z \geq 0.50$ for $Ir_{(1-x-z)}Ru_xRh_zO_y$.

Table of Contents

Table of Contents (Continued)

Table of Contents (Continued)

Table of Contents (Continued)

Table of Contents (Continued)

List of Figures

List of Figures (Continued)

List of Figures (Continued)

List of Figures (Continued)

List of Figures (Continued)

List of Figures (Continued)

List of Figures (Continued)

List of Figures (Continued)

List of Figures (Continued)

List of Tables

Table Page

List of Tables (Continued)

Table Page

Chapter 1

Introduction

Materials science and engineering (MSE) is a discipline that is intimately connected with the technological progression of mankind. Historical terms which highlight technological progress such as the “Bronze Age” (3500 BCE) which demarks the use of Cu-Sn alloys to develop harder tools and weapons or the “Iron Age” (1500 BCE) in which further progression was achieved through the use and alloying of Fe and Fe-based compounds to create even stronger tools resulting in even greater changes to society are a few such examples. Regardless of the era, it is clear that materials science and engineering plays a pivotal role in the advancement of human civilization.

Materials science involves the investigation and classification of the relationship between the structure and properties of a material while materials engineering involves the design or engineering of material structures to exhibit certain desired properties. The scope of material structures ranges from subatomic such as electronic structure, to atomic which includes arrangements of atoms, to micro and macroscopic structures *i.e.*, those that can be observed with a microscope device or with the naked eye. Material properties on the other hand, can be characterized into seven categories. These include biological, mechanical, electrical, magnetic, optical, thermal, and chemical. In addition to the structure-property relationships, the synthesis and performance of materials are also critical components to MSE. Thus, the discipline of MSE can be wholly defined as the interrelationship between the process, structure, properties, and performance of materials (Fig. 1.1).

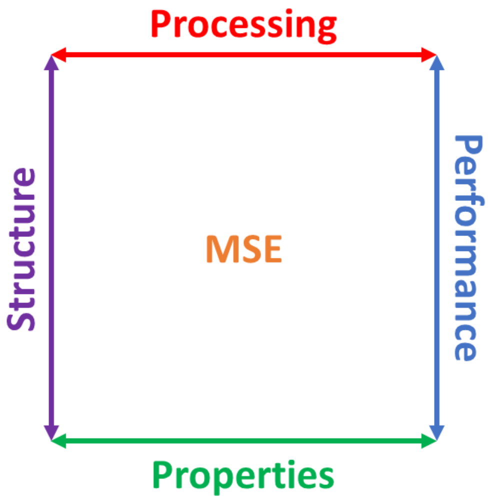

Figure 1.1. The four characteristics which define materials science and engineering and their interrelationship.

1.1 Ceramics

Ceramics are compounds that are often but are not limited to materials consisting of one or more metallic elements and one or more non-metallic elements. These materials include but are not limited to oxides, nitrides, carbides, and sulfides. The bonding of ceramic materials ranges from ionic to fully covalent or a combination of both. More often ceramics bond ionically with the metallic atom acting as the cation (positive charge) and the non-metallic atom acting as the anion (negative charge). The crystal structure of ceramics must obey the law of neutrality (the crystal structure must be electrically neutral); thus, the oxidation states and the relative sizes of the cations and anions will influence the crystal structure to meet this criterion.

The properties of ceramic compounds are dictated by their constituent elements and the types of bonding that occur. For instance, bulk ceramics are brittle due to the strength of ionic and covalent bonds which is in contrast to metals which tend to be more ductile due to the comparatively weak metallic bond strengths. In addition to brittleness, ceramic compounds are likely to possess characteristics such as transparency, chemical durability, hardness, high melting point, and under most circumstances, these materials are electrically and thermally insulating. Some exceptions to these characteristics exist such as those observed in perovskites (14,15), MAX phase carbides and nitrides (16–18), and solid catalysts (19,20).

1.2 Thin Films

Thin films are materials that can range from a few nanometers to several microns thick and act as an intermediary between monolayer and bulk properties and are utilized in a variety of applications which include those shown in Table 1.1. Thin films can be defined in many ways. Some constraints include having a high surface to volume ratio, possessing material properties that are volume dependent, as well as possessing surface and near surface properties that may deviate substantially from their bulk counterparts. Additional differences in thin films from their bulk counterparts result from the non-equilibrium conditions common during synthesis which can lead to the growth of metastable structures with unique and unusual properties not achievable in bulk materials. Unlike bulk solids which have consistent properties throughout their volume, the aforementioned surface and near surface properties of thin films can be tuned through alteration of synthesis parameters such as background pressure, gas and impurity concentrations, particle energies, substrate temperature, material, and orientation, as well as a host of other parameters. As a consequence, the material properties of thin films can be engineered with relative ease to meet specific design criteria with high reproducibility.

Table 1.1

Thin Film Properties and Applications

Thin Film Property	Applications
Biological	Osteointegration, Fibrointegration, Anti-fouling
Electrical	Insulation and Conduction, Photo and Piezoelectric, Semiconductors
Magnetic	Data Storage, Antennas
Mechanical	Tribological, Hardness, Adhesion, Tolerance, Micromechanics
Thermal	Thermocouple sensors, Heat Sinks, Thermal Barriers
Chemical	Catalysis, Electrocatalysis, pH Sensors, Corrosion Resistance
Optical	Reflection/Anti-reflection, Optical Interference, Optoelectronics

1.3 Neural Interfacing Devices

Neural interfacing devices can broadly be defined as devices which are able to record or modulate electrophysiological information by directly interfacing with neural tissues via an electrode-tissue interface. A depiction of the electrode-tissue interface interaction is provided in Fig. 1.2 (21,22). Generally, devices that measure or monitor neuronal signals in the body are referred to as recording devices while devices which inhibit or stimulate neuronal signals in the body are referred to as neurostimulation devices. Implantable neural interfacing devices are utilized in a wide range of applications including but not limited to the investigation of neuronal signals in the brain with high spatial resolution to better understand and diagnose neurological diseases and disorders (23–25), cardiac modulation and defibrillation through cardiac stimulation and sensing (26–31), robotic limb control and restoration of motor function through recording and transmittance of neural signals from the motor cortex to prosthetic devices (24,32–36), treatment of chronic pain through spinal cord and peripheral nerve stimulation (37–40), treatment of diseases such as Parkinson’s and epilepsy through vagus nerve via deep brain stimulation (41–47), as well as sensory restoration through the use of cortical and cochlear neuroprosthetic implants (48–51).

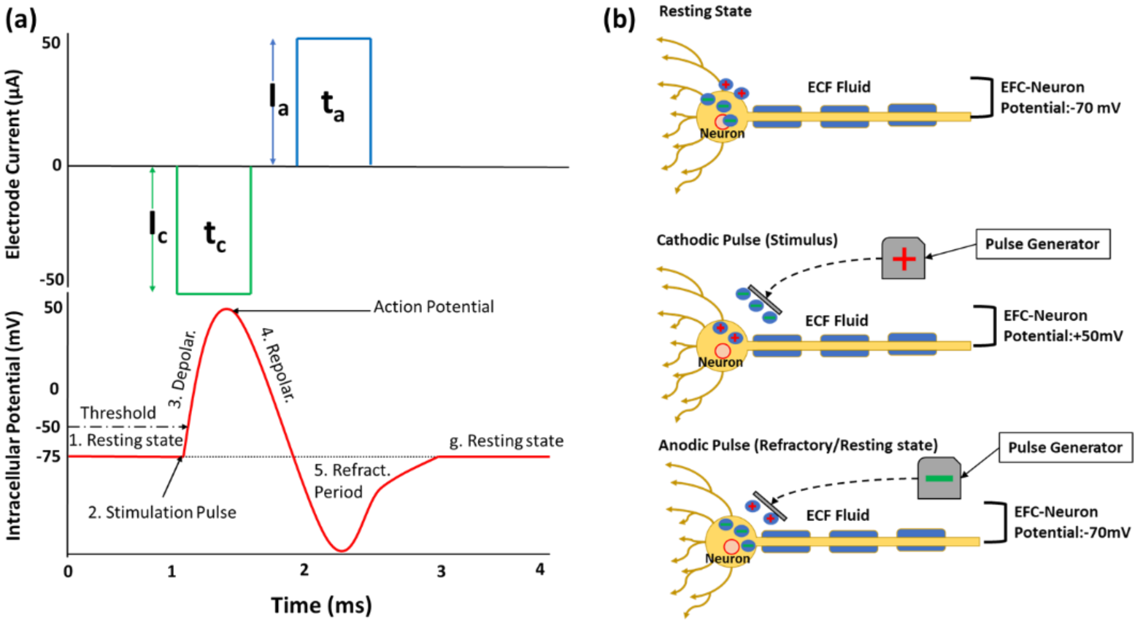

Figure 1.2. (a) Schematic of a pulse waveform for a stimulation pulse in tissue from an electrode to neuronal tissue (b) Neuron polarization/depolarization response to a neurostimulation pulse.

1.3.1 Electrode Materials

Electrode materials, due to their role in directly interacting with neural tissue (through either modulation or recording of neural signals), must be selected carefully to ensure that no irreversible damage occurs to the tissue or electrode while implanted(21,52–55). Thus, to ensure long-term efficacy of devices, electrode materials must be biocompatible to reduce the occurrence of fibrotic encapsulation. Otherwise performance will be reduced over time due to the insulative nature of the fibrous capsule, or, in some circumstances may result in implant rejection (56–60). Another important factor is the chemical stability of electrode materials (corrosion resistant). This characteristic is important in sustaining electrode electrical properties as well as minimizing the generation of toxic metal ions in the body which can lead to large scale inflammation (61–63). Some additional considerations include having good mechanical properties such as compliance and adhesion to ensure electrodes can be handled and implanted without loss of functionality, good electrical conductivity, and excellent reduction-oxidation (redox) stability to ensure long-term charge injection capabilities (52,53,64). As shown in Table 1.2 many metals and alloys have been evaluated for use as electrode materials. Among the materials tested, those that match closely with the aforementioned criteria are the heavier transition metals such as gold (Au) (65–67), platinum (Pt) (68–70), iridium (Ir) (71), and alloys such as Pt-10%Ir (53,72,73).

No material exchanges charge strictly through faradaic or double layer mechanisms. Instead one mechanism (though not always the case) will dominate depending on reaction rate, potential window, structure, and chemical stability of the electrode material (74–77). Noble metal materials are able to inject charge primarily through faradaic redox reactions with small contributions from a pseudo-double layer related to ion confinement and diffusion at the surface (22,64,78). Non-noble metals such as stainless steel, nickel chromium, and titanium, due to their comparatively slower faradaic processes, primarily exchange charges through pseudo-double layer capacitance via adsorption and desorption of a counter-ion monolayer (53,55). Regardless of the type of metal, electrode dissolution can occur wherein oxidized metal ions at the surface will diffuse away before they are reduced and redeposited back on the interface which can reduce performance and cause harm to surrounding tissue over time (79). This effect is much stronger in the non-noble metals and alloys, as a consequence they’re used on much shorter time scales.

Table 1.2

Neural Interfacing Electrode Materials

Electrode Material	Suitability	Failure Mechanism
Gold	Suitable	Corrosion (very long time scale)
Iridium	Suitable	Corrosion (long time scale)
Platinum	Suitable	Corrosion (long time scale)
Tungsten	Suitable (short term)	Corrosion
Tantalum	Suitable (short term	Corrosion
Titanium	Suitable (short term)	Corrosion
Copper	Unsuitable	Corrosion/Necrotic/Inflammatory
Silver	Unsuitable	Corrosion/Necrotic/Inflammatory
Iron	Unsuitable	Corrosion/Necrotic/Inflammatory
Nickel	Unsuitable	Corrosion/Necrotic/Inflammatory
Platinum-10% Iridium	Suitable	Corrosion (long time scale)
Platinum-8% Tungsten	Suitable	Corrosion (long time scale)
Platnium-10% Rhodium	Suitable	Corrosion (long time scale)
Stainless Steel	Suitable (short term)	Corrosion
Nichrome	Suitable (short term)	Corrosion

The trajectory for further refinement of neural interfacing devices is in large part predicated on increased miniaturization of devices and electrodes which enable higher spatial resolution, precision, and reliability (21,52); these characteristics are particularly important in improving operation and efficacy of neuroprostheses which require single unit (recording of one type of neuronal cell) or multi-unit (simultaneous recording of two or more types of neuronal cells) recordings of neuronal cells (80–82). Additionally, increased miniaturization of neural interfacing electrodes and devices will further reduce trauma in patients during implantation leading to faster recovery times, a lowered risk of infection, and improved quality of life. To this end, bare metal electrodes are effective in applications not constrained by larger electrode geometric surface areas (GSA) or lower charge injection limits (83–85). However, they lack the charge injection and low impedance characteristics necessary to operate as microelectrodes without exceeding the potentials and currents where water electrolysis can occur (water window) which can cause irreversible damage to itself and/or the surrounding neural tissue (62,63).

1.3.2 Electrode Coatings

The ideal electrode/microelectrode coating possesses properties such as high charge storage capacity (CSC), high charge injection (Q_{inj}), low interface (electrode-tissue) impedance, a high electrochemically available surface area (ESA) to GSA ratio, excellent redox and chemical stability, excellent biocompatibility, mechanical stability, as well as the ability to be deposited on nearly any type of electrode regardless of shape, size, or electrode material. In an effort to match these criteria many materials (Table 1.3) have been investigated for use as electrode and microelectrode coatings. Platinum group metal (PGM)-based electrode coatings are often used due to their pseudocapacitive charge exchange mechanisms which allow for high charge injection, making them useful for interfacing with neural tissues which have high dielectric constants and threshold voltages (84,85), such as those found in the brain, as well as applications which require high specificity (microelectrodes/neuroprosthetics) when interfacing with neural tissue. Typical PGM-based electrode coatings include ceramics such iridium oxide (IrO_x) (71,86–88) and more recently ruthenium oxide (RuO_x) (89–91) thin films, as well as high surface area metals such as porous platinum and platinum black (92,93). For applications where tissue requires lower charge injection such as cardiac sensing and pacing, films which utilize double layer capacitance (effectively no chemical reaction) are utilized. Typical materials include fractal zirconium (ZrN) and titanium nitrides (TiN) due to their chemical and mechanical stability, high charge storage, and high ESA (low impedance). In addition, non-ceramic and non-metallic materials have been investigated including conductive polymers such as poly(3,4-ethylene dioxythiophene)(PEDOT) (94) and polypyrrole (PPy) (95,96), and various carbon allotropes (25,97,98).

Table 1.3

Typical Neural Interfacing Electrode Coatings

Electrode Material	Primary Charge Exchange Mechanism
Iridium Oxide	Pseudocapacitive
Ruthenium Oxide	Pseudocapacitive
Porous Platinum	Faradaic
Platinum Black	Faradaic
Titanium Nitride	Double Layer
Zirconium Nitride	Double Layer
PEDOT (doped)	Pseudocapacitive
Polypyrrole	Faradaic
Carbon (graphene, CNT)	Faradaic

1.4 Motivation and Objectives

The treatment of many neurological diseases and disorders are traditionally achieved through the use of pharmaceuticals and major surgery. The use of pharmaceuticals is appealing due the diverse number of drugs that are available in the treatment of a wide range of conditions, the relative ease of intake by the patient, and the relative ease of production. However, pharmaceuticals lack specificity in their treatment and can become less effective over time due to drug tolerance development (99). Additionally, pharmaceuticals can come with many peripheral and downstream adverse effects on immune, pulmonary, cardiac, and sexual function (100–103). Furthermore, extended use can also result in insomnia, depression, fatigue, and dependency development which can lead to overdose. On the other hand, major surgical treatments while necessary in some circumstances can often be very traumatic to the body and comes with a greater risk of infection. Moreover, this treatment option often requires the use of pharmaceuticals to assist in the long recovery times needed to restore quality of life. When compared to more traditional methods of treatment, implantable neural interfacing devices supplant many pharmaceuticals and major surgical treatments due to their high specificity and efficacy which minimize or outright eliminate many of the peripheral and downstream effects associated with pharmaceuticals. These devices often require only minimally invasive implantation leading to shorter recovery times and reduced risk of infection, and because of their method of operation, negative effects such as dependence or treatment tolerance are not present granting long term efficacy via chronic implantation.

As previously mentioned, the continued advancement of implantable neural interfacing devices is in large part predicated on the development of materials that enhance communication between the tissue-electrode interface and thereby increase miniaturization. The investigation of new platinum group metal oxides for neural interfacing applications has been limited to primarily IrO_x and more recently RuO_x (89–91). IrO_x coatings have been extensively investigated due to their excellent charge exchange characteristics, biocompatibility, and chemical stability. Cogan *et al.* has studied various types of IrO_x, including electrodeposited and sputtered IrO_x thin films, based on earlier work by Kang *et al.*(22,104–106). While others have explored thermally prepared IrO_x thin films (86,107,108). Wessing *et al.* describes the use of RF sputtering and synthesis pressure dependence on IrO_x thin films in his thesis (109), while Chen *et al.* details the use of chemical bath deposition (88). The numerous fabrication methods for IrO_x have been thoroughly detailed by Jang and Lee (87) in their review. Among the methods of synthesis, reactive magnetron sputtering stands out due to excellent coating uniformity, the high degree of control of deposition parameters, and repeatability, making it the dominant synthesis method for neural interface coating fabrication. Synthesis methods for RuO_x on the other hand have not been as extensively investigated for neural interfacing purposes though Atmaramani *et al.* and this author both have used reactive magnetron sputtering to create RuO_x thin film coatings (89,90).

The properties of IrO_x including biocompatibility, stability, and degradation have been intensively investigated. Maeng *et al.* studied the cytotoxicity of neuronal cells in a viability assay (110), while Gobbels *et al.* performed a similar viability assay with a different polymorph of IrO_x (81). Additional *in-vitro* tests performed by Cogan *et al.* were also performed which investigated two different physiological electrolytic solutions, as well as *in-vitro* comparisons of charge injection limits of Pt and IrO_x microelectrodes (22), while Negi *et al.* performed a similar investigation of charge injection capacity *in-vitro* of platinum and iridium oxide microelectrodes (111). The breadth of *in-vitro* and *in-*

vivo investigations of IrO_x is vast, with many studies demonstrating the longevity and biocompatibility of the compound. For these reasons, as well as its early use in cochlear implants (112), IrO_x has been thoroughly investigated and is often touted as possessing many of the desired properties of neural interface electrode coatings (78). Despite this thorough examination of IrO_x, an under-reported characteristic IrO_x films is the growth a of nanoflake microstructure, which while associated with excellent electrochemical performance, is mechanically fragile. This can often lead to a reduction in its charge exchange characteristics and reduction in its functionality and longevity when handled and over time as this author and others have demonstrated (81,89,111,113,114). Thus, there is still a need to identify and develop new materials for implantable neural interfacing applications which exhibit the excellent electrochemical and biocompatible properties of IrO_x while not developing unfavorable mechanical and microstructural characteristics. Among these new materials are other PGM single metal oxides, as well as PGM binary and ternary metal oxides.

This dissertation outlines the synthesis and characterization of known and newly investigated PGM single metal oxides and PGM binary and ternary metal oxide solid solution thin films for use as implantable neural interface electrode coatings. The single metal oxides investigated include IrO_x, RuO_x, Rh_xO_y, and PdO. The binary metal oxide solid solutions studied include $Ir_{(1-x)}M_x$ oxides where M = Pd, Rh, Ru, while the ternary metal oxide solid solutions studied include $Ir_{(1-x-z)}M_xM'_z$ oxides, where M, M' = Pd, Ru, Rh. The objective of this dissertation is to identify the processing parameters, structures, and properties which result in oxide thin films possessing favorable neural interfacing electrode/microelectrode characteristics *i.e.*, high charge storage capacity (CSC_C), low impedance, excellent redox and chemical stability, favorable biocompatibility, and good mechanical stability.

Chapter 2

Platinum Group Metals

This chapter provides an overview of platinum group metals, platinum group metal oxides, and their applications.

2.1 General Properties

Platinum group metals (Fig. 2.1) are a collection of d-block (4*d* and 5*d*, groups 8, 9, and 10) transition metals which share general similarities in their physical and chemical properties and include Ru, Rh, Pd, Os, Ir, and Pt (115). The similarities and differences in the properties of PGMs can be explained through examining the "heavier" PGMs of Os, Ir, and Pt. The heavier elements possess a fully occupied 4*f* orbital as shown in Table 2.1. As a consequence the elements are subject to the "lanthanide contraction" that results from the nucleus having greater attraction to the 6s electrons due to poor shielding from the 4*f* orbital, resulting in a smaller atomic size (116).

Table 2.1

PGM Electron Orbital Structure

Metal	Noble Gas Structure	Orbital
Ru	[Kr]	$4d^{7}\ 5s^{1}$
Rh	[Kr]	$4d^{8}\ 5s^{1}$
Pd	[Kr]	$4d^{10}$
Os	[Xe]	$4f^{14}\ 5d^{6}\ 6s^{2}$
Ir	[Xe]	$4f^{14}\ 5d^{7}\ 6s^{2}$
Pt	[Xe]	$4f^{14}\ 5d^{9}\ 6s^{1}$

However, as Bond (2) points out, a greater contributor to the atomic contraction and the partial occupation/splitting of the valence orbitals of the "heavier" PGMs and all 5*d* transition metals are the relativistic effects on electrons in elements with a Z > 50. For such atoms, electrons must move at relativistic speeds to overcome the electrostatic attraction of the positive nucleus with a resultant increase in electronic mass described by the effective mass correction (momentum) for special relativity(2):

$$\mathrm{m_{rel}} = \frac{\mathrm{m_o}}{\sqrt{1-\frac{\mathrm{v}^2}{\mathrm{c}^2}}} \tag{1}$$

where m_o is the rest mass of the particle, v is the speed of the rest particle, c is the speed of light, and m_{rel} is the effective relativistic mass. The relativistic corrections for the electron orbitals and atomic size are shown in Fig 2.2 and Fig. 2.3 and demonstrate that with relativistic correction considerable changes occur in the *d*, *s*, and *p* orbitals with increasing *Z*-number.

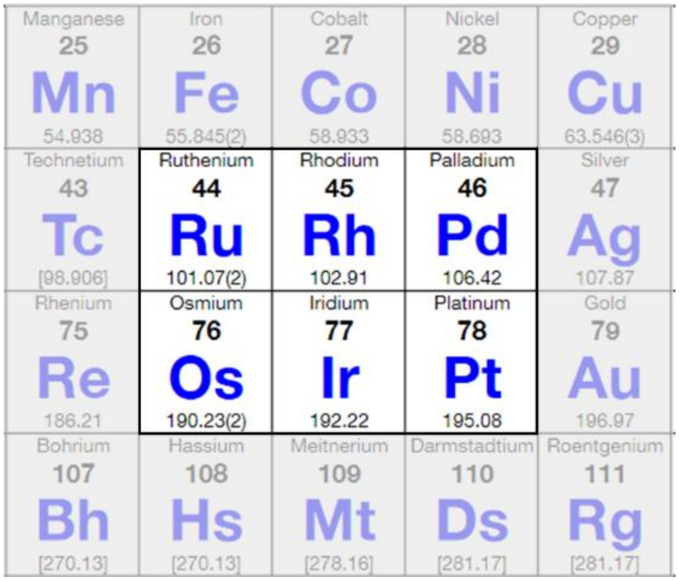

Manganese 25 Mn 54.938	Iron 26 Fe 55.845(2)	Cobalt 27 Co 58.933	Nickel 28 Ni 58.693	Copper 29 Cu 63.546(3)
Technetium 43 Tc [98.906]	Ruthenium 44 Ru 101.07(2)	Rhodium 45 Rh 102.91	Palladium 46 Pd 106.42	Silver 47 Ag 107.87
Rhenium 75 Re 186.21	Osmium 76 Os 190.23(2)	Iridium 77 Ir 192.22	Platinum 78 Pt 195.08	Gold 79 Au 196.97
Bohrium 107 Bh [270.13]	Hassium 108 Hs [270.13]	Meitnerium 109 Mt [278.16]	Darmstadtium 110 Ds [281.17]	Roentgenium 111 Rg [281.17]

Figure 2.1. Platinum group metals in the periodic table (1).

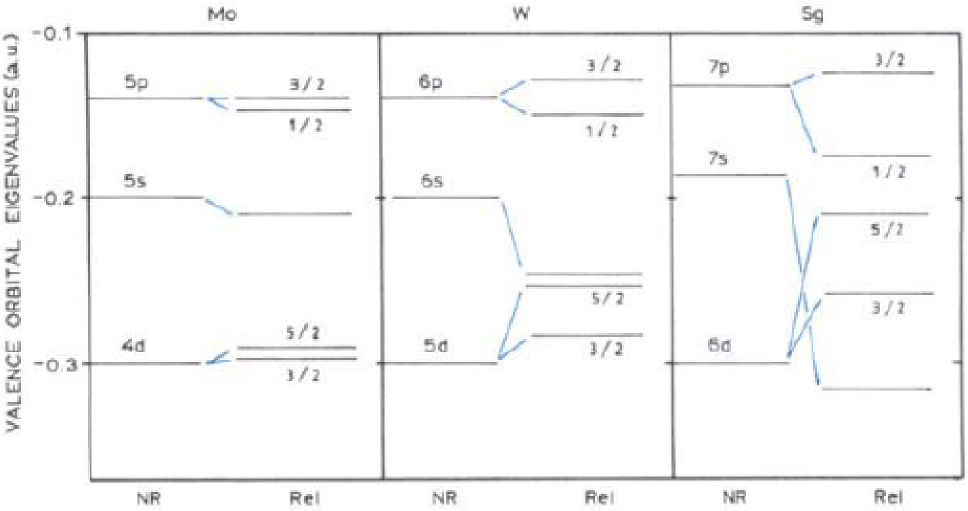

Figure 2.2. This shows the calculated outermost atomic energy levels for molybdenum, tungsten and seaborgium, (assumed to be analogous to palladium, platinum, and darmstadtium. The left-hand part for each element shows the non-relativistic values (NR) and the right-hand part the values having the relativistic correction (2,3).

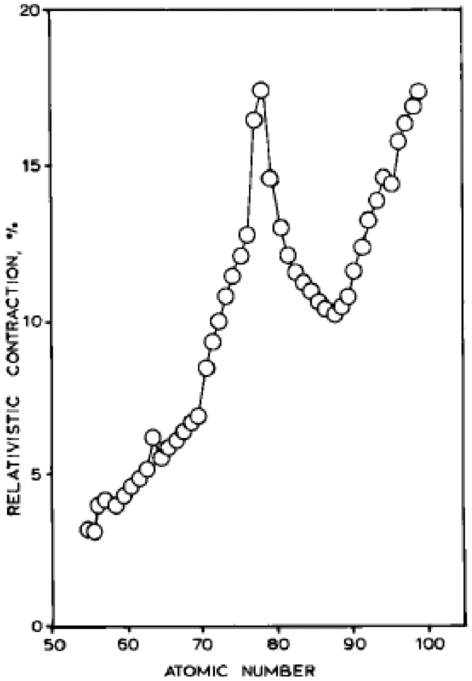

Figure 2.3. Relativistic contraction of the 6s electron level as a function of nuclear charge (2,3).

Consequently, small differences in energy exist between valence orbitals, and the atomic size difference between the “lighter” and “heavier” PGMs is considerably smaller than anticipated. Therefore, many of the important properties shared by PGMs and the differences between the “lighter” and “heavier” PGMs, such as the formation of chemical complexes, catalytic properties, multiple oxidation states (Table 2.2), corrosion resistance, and high melting point can be attributed to the unique atomic characteristics and electronic configuration of PGMs. Additional relations within the PGMs towards chemical properties and compound formation can be gathered from examining the similarities (or lack thereof) between oxidation states, electronic structure, and related criteria (117).

Table 2.2

PGM Oxidation States and Atomic Radii

Metal	Oxidation States	Van der Waals Radius (pm)	Ionic Radius (pm)	Electronegativity	Valency
Ru	-2, 0, +2, **+3, +4,** +5, +6, +7, +8	205	62 (**+4**)	2.2	+8
Rh	-1, 0, +1, +2, **+3**, +4, +5, +6	195	60 (**+4**)	2.28	+6
Pd	0, **+2**, +3, **+4**	202	86 (**+2**)	2.0	+4
Os	-2, 0, +1, +2, +3**, +4,** +5, +6, +8	200	62 (**+4**)	2.2	+8
Ir	-1, 0, +1, +2, **+3**, **+4**, +5, +6, +8	216	62.5 (**+4**)	2.2	+8
Pt	0, **+2**, **+4**, +5	209	62.5 (**+4**)	2.28	+5

2.2 Applications

The unique characteristics of PGMs and PGM compounds enable their use in a wide and varied array of applications. The most prominent use of PGMs is in autocatalysts to reduce pollution by converting hydrocarbons, nitrous oxides, and carbon monoxide into much safer nitrogen, water vapor, and carbon dioxide. Ordinarily Rh, Pt, and Pd coated on a high surface area substrate are used in this application although Ru has also been considered for this application (118,119). Interestingly, PGMs and PGM compounds are also used in cancer treatment. Pt compounds such as cisplatin and oxaliplatin inhibit the growth of cancer cells while radioactive Ir isotopes and Pd-103 are used for targeted tumor therapy known as brachytherapy (120). There is significant interest in PGMs for use in fuel cells for renewable energy generation and storage. In this application Pd may play a particularly important role in the storage and purification of hydrogen due to its extraordinary hydrogen loading ability and its capability to act as a selective permeable barrier of hydrogen when used in thin films (20,121–123). Additionally, as this thesis reports PGM and PGM oxides are extensively used in many neural interfacing applications. The lesser used PGM osmium (Os) is extremely rare and is the densest known elements. It is often alloyed to develop hard and wear resistant compounds. Additionally, Os-based compounds are also used in cell and tissue staining for microscopy. The applicability of Os and Os-based compounds is limited by its rarity and its tendency to form the highly toxic OsO_4 compound l (120,124). However, the applications mentioned only scratch the surface of the ubiquity of uses for PGMs and PGMs compounds.

Chapter 3

Thin Film Synthesis

3.1 Introduction

This section provides a background and overview of sputtering processes and configurations.

3.2 Sputter Deposition

Sputtering is a physical vapor deposition technique wherein energetic particles impinge on the surface of a solid target material and via momentum transfer eject the target atoms or molecules into a gas phase which then condenses onto a substrate to create a thin film (125,126). Due to the relative simplicity of its operation and the consistency of the resultant films, sputtering is utilized in many settings such as optics for anti-reflective and optical filters (126,127), electronics for semiconductors and sensors (128–132), data storage such as flash memory (133,134), medical devices for electrode and bio-integrative coatings, and energy storage and generation such as solar panels or fuel cells (20,135–137).

For sputter deposition to occur a plasma must be generated and sustained. Plasma generation is achieved when sufficiently high DC voltages are established between electrodes. Plasma is initiated when an electron near the cathode is accelerated towards the anode via an electric field. If the electron collides with a neutral gas (typically a noble gas) atom during this transport to the anode at sufficiently high energies gas breakdown will occur. The gas atom will be ionized according to the following relation:

$$e^- + A \rightarrow 2e^- + A^+ \tag{2}$$

where e^- is an electron, A is a neutral noble gas atom, and A^+ is a positive noble gas ion. The collision between the electron and the noble gas atom results in the generation of 2 electrons (in accordance with charge conservation) as shown in Fig 3.1.

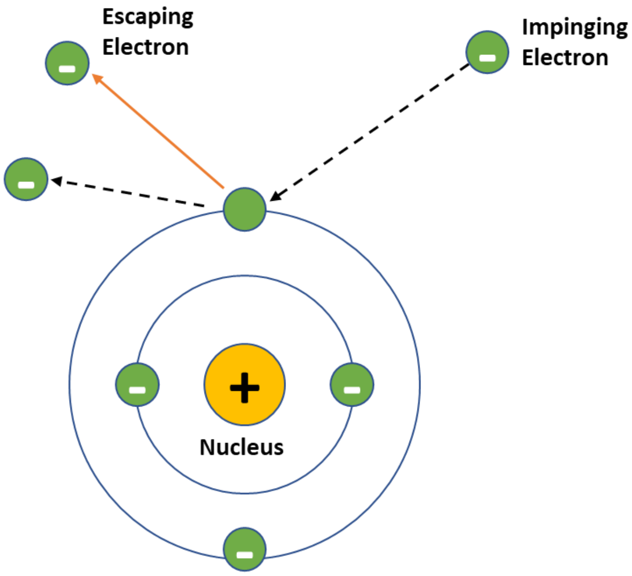

*Figure 3.1***.** Ionization of a molecule from an impinging high energy electron.

This process will continue so long as the generated electrons obtain enough energy to ionize more neutral atoms in an ever-increasing process referred to as an ionization or Townsend cascade which then results in a sustained plasma (6). It is for this reason that sputtering must be performed at high vacuum (< 100 mTorr). Too high of a pressure and the electrons will not gain sufficient energy for the ionization cascade to occur (due to a greater number of collisions) while at too low of a pressure there is insufficient gas to sustain the ionization cascade as electrons will simply travel from the cathode to the anode.

Once positive ions are generated, they will accelerate towards the target (cathode) and penetrate its surface. Target atoms will be sputtered as a result of a series of knock-on events occurring near the surface where a target atom is dislodged from the lattice as schematically shown in Fig. 3.2.

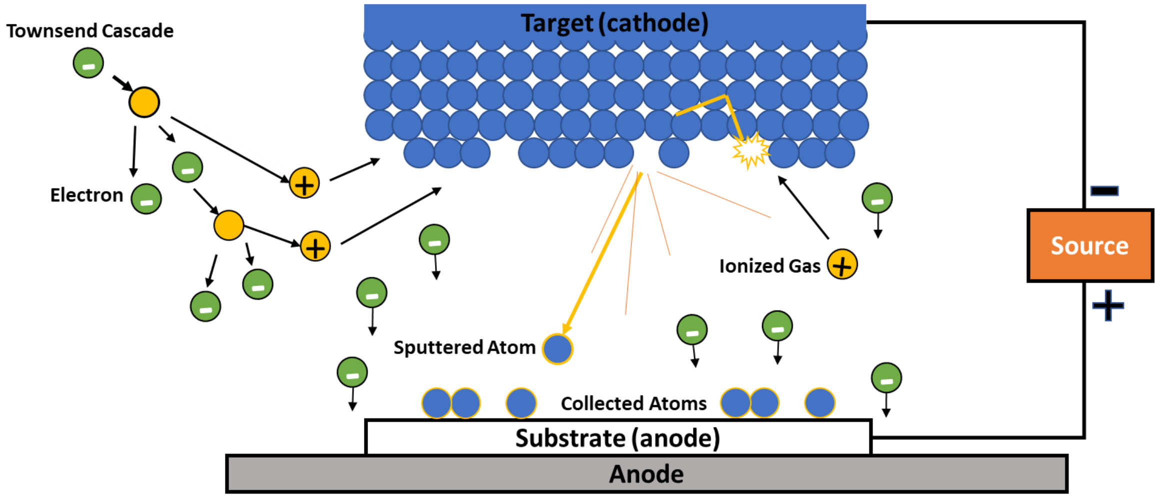

Figure 3.2. Diagram of the Townsend cascade and the sputtering process at the target surface and condensed species on the substrate.

Typically, the collisions are considered to be elastic, and the sputtering process can be modeled as two hard spheres colliding which is described by the sputter yield equation (6):

$$Y = \frac{3\alpha}{4\pi^2}\frac{4m_{ion}m_{sp}}{(m_{ion}+m_{sp})^2}\frac{E}{U} \tag{3}$$

where m_{ion} is the mass of the incident ion, m_{sp} is the mass of the target atom, E is the energy of the incident atom, U is the surface binding energy of the target, α is a constant of proportionality based on m_i and m_T.

3.2.1 DC Magnetron Sputtering

Ordinary DC sputtering has limitations. Among these are extremely low deposition rates, bombardment of the substrate with energetic particles causing unwanted heating leading to damage to the growing film and substrate, and inconsistent film growth. Thus, ordinary DC sputtering has been superseded by DC magnetron sputtering (Fig. 3.3). The concept behind DC magnetron sputtering is deceptively simple. It takes advantage of the fact that ions and electrons, which make up the plasma, respond to magnetic fields. Thus, by placing strong magnets (such as those made from neodymium iron boron) behind the target, the generated plasma can be confined to cathode and thereby direct positive ion flow to the target much more efficiently. As a result, sputter deposition rates are considerably greater, film growth is much more consistent, and unwanted effects such as residual heating from energetic charged particles are greatly reduced.

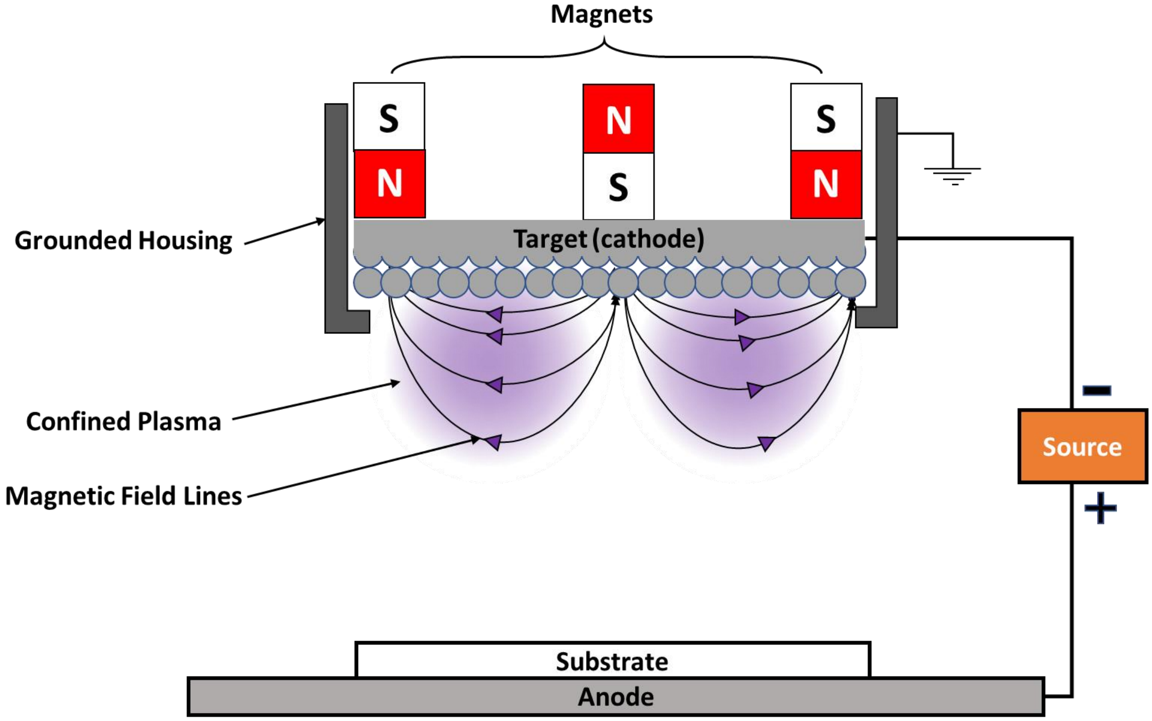

Figure 3.3. Schematic of a magnetron sputtering cathode and magnetron configuration.

3.2.2 Reactive Magnetron Sputtering

Reactive magnetron sputtering is a method to deposit thin film compounds with one or more reactive gases (oxygen, nitrogen, carbon, sulfur, etc…) and a working gas which is typically a noble gas (*L*) (Ar, Kr, Ne, etc…). The amount of reactive gas can be tuned to incorporate small amounts of dopants, or to form full and even over-stoichiometric compounds such as those shown in Table 3.1.

Table 3.1

Common Reactive Sputtering Compounds

Reactive Gases	Compound Type	Typical Compounds
Oxygen	Oxides	Al_2O_3, In_2O_3, SiO_2, Ta_2O_5
Nitrogen	Nitrides	TaN, TiN, ZrN, AlN, Si_3N_4
Carbon (CH_4, C_2H_2)	Carbides	TiC, NbC, WC, SiC, VC
Sulfur (H_2S)	Sulfides	CdS, CuS, ZnS
CO_2	Oxycarbides	Ti, Ta, Al, Si
N_2O	Oxynitrides	Ti, Ta, Al, Si
H_2O	Oxyhydrides	Ir, Y, La, Sr

The dissociation energy of molecules tends to be lower than their ionization energy. Because of this tendency plasma generation is more complex in reactive magnetron sputtering. In addition to Eqn. 2, additional considerations must be made with respect to the creation of radicals relating to the dissociation of reactive gas molecules. These include dissociative capture and further ionization as shown in the ion-pair reactions (6):

$$e^- + O_2 \rightarrow O + O^- \tag{4a}$$

$$e^- + O \rightarrow e^- + O^+ \tag{4b}$$

$$e^- + O_2 \rightarrow O^+ + O^- + e^- \tag{4c}$$

The resultant plasma will include positive noble gas and reactive gas ions, negative reactive gas ions, and energetic neutral atoms (typically from the reactive gas through electron capture). The negative ions generated are particularly interesting due to their tendency to accelerate away from the target (cathode) to the substrate (anode) at high energies in a process referred to as negative ion bombardment (138–147). As a result of the high energy bombardment, films tend to be more dense (due to knock-on effects closing voids) and develop greater intrinsic stresses from interstitial implantation and knock-on effect dislodging atoms at equilibrium sites at higher ion energies.

3.2.2.1 Pulsed DC Reactive Magnetron Sputtering. Often in reactive magnetron sputtering target poisoning will occur wherein a thin dielectric layer will form on the surface of the target (typically on non-sputtered portions of the target) (148). The dielectric layer will build up positive charge and a dielectric breakdown will occur in a phenomenon known as arcing (149,150). The target material will be subject to a dense plasma discharge which ejects large amounts of material in the form of droplets or macroparticles. As a result, growing films develop a high number of defects, lack consistency in growth, and are overall of lower quality. To overcome this issue reactive sputtering is performed with a pulsed-DC power supply which generates a square wave pulse as shown in Fig. 3.4, drawing electrons to the cathode to discharge the positive charge buildup on the target surface by reversing the polarity of the cathode. The use of pulsed DC reactive magnetron sputtering is particularly useful over other techniques such as RF reactive magnetron sputtering due to its comparatively higher deposition rates.

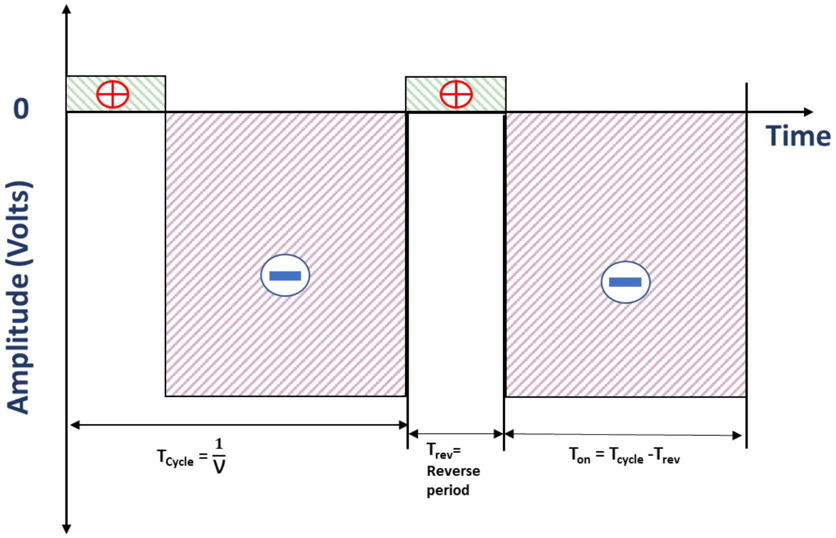

Figure 3.4. Illustration of pulsed DC square-waveform. T_{cycle} is the period for one cycle to occur which is the inverse of the frequency, T_{rev} and T_{on} represent the periods in which the target surface is discharged and sputtered, respectively.

3.2.3 Combinatorial Reactive Magnetron Sputtering

Combinatorial magnetron sputtering is a high throughput technique to rapidly synthesize, discover, and optimize new materials (151). Unlike incremental or single step synthesis methods which may result in a narrow compositional range, combinatorial methods are able to create large compositional ranges of materials from a single deposition as suggested by Fig. 3.5, thus making it a powerful technique for the rapid development of new materials. Because of this, combinatorial synthesis has been used in the discovery and optimization of dielectric films (152), metallics glasses (153), electrode materials (154), and non-noble metal catalysts (155). Outside of the work reported in thesis the combinatorial method has not be implemented in the optimization and discovery of new PGM binary and ternary metal oxides.

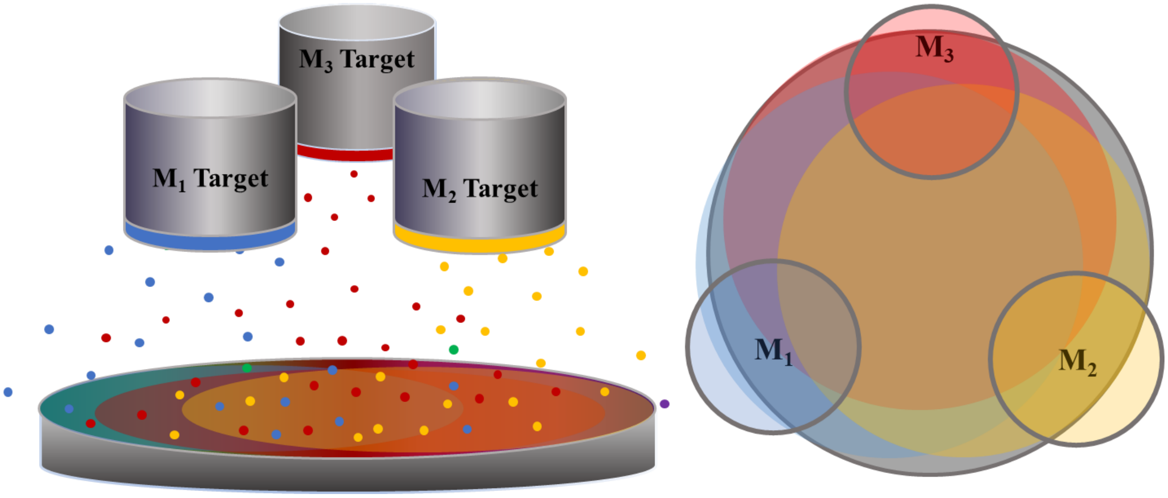

Figure 3.5. Representative diagram of a 3-source configuration for the combinatorial reactive magnetron sputtering deposition process.

3.3 Thin Film Growth

The following sections provides a general overview of the growth of films from the vapor phase to adsorption and condensation and finally to film structure.

3.3.1 Nucleation and Kinetics

Film growth can be said to begin in the vapor phase when atoms are sputtered from the target and transport to the substrate in gaseous state. The energy of sputtered atoms immediately after leaving the target can be described by the Thomson distribution (F_{TH}) (156):

$$F_{TH}(E_{sp}) = \left\{ \begin{array}{c} 2\left(1 + \frac{u_T}{\beta_{ion-sp}E_{in}}\right)^2 \frac{u_T E_{sp}}{(u_T+E_{sp})^3} \text{ for } E_{sp} \leq \beta_{ion-sp}E_{in} \\ 0 \text{ for } E_{sp} > \beta_{ion-sp}E_{in} \end{array} \right\} \qquad (5a)$$

where β_{ion-sp} is the kinetic energy fraction of colliding particles which can be determined using:

$$\beta_{ion-sp} = \frac{4m_{ion}m_{sp}}{(m_{ion}+m_{sp})^2} \tag{5b}$$

u_T is the surface binding energy of the target material, E_{sp} is the average kinetic energy of the sputtered atoms, E_{in} is the incident energy of the ion incident on the target surface (proportional to the discharge voltage), $\beta_{ion\text{-}sp} E_{in}$ is the maximum recoil energy, assuming elastic hard sphere collision model. $\beta_{ion\text{-}sp}$ is at a maximum when $m_{ion} = m_{sp}$, and the closer the mass of the working gas ion to the target material the more efficient the sputtering process. Following their release from the target and assuming motion is random, the behavior of sputtered atoms during gas transport can be described by the distance traveled before colliding with another atom or molecule known as the mean free path (λ_{mfp}) and the number of collisions per unit length traveled (N). The following equations describe the interaction of a sputtered atom with different background gases (6,7,156):

$$\lambda_{mfp} = \frac{k_B T_g}{\sigma_{LJ} P_{Tot} (1+\frac{m_{sp}}{m_g})^{1/2}} \tag{6a}$$

The value σ_{LJ} is the Lennard-Jones radius given by:

$$\sigma_{LJ} = \pi(r_g + r_{sp})^2 \tag{6b}$$

and the number of collisions (N):

$$N = \frac{d}{\lambda_{mfp}} \tag{7}$$

where k_B is the Boltzmann constant, T_g is the background gas temperature, P_{Tot} is the total pressure of the background gas, d is an arbitrary length of travel (typically the distance between target and substrate), and σ_{LJ} is the elastic collision cross section based on the Leonard-Jones radii (which accounts for soft repulsive and attractive forces, describing electrical neutral interactions), and m_g and m_{sp}, and r_g and r_{sp} are the gas and sputtered atom molecular masses and atomic radii, respectively. Clearly as the pressure increases the mean free path decreases and the number of collisions increases, and at sufficiently high pressure sputtered atoms will thermalize. The number of collisions is a useful equation for optimization and allows for a cursory assessment of sputtering dynamics during gas transport. Once a total working pressure and distance (distance between target and substrate) have been established, the average number of collisions can be estimated.

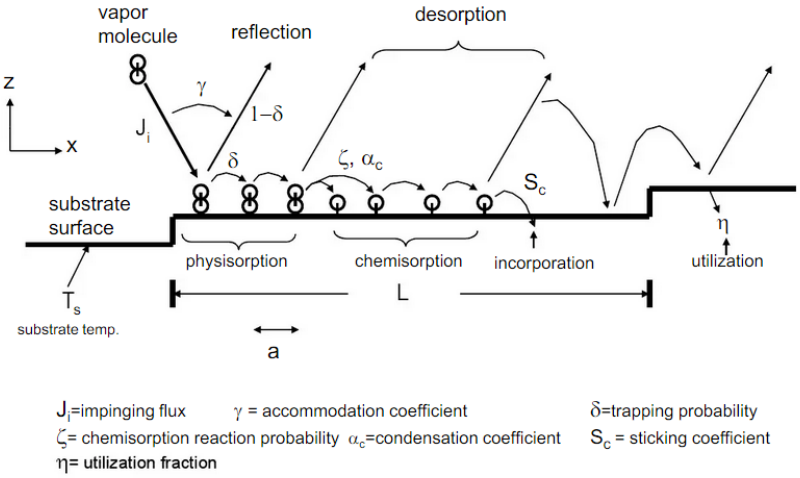

Figure 3.6. Adsorption process for a molecule impinging on a substrate (4).

Following impingement of sputtered atoms on the substrate, the incident atoms can desorb elastically, inelastically, or from trapping (capture of adatoms by defects and desorption). Alternatively, incident atoms can stick on the substrate surface through adsorption (typically with a binding energy of greater than 0.3 eV). The various sorption processes an incident atom or molecule may experience are shown in Fig. 3.6. The sputtered adatoms that remain on the surface will experience a weak attraction to the substrate through Van der Waals, dipole/dipole, or polarization interactions referred to as physisorption as shown in Fig. 3.6 and will remain on the surface for a residence time (τ_s) (7) described by:

$$\tau_s = \frac{1}{v} e^{-\left(\frac{E_{des}}{k_B T_s}\right)} \tag{8}$$

where v is the attempt frequency describing the number of adatom attempts to overcome a barrier and is related to the vibrational frequency of the adatom (typically on the order of 10^{13} Hz), E_{des} is the desorption energy *i.e.*, the energy needed for the adatom to return to the gas phase, and T_s is the substrate temperature.

Physiosorbed adatoms will then diffuse or jump randomly on the substrate surface according to the jump frequency (v_j) (7):

$$v_j = v e^{-\left(\frac{E_s}{k_B T_s}\right)} \tag{9}$$

where E_s is the activation energy for surface diffusion. Adatoms will randomly diffusion and jump eventually forming adatom pairs or nucleate into larger clusters eventually forming stable nuclei. This behavior is assisted by various surface inhomogeneities such as terraces, kinks, or defects as schematically shown in Fig 3.7. At these sites, the transition point from physisorption to chemisorption occurs (as long as the adatom is capable of forming a chemical bond).

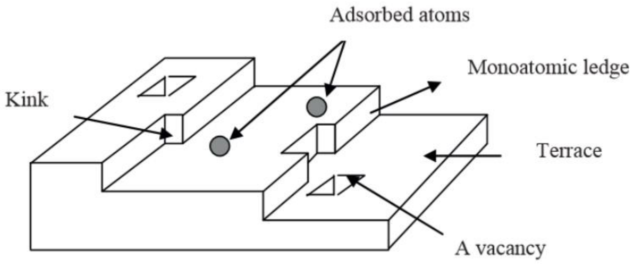

Figure 3.7. Various atomic positions as described by the terrace, ledge, kink model for early stages of film growth for adsorbed atoms (5).

Adsorption and transition of reactive gas from a physiosorbed to a chemisorbed state requires the molecular bond of the admolecule to be broken and is normally accomplished by thermal activation. The diffusion length of adatoms on the substrate surface during the residence time (τ_s) influences the formation of pairs, clusters, and larger nuclei and can described by the diffusivity coefficient (D_s) (6,7):

$$D_s = \frac{1}{2} a_0^2 v e^{-(\frac{E_S}{k_B T_S})} \tag{10}$$

And the mean diffusion length (X) (6,7):

$$X = (2D_s\tau_s)^{1/2} = a_o e^{\left(\frac{E_{des}-E_s}{2k_B T_s}\right)} \qquad (11)$$

where a_o is the adatom jump distance between surface sites which is proportional to the lattice constant of the substrate. The difference E_{des}-E_s determines whether adatoms will diffuse or desorb. At this stage desorption involves the dissociation of chemical bonds, and because of this it takes a greater amount of energy to desorb than to diffuse along the surface, *i.e.*, $E_{des} > E_s \Rightarrow$ diffusion (given the number of paired bonds does not change). Furthermore, large values of E_{des} and small values of E_s result in larger nuclear capture radii.

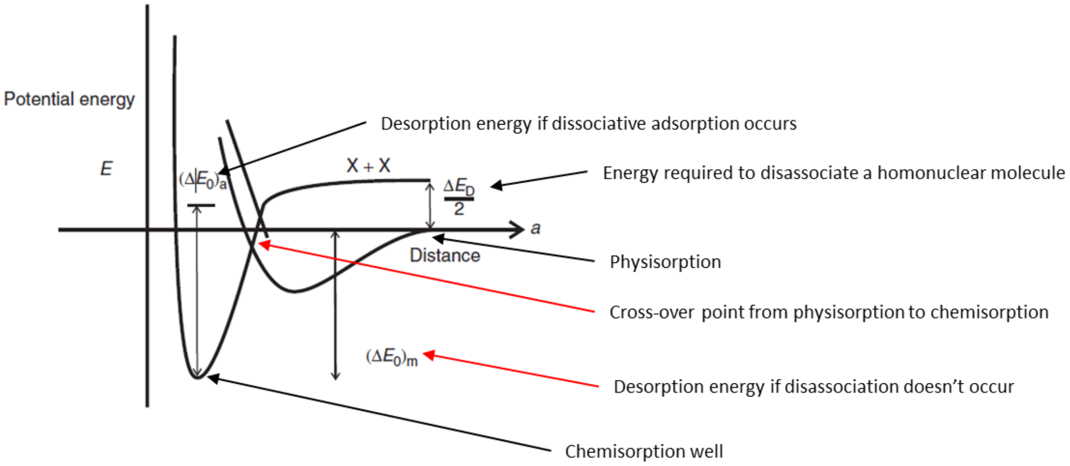

Figure 3.8. Potential energy versus distance curve for a homonuclear molecule undergoing dissociative adsorption at the substrate surface adapted from Sree (6).

3.3.2 Thin Film Growth

The early stages of film growth begin with an increase in the density of stable nuclei as shown in Fig. 3.9. Nuclei formation increases for a period of time, plateaus indicating stabilization of nuclei growth, then decreases as a result of coalescence; Additionally, as Fig. 3.9 depicts, the density of nuclei over time (deposition time) is greater at higher temperatures but the region of stability is much smaller indicating the transition from formation and growth to coalescence occurs much faster. While deposition at lower substrate temperatures results in the formation of stable nuclei for a longer period suggesting that the coalescence process is much slower (likely a result of slower adatom diffusion and cluster migration rates).

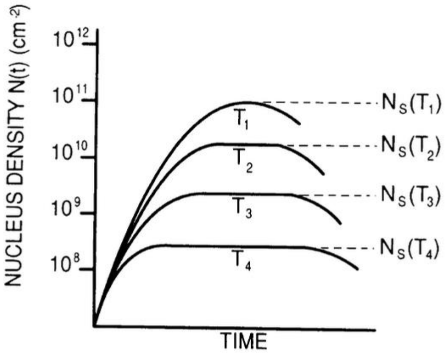

Figure 3.9. Schematic dependence of the rate of nuclei formation with time and substrate temperature $T_1>T_2>T_3>T_4$. N_s is the stable nucleus density. (6).

The growth and coalescence (intergrowth) of stable nuclei can be described by three types of growth modes as shown in Fig. 3.10. The first mode shown in Fig. 3.10a is referred to as the Volmer-Weber island growth model and is characterized by the growth of discrete islands or nuclei completely separated on the substrate. This type of growth can be expected for depositions at lower substrate temperatures and/or from deposition on a surface with many inhomogeneities or defects.

The second mode of growth as shown in Fig. 10b, is referred to as Frank-van der Merwe layer growth model. This mode features the formation of monolayers which grow simultaneously on the film layer by layer. This type of growth occurs when the interaction strength of the film to the substrate is greater than the atom-atom interaction strength within the film.

The final growth mode is shown in Fig. 10c and is referred to as Stranski-Krastanov growth. This mode is effectively a combination of the previous two modes. Initially, the monolayer growth mode takes precedence; however, if the lattice mismatch between the film and the substrate is sufficiently large, the growing film will be unable to accommodate the mismatch. As a result, film growth transitions from monolayer growth to the formation of discrete islands to reduce strain.

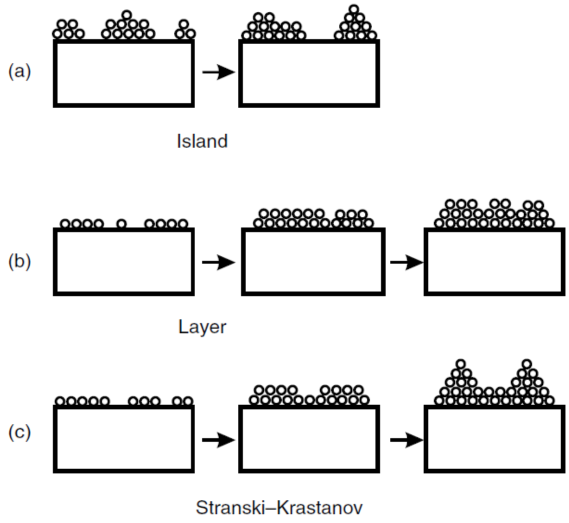

Figure 3.10. Modes of growth of film: (a) Volmer-Weber island growth (b) Frank-van der Merwe layer growth and (c) Stranski-Krastanov layer plus island growth (7).

The growth of films following the initial stages of condensation are well described by the Thornton structure zone model (SZM) for sputtered metal films shown in Fig. 3.11 (8). The film structure is highly dependent on total background pressure and substrate temperature, T_S (presented as a ratio of T_S/T_M, where T_M is the melting point of the film). It is worth noting that the model does not consider the effects of sputtering power density and ion bombardment on film structure.

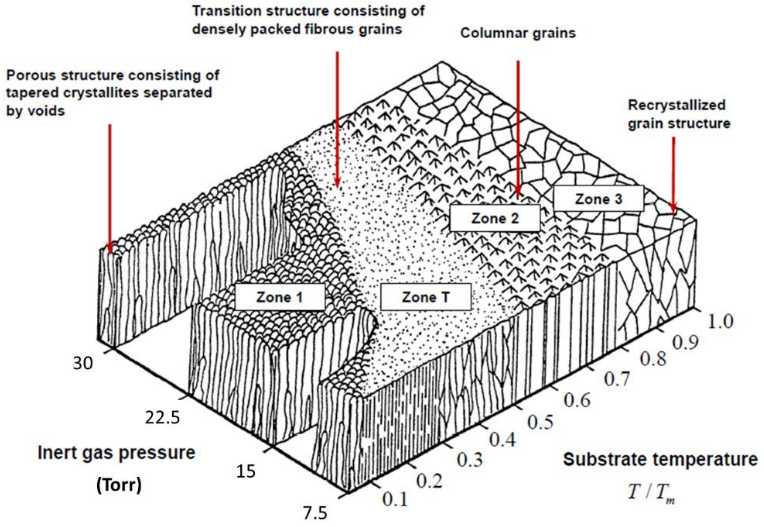

Figure 3.11. Schematic of the Thornton structure zone model for sputtered films (8).

Film/substrate temperature directly effects the growth of films. At higher temperatures (less than T_M) adatoms will have much longer diffusion lengths allowing them to situate in thermodynamically favorable sites. As a result, films will have larger grains and be much more crystalline. A general overview of thin film properties and structural characteristics for the SZM are shown in Table 3.2. The effects of temperature and pressure on film structure and properties differs somewhat in ceramics from their metal counterparts, for instance, at low T_S/T_M values ceramics have low hardness and become harder in zone II and III of the SZM.

Table 3.2

Zones, Structures, and Film Properties of Sputtered Films[a]

Zone	T_S/T_M	Structural Characteristics
1	< 0.1 at 7.5 Torr to < 0.5 at 30 Torr	Voided boundaries, small fibrous grains, amorphous, shadow effect driven, low surface diffusion
T	0.1-0.5 at 7.5 Torr, 0.4-0.5 at 30 Torr	Fibrous grains, dense grain boundaries, limited surface diffusion
2	0.4-0.7	Columnar grains, dense gran boundaries, surface diffusion driven
3	0.6-1.0	Large equiaxed grains, bulk diffusion driven

[a] Adapted from Ohring (7)

The effect of power density can promote an increase growth rate and nucleation rate in films as incident energies of particles will be high enough to allow for longer diffusion lengths on arrival and ballistically assisted diffusion of existing adatoms. However, if the power density is too high, incident particle energy on the substrate can damage the growing film, likely becoming more amorphous through resputtering, interstitial implantation, or the creation of vacancies.

3.4 Experimental Conditions

In the following sections the experimental details for synthesis of the PGM oxides will be discussed. All films were synthesized with a TM-Vacuum Smart-Jar (USA) (Fig. 3.12) deposition system configured with three two-inch circular planar cathodes (Angstrom Sciences ONYX cathode, U.S.A.). The Ir, Ru, Rh, Pd targets had a purity of 99.95% by weight (Johnson Matthey Inc, U.S.A., and U.K.). Targets were two inches in diameter and had thicknesses of 0.64 cm for Ru and Rh, and 0.32 cm for Ir and Pd. The targets were indirectly cooled with water flowing at a temperature of 14 °C.

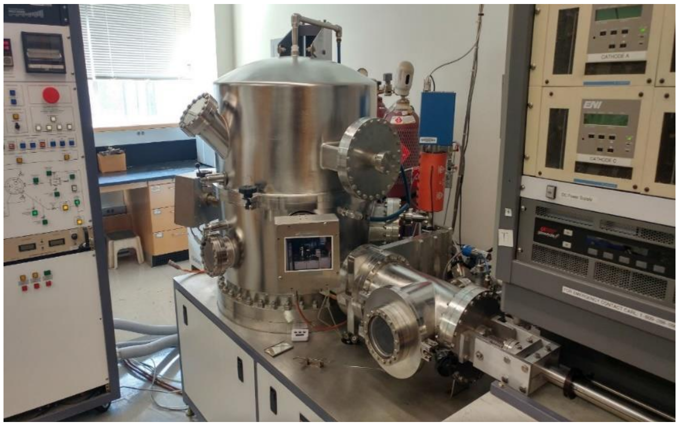

Figure 3.12. TM-Vacuum Smart Jar system used in the synthesis of films investigated in this thesis.

3.4.1 Single Metal Oxides

3.4.1.1 Synthesis. Single metal oxide depositions were performed at ambient substrate temperature with a pulsed DC power supply (Advanced Energy Pinnacle Plus, U.S.A.) with at a power of 100W. The power was held at 100 W at a frequency (*f*) of140 kHz and a reverse period of 1.8 µs. This power was selected to prevent unwanted substrate heating and other peripheral effects of high cathode power deposition discussed in section 3.3.2.1. Sputtering was performed in a mixture of Ar) and O_2 gases which were controlled by mass-flow controllers (MKS Instruments, U.S.A.). The pressure in the system was controlled downstream by adjusting the pumping rate of a turbopump (Leybold 1000C, U.S.A.) controlled with a capacitance manometer and a baffle valve

(MKS Instruments, U.S.A.). The overall gas flow rate (Ar + O_2) was held constant at 50 sccm. The oxygen partial pressures (OPPs) of the gas mixture were held at 20, 50, and 80% ($\frac{P_{O_2}}{(P_{O_2}+P_{Ar})} \times 100$) based on gas flow rates and at working pressures (WP) ($P_{O_2} + P_{Ar}$) of 5, 10, 20, and 30 mTorr.

3.4.1.2 Substrate Preparation. Films were deposited onto 316 stainless steel foil and plate (316 SS) (McMaster-Carr, U.S.A.), c-axis epi-polished sapphire (Al_2O_3) (Alfa Aesar, U.S.A.), and SiO_2/Si (University Wafer, U.S.A.) substrates at a working distance of approximately 10 cm. Substrates were mounted onto the sample tray with double-sided conducting copper tape (3M™ Copper Conductive Tape, U.S.A.) to ensure good thermal contact. Substrates were ultrasonically cleaned in a methanol (99.8% purity, Thermo-Fisher Scientific, U.S.A.) bath for 10 minutes and dried with dry nitrogen (N_2) gas. Prior to deposition, substrates were RF etched for a duration of 5 minutes at 100 W with high purity Ar gas flowing at 50 sccm at a working pressure of 20 mTorr. This step was performed to eliminate surface contamination ensuring consistent substrate surface conditions prior to deposition. During deposition, substrates were rotated at 30 rpm to ensure film thickness uniformity.

3.4.2 Binary Metal Oxides

$Ir_{(1-x)}M_x$ (M = Pd, Rh, Ru) oxide depositions were performed at ambient substrate temperature.

3.4.2.1 10 mTorr $Ir_{(1-x)}Pd_xO_y$. The preliminary 10 mTorr WP $Ir_{(1-x)}Pd_xO_y$ binary metal oxide coatings were prepared via co-sputtering. The Ir target was sputtered with a pulsed-DC power supply (Advanced Energy Pinnacle Plus, U.S.A) with a frequency of

140 kHz and a reverse period of 1.8 μs. A DC power supply (Advanced Energy MDX-1000) was used for the Pd_x targets. The approximate sum of the power between both power supplies was held constant at 100 W and the amount of power supplied to each cathode was varied between depositions to achieve various coating compositions. The reactive gas partial pressures utilized were 20, 50, and 80% OPP. Instrumentation was identical to that described in section 3.4.1.1 for the single metal oxides. Additionally, the substrate preparation (pre-cleaning, RF-etching, and mounting) steps, and rotation speed were identical to those described in section 3.4.1.2.

3.4.2.1 30 mTorr $Ir_{(1-x)}M_x$ (M = Pd, Rh, Ru) Oxides. The 30 mTorr WP $Ir_{(1-x)}M_x$ (M = Pd, Rh, Ru) binary metal oxide coatings were prepared via combinatorial sputtering. A schematic of the 3-cathode configuration is shown in Fig. 3.13a. The two Ir targets were supplied 25 W of power each from two different pulsed DC power supplies (Advanced Energy Pinnacle Plus, U.S.A, and Trumpf Hüttinger TruPlasma DC1000, DE), the M targets were supplied 50 W of DC power (Advanced Energy MDX-1000, U.S.A). The total gas flow rate was 50 sccm and the OPP was held at 20% (10 sccm). A circular sample tray with a diameter of 15.2 cm was placed under the cathode and a 316 SS foil substrate divided into three sections covered the entire sample tray area. The working distance and substrate preparation steps (pre-cleaning and RF-etching, mounting) were identical to those described in section 3.4.1.2. Samples were not rotated to ensure a large compositional gradient over the substrate area for a single deposition. A secondary nominally identical deposition was performed to estimate thickness of the combinatorially synthesized films. However, instead of 316 SS, coatings were deposited on 1.3 cm × 1.3 cm SiO_2/Si substrates (University Wafer, U.S.A.) placed throughout the sample tray area.

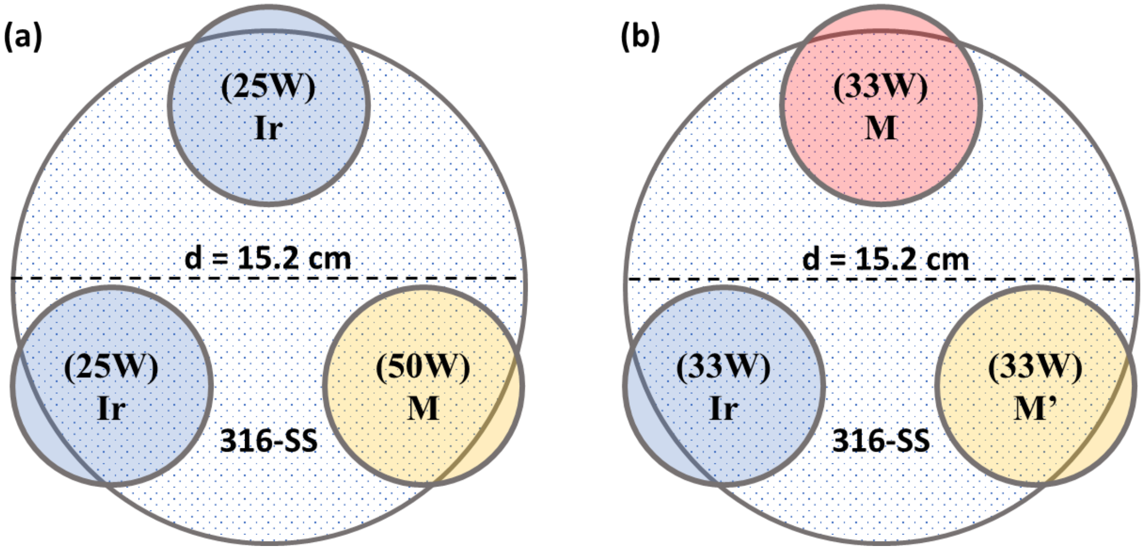

Figure 3.13. Overhead schematic representation of a three two-inch cathode setup for combinatorial synthesis of (a) binary metal $Ir_{(1-x)}M_x$ (M = Pd, Rh, Ru) and (b) ternary metal $Ir_{(1-x-z)}M_xM'_z$, (M,M´ = Pd, Rh, and Ru) oxides. The 316 SS foil and SiO_2/Si substrates were mounted onto the 15.2 cm diameter sample tray with double-sided conductive copper tape.

3.4.3 Ternary Metal Oxides

The ternary $Ir_{(1-x-z)}M_xM'_z$ (M, M´ = Pd, Ru, and Rh) metal oxide coatings were prepared via combinatorial sputtering. A schematic of the three-cathode configuration is shown in Fig. 3.13b. The Ir target was supplied 33 W of power from a pulsed DC power supply (Advanced Energy Pinnacle Plus, U.S.A), the M and M´ targets were each supplied 33 W of DC (Advanced Energy MDX-1000, U.S.A, and Trumpf Hüttinger

TruPlasma DC1000, DE (operated in DC mode), respectively). The total gas flow rate was 50 sccm and the OPP was held at 20% (10 sccm O_2). A circular sample tray with a diameter of 15.2 cm was placed under the cathode and a 316 SS foil substrate divided into three sections covered the entire sample tray area. The working distance and substrate preparation steps (pre-cleaning and RF-etching, mounting) were identical to those described in section 3.4.1.2. Samples were not rotated to ensure a large compositional gradient for a single deposition.

Chapter 4

Thin Film Characterization

This chapter is a brief overview of the characterization techniques that have been used on the oxide thin films investigated in this thesis.

4.1 Electrochemical Analysis

The following sections will provide a background and outline the techniques that were used to analyze the electrochemical properties of the as-deposited films

4.1.1 Electrochemical Cell

A typical electrochemical setup consists of a cell made of an electrically insulating and chemically inert material (PTFE, or glass), a three-electrode configuration, and an electrolytic solution (consisting of ionic species such as K^+, H^+, Na^+, Cl^-, and OH^- typically in water). A representative diagram of the cell used in this thesis is shown in Fig. 4.1. Each electrode in the cell plays a crucial role in studying and maintaining stable conditions for analysis.

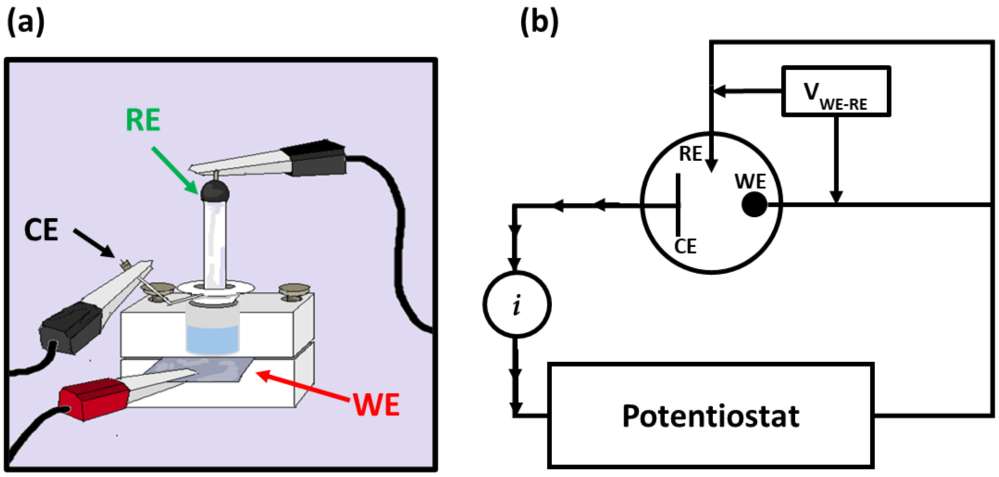

Figure 4.1. (a) Schematic of the three-electrode Teflon™ electrochemical cell used in this thesis. RE denotes the reference electrode (Ag|AgCl), CE denotes the counter or auxiliary electrode (high surface area coiled Pt wire), and WE denotes the working electrode (coated 316-SS or SiO_2/Si substrate). (b) Three-electrode cell schematic, V_{WE-RE} is the voltage between the reference and working electrode, and I is the current flowing from the working electrode to the counter electrode.

The three-electrode setup consists of a working electrode (WE), counter electrode (CE), and a reference electrode (RE). The working electrode is where the electrochemical reactions occur. For this thesis, the reaction is a reduction oxidation (redox) reaction shown by the following standard system redox reaction pair (9):

$$\mathrm{ne^{-} + O \rightleftharpoons R} \quad (12)$$

where *n* is the stoichiometric number of electrons involved in an electrode reaction. *R* is the reduced form of the standard system pertaining to species *O*, *O* is the oxidized form of the standard system pertaining to species *R*. The area of the WE can be defined in two ways; By the GSA or by the ESA as shown in Fig. 4.2. The GSA is much easier to evaluate and is simply a projection of the enclosed area of the electrode. The ESA on the other hand, is a much more complicated value to quantify as it relates to the surface variations of the electrode as well as the internal areas available for electrochemical processes to take place. This characteristic becomes particularly relevant when working with electrode and electrode coatings that are porous. In this thesis all measurements and calculations are performed with the GSA and qualitative statements on the ESA are made with supporting evidence.

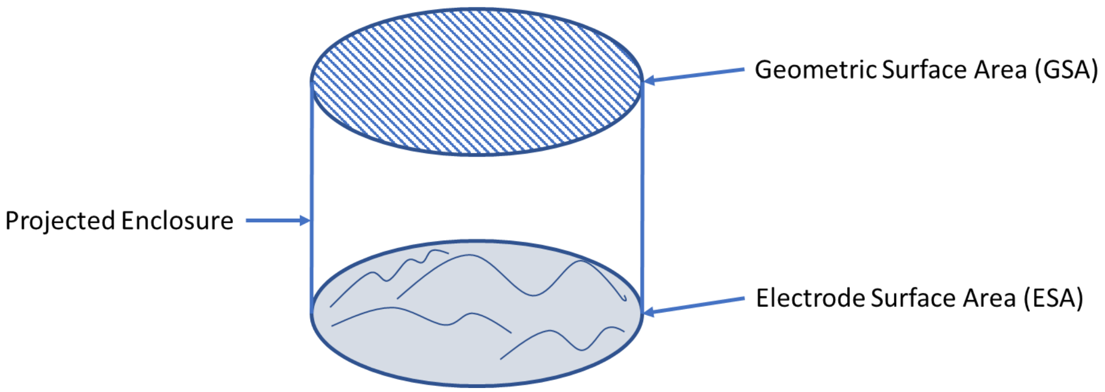

Figure 4.2. Electrode surface and the enclosure formed by projecting the boundary outward in parallel with the surface normal. The cross-section of the enclosure is the geometric surface area of the electrode adapted from Bard and Faulkner (9).

As the diagram in Fig. 4.3 shows, when the WE is driven to increasingly negative potentials, the energy in the electrons is increased and electrons are raised to higher energy levels. As a consequence, they can reach vacant electronic states enabling them to transfer to cations in the solutions. This transfer is referred to as the reduction current (the WE is the reducing agent or it is being oxidized). On the other hand, by driving the potential to more positive potentials the energy of electrons can be lowered, moving electrons to lower energy levels. This will drive anions to the electrode and facilitate electron transfer from the solution to the WE and is referred to as the oxidative current (the WE is the oxidizing agent or it is being reduced).

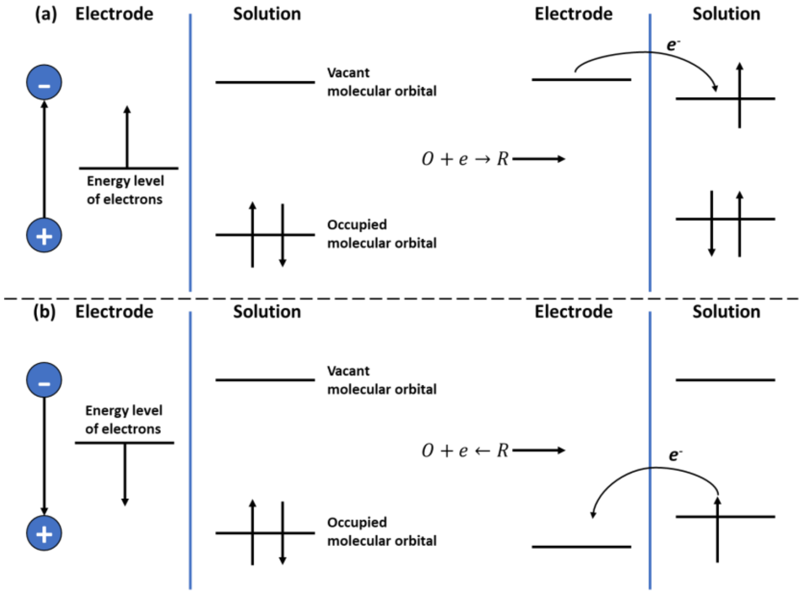

Figure 4.3. Representation of the (a) reduction of a species O and (b) oxidation of a species R in a solution. The highest occupied molecular orbital and the lowest vacant molecular orbitals are shown adapted from Bard and Faulkner (9).

The RE is an electrode with a known potential and is generally non-polarizable (potential does not change as current flows through it). Since the composition and potential of the RE is fixed any changes in the system are attributed to the WE when potential is cycled. The potential of the WE is typically measured with respect to the RE (Fig. 4.1b).

The CE is the third electrode in the system, and it acts as a current sink.source depending on the direction of the potential sweet, enabling current to be passed from the WE through it. This is preferable because if sufficiently high currents are passed through just RE, its potential will change and the processes occurring in the system can no longer be attributable solely to the WE, this would complicate analysis of the WE. The CE is normally a material that is ideally unreactive within the potential window being analyzed or will not produce any species that will interfere with WE reactions. For this dissertation, the CE is a coiled Pt wire. To ensure current passes between the WE and CE, the potential between the RE and WE is measured with an extremely high input impedance so that an insignificant amount of current flows into the RE.

4.1.2 Cyclic Voltammetry

Cyclic voltammetry (CV) is a widely used technique to study redox processes at the electrode electrolyte interface (between surface atoms and electroactive species in solution) by measuring the faradaic current that is generated from the heterogenous charge transfer (other contributions to current such as double layer capacitance will also be measured). CV provides information on the capacitance, potential window (water electrolysis window), reaction rates, reversibility and many other processes related to interfacial reactions and processes. The technique is performed by applying a linear time varying potential provided by a potentiostat across the WE and the CE (within the water window) and the current response is measured. This potential is then swept in the opposite direction to reverse the electrochemical process that has occurred. An example of a CV waveform is provided in Fig. 4.4a.

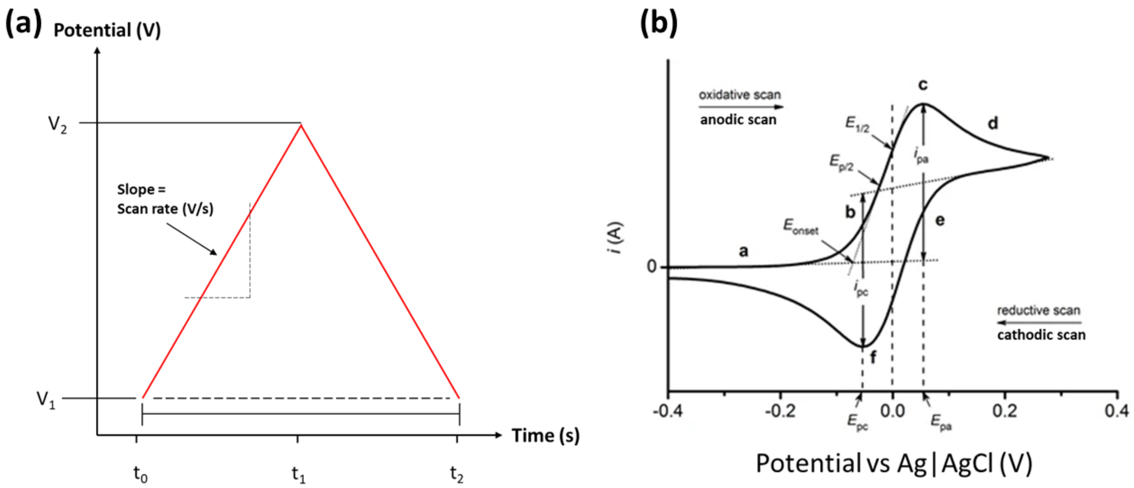

Figure 4.4. (a) Typical potential waveform used in cyclic voltammetry.(b) Cyclic voltammogram for a electrochemically reversible one-electron redox reaction (10).

The redox processes that occur at the electrode electrolyte interface result in mass transport of electroactive species to and from the electrode surface. The three mass transport processes include migration, convection, and diffusion. Migration can be understood as the movement of ions in the presence of an electric field generated when a potential difference is applied between the WE and the CE. For this thesis migration is considered to be a negligible contribution to measurements due to the use of a supporting electrolyte (which consists of high concentrations of non-electroactive ions) reducing the ohmic drop to negligible values. Additionally, convection is ignored as the systems investigated in this thesis are not stirred or are not subjected to any significant thermal gradients. For this thesis, diffusion which occurs as a result of chemical concentration gradients of electroactive species in the solution is considered to be the dominant mass transport mechanism.

The Nernst equation is considered one of the fundamental equations in CV. It expresses the relationship between the electrode potential and concentration or chemical driving forces on electroactive ions (9):

$$\mathrm{V} = \mathrm{V^{o}} - \frac{\mathrm{RT}}{\mathrm{nF}} \ln \left(\frac{\mathrm{C_O(x)}}{\mathrm{C_R(x)}}\right) \tag{13}$$

where V is the applied potential, V^{o} is the formal potential (midpoint potential between reduction and oxidation peaks $V_{1/2}$ (Fig. 4.4b) of a reversible reaction), F is Faraday's constant, T is the temperature of the solution (taken to be room temperature), C_O/C_R is the reaction quotient which is a measure of the relative amounts of the oxidized (C_O) and reduced (C_R) species as a function of distance from the electrode surface and n is the number of electrons transferred. By applying a potential, a concentration gradient is forced from consumption (oxidation or reduction) of reactants at the electrode surface. If we consider Fig. 4.3 in the context of the Nernst equation, sweeping the potential to increasingly negative values will reduce species O depleting its concentration near the electrode until $C_O = C_R$, while the opposite will occur when the potential is swept in the positive direction. The rate at which electrons are transferred is measured as the current response in the CV measurement which can provide useful information on electrochemical processes at the interface. In this thesis the current response is used to determine the charge storage capacity (CSC) of various oxide films and is calculated by the following equation:

$$\frac{1}{\nu A} \int_{V_1}^{V_2} i(V)\, dV \tag{14}$$

where v is the potential scan rate, A is the GSA of the electrode, V_1 and V_2 is the potential window, and i is the current. Additional information such as adsorption characteristics, the degree of reversibility of redox processes, and rate constants can be determined from the current by relating the peak current to the scan rate (or varying the scan rate) with the Randles-Secvik equation (9):

$$\mathrm{i} = (2.69\mathrm{E}5)\mathrm{n}^{3/2}\mathrm{A}\mathrm{D}_{\mathrm{R}/\mathrm{O}}^{1/2}\mathrm{v}^{1/2}\mathrm{C}^{*}_{\mathrm{R}/\mathrm{O}} \tag{15}$$

where $D_{R/O}$ is the diffusion coefficient of a species, and $C^{*}_{R/O}$ is the bulk concentration of a species.

4.1.3. Electrochemical Impedance Spectroscopy

Electrochemical impedance spectroscopy (EIS) is a frequency dependent measurement that measures the AC current of a system in response to an applied AC voltage. By using a small AC voltage signal (or perturbation), the AC current response will exhibit linear-like behavior. In other words, the response current will have the same frequency as the input voltage shifted by a phase angle (φ). The AC voltage signal can be described by the sinusoidal equation (9,157):

$$\mathrm{V(t)} = \mathrm{V_o}\sin(\omega \mathrm{t}) \tag{16}$$

$$\mathrm{I(t)} = \mathrm{I_o}\sin(\omega \mathrm{t} + \varphi) \tag{17}$$

where V is the potential at a time t, V_o is the amplitude of the input signal, I is the current at a time t, I_o is the current of the input signal, ω is the angular frequency ($2\pi f$), and f is the input frequency.

The input impedance can be calculated from the generalized Ohm's law and represented as a complex function including a phase angle φ, and a magnitude impedance (Z_o) (9,157):

$$\mathrm{Z}(\omega)=\frac{\mathrm{V(t)}}{\mathrm{I(t)}}=\mathrm{Z_o}[\cos(\varphi)+\mathrm{j}\sin(\varphi)] \tag{18}$$

where j is an imaginary number defined as $\sqrt{-1}$. This is significant as it allows for the expression of impedance in real and imaginary terms, allowing for deconvolution of factors which contribute to impedance such as solution resistance, various capacitive mechanisms, and even diffusion processes. To this end it is helpful to represent the impedance as a Nyquist (Z_{img} vs Z_{real}) and Bode plots (φ and Z_o vs f). Additionally, circuit elements which include but are not limited to capacitors, inductors, and resistors can be represented by real and complex equations. By combining equivalent circuit elements and impedance data from Nyquist and Bode plots the impedance response can be modeled by constructing an equivalent circuit. This process is referred to as equivalent circuit modeling (ECM). A table of elements used for EC-modeling in thesis are provided in Table 4.1.

The modeling of EIS spectra can often provide physical insight to the electrochemical processes that occur over the frequency ranges tested. These can include the determination of solution resistance, double layer capacitance (plate and Helmholtz), polarization resistance, charge transfer capacitance and resistances from (faradaic and pseudo-faradaic processes), diffusion behavior by way of Warburg elements, and imperfect capacitance by utilizing constant phase elements (CPE).

Table 4.1

Equivalent Circuit Elements and Corresponding Impedance Equations

Impedance Element	Equivalent Equation
Resistor (R)	R
Capacitor (C)	$\frac{-j}{\omega C}$
Bounded Warburg (W$_T$)	$\frac{1}{Y_0\sqrt{(j\omega)}}\coth\left(B\sqrt{j\omega}\right)$
Finite Length Warburg (W$_O$)	$\frac{1}{Y_0\sqrt{(j\omega)}}\tanh\left(B\sqrt{j\omega}\right)$
Constant Phase Element (CPE)	$\frac{1}{Y_0(j\omega)^n}$

4.1.4 Electrochemistry Experimental Conditions

CV and EIS were performed with a three-electrode setup with a potentiostat/galvanostat (Metrohm Autolab, PGSTAT204, NL). The as-deposited oxide films deposited on 316 SS and SiO_2/Si substrates served as the WE. Films deposited on 316 SS have roughly a 10% improvement in electrochemical performance over the SiO_2/Si substrates as measured by CV. The change in the electrochemical performance as a function of thickness for the two substrates are nearly identical. These characteristics are demonstrated in a later section (Section 5.4.1, Fig. 5.45) for RuO_x films. An Ag|AgCl electrode (ALS-Co Ltd. RE-1B, JP) was used as the RE, and a coiled platinum wire acted as the CE. A Teflon® plate cell (ALS-CO Ltd. Plate Material Evaluating Cell, JP) was used for the CV and EIS measurements (Fig. 4.1b). The GSA of the working electrode in the cell was 0.46 cm^2. The electrolyte used was a phosphate buffered saline (PBS) solution (NaCl (137), KCl (2.7), Na_2HPO_4 (10), KH_2PO_4 (1.8)(mmol/L)) (VWR Ultra-Pure PBS, 10X, USP sterile, U.S.A.) diluted to 0.1 M with DI water and had a pH of 7.4. The buffer was required to maintain a constant pH (158), and the volume of solution used per measurement was 1 mL. CV measurements were performed on three separate locations on each sample at a 0.10 V/s (v) sweep rate for 20 cycles at room temperature. Potential windows were selected to ensure water electrolysis did not occur in each of the systems. The water windows were identified to be -0.6 – 0.8 V and -0.4 – 1.0 V depending on the system. The voltage sweeps were initialized at open-circuit potential (OCP) and swept in the positive direction first . EIS measurements were performed over a frequency range of $10^{-2} – 10^{5}$ Hz with an amplitude of 10 mV. EC-modeling and EIS analysis was performed with Nova 2.1.4 software (Metrohm-Autolab, NL).

4.2 Structure/Microstructure/Topography

The following sections will outline the techniques that identify the crystal structure, microstructure, and topography of the as-deposited films.

4.2.1 X-Ray Diffraction

A crystal can be described as a periodic arrangement of atoms in a three-dimensional space. A table of different ordering of crystals is shown in Table 4.2, with structures spanning from amorphous lacking long-range order, polycrystalline which consists of randomly orientated crystallites with various size and shape, to mono-crystalline with one orientation with effectively perfect periodicity.

Table 4.2

Structure of Crystals and Definitions

Structure Type	Definitions
Perfect Epitaxial	Single crystal with perfect periodicity
Textured Polycrystalline (Preferred Orientation)	Crystalline planes are random in plane but have preferential orientation out of plane
Polycrystalline	Randomly orientated crystallites which may have different sizes and shapes
Amorphous	No long-range order, strong interatomic bonds (similar atomic distances to well defined crystals)

X-ray diffraction (XRD) is a widely used non-destructive experimental technique which can reveal information on the crystal structure of a material including phase, stoichiometry, lattice spacings, orientation, and strains. XRD involves the elastic scattering (Thompson scattering) of x-rays off of electrons in a material. The planes of atoms that make up a crystal can constructively or destructively interfere in accordance with Bragg’s Law:

$$n\lambda = 2d_{hkl}\sin\theta \tag{19}$$

where d_{hkl} is the interplanar spacing which depends on the unit cell parameters of the crystal. The subscript *hkl* refers to the Miller indices which are a set of integers which denote the intercepts of a surface along the crystallographic axes (defined from the unit cell dimensions). The angle θ is the Bragg's diffraction angle (Fig. 4.5a) where constructive interference can occur, λ the wavelength of the incident x-rays, and n (typically 1) is the multiplicity of the reflection.

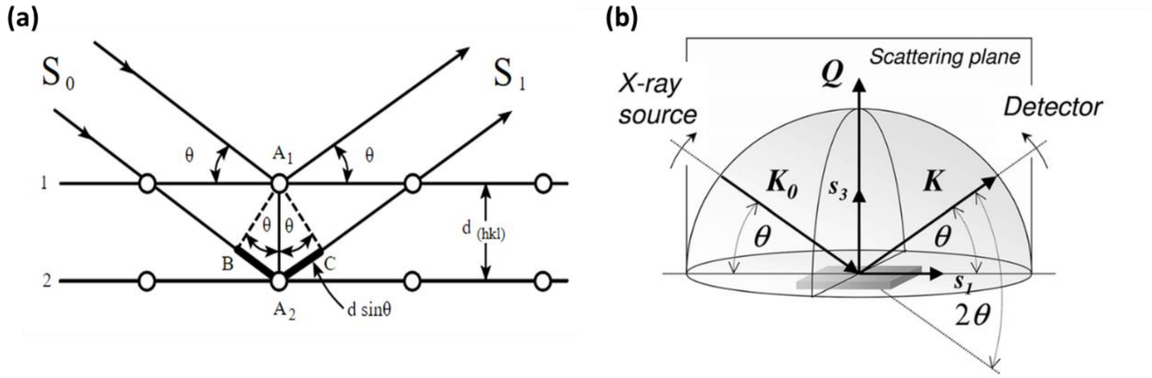

Figure 4.5. (a) Schematic representation of Bragg's Law. Incident X-rays elastically scatter off atoms in the lattice, and constructive interference occurs at angles that satisfy Bragg's Law (11). (b) Schematic representation of a θ-2θ scan (12).

Typically for a thin film polycrystalline material a θ - 2θ scan is performed which provides the position, shape, intensity, and phase of a material. Further analysis can provide information on strain and crystallite size. As shown in Fig 4.5b, in a θ - 2θ scan the sample is scanned with x-rays over a range of angles with the incident and exiting x-ray angles remaining the same during the scan.

4.2.1.1 XRD Strain Measurements. The interplanar spacing (d_o) of an unstrained lattice spacing will produce a pattern that is representative of the ideal diffraction pattern for that material. Frequently this is taken to be the powder diffraction pattern found in a database (159). A strained material will deviate from this “ideal” or reference diffraction pattern because of contractions or expansions in the crystal lattice. A change in d_{hkl} spacing resulting from atoms being displayed from their thermodynamic equilibrium positions will result in a shift in the diffraction peak due to a strain in the film (ε). The strain in a film can be calculated by the relative difference in the measured lattice spacing and the ideal lattice spacing (d_o):

$$\varepsilon = \frac{d_{hkl} - d_o}{d_o} \tag{20}$$

By altering the angle of the sample by an angle ψ strain along different planes can be measured:

$$\varepsilon_\psi = \frac{d_\psi - d_o}{d_o} \tag{21}$$

where ε_ψ is the strain in the plane at an angle ψ measured from the film plane , and d_ψ is the corresponding interplanar spacing. By measuring a diffraction peak at various ψ angles and taking their respective interplanar spacings, the stress (σ) can be determined in a technique referred to as the $\sin^2\psi$ method. However, some knowledge of the elastic properties of the material must be known (elastic properties of thin films often differ substantially from bulk values).

4.2.1.2 Low Temperature Annealing. Measuring the XRD pattern of samples *in-situ* during low temperature annealing can provide insight into the micro and macrostrain in a material through evaluating the FWHM, lattice parameters, texture, and diffraction angle as a function of annealing temperature. Increasing the temperature and measuring the diffraction pattern provides insight into the crystallization, relaxation behavior, and dissociation temperature of a material. On the other hand, by evaluating how the crystal changes after returning to room temperature provides details on the migration of interstitials and the stress mechanisms (defect, interfacial…,*etc*).

4.2.2 Scanning Electron Microscopy

A scanning electron microscope (SEM) uses a focused beam of electrons to scan the surface of a material releasing secondary electrons which scattered into a detector to create a secondary electron map which develops a high magnification image of the materials micro- or nanostructure. The wavelength of electrons can be on the order of 100,000 shorter than that of visible light. Therefore, the resolution of an SEM is far greater than that of an optical microscope. Micrographs are generated from a high energy beam of electrons scanned/rastered in a horizontal pattern on the target area. The incident electrons interact with atoms and electrons of the sample material producing characteristic x-rays, back-scattered electrons, secondary electrons, and Auger electrons which provide information on composition, microstructure, and morphology of a material.

Back scattered electrons (BSE) are produced by elastic interactions between the electron beam and the nuclei of the atoms in the imaged material. These electrons can scatter at angles up to 180° but typically at lower angles. Due to the mass disparity of electrons to various atomic nuclei, the amount of scattering is dependent on the size of the nucleus of a target atom with larger atoms generating a higher signal at the detector as they are a stronger scatterers of electrons.

For normal imaging, secondary electrons (SE) are detected. SE are generated via inelastic interactions between the incident electron beam and outer shell electrons of the target atoms and are defined as having energies of less than 50 eV. Outer shell, electrons after receiving enough kinetic energy from the electron beam, will be ejected from the imaged materials. These interactions occur at the surface (< 20 nm), while subsurface interactions are scattered and will not make it to the detector. The number of SE rise as the beam energy decreases. Generally, SE micrographs preserve spatial and lateral information due to the shallow sampling depth. Thus, high-resolution images can be generated with SE imaging.

4.2.3 Atomic Force Microscopy

Atomic force microscopy (AFM) provides nanoscale profiling of the surface topography of coatings and is a subset of operation of scanning probe microscopy (SPM). In addition to surface characterization, material properties such as Young’s modulus can be gathered from SPM measurements using specifically designed tips and applying varying forces to the tip. AFM utilizes a cantilever with a fine tip with radius of curvature typically >15nm. As the tip approaches the sample it will experience an attractive Van der Waal's force. This is caused by local polarization of atoms to the tip resulting in an attractive interaction, and generally. The interactions at the tip can be described by the Lennard-Jones potential. After reaching a critical distance from the sample's surface, the tip will experience a repulsive force driven by the electrostatic interactions of the interfacial electronic orbitals. This zone of repulsion is referred to as the contact regime and is used when measuring in contact mode. In contact mode the AFM tip is said to be in physical contact with the sample surface and nearly atomic level topography of surfaces can be mapped.

4.2.4 Structure/Microstructure/Topography Experimental Conditions

4.2.4.1 XRD. The crystal structure of as-deposited oxide films deposited on 316 SS substrates were analyzed by XRD (Panalytical Empyrean, USA) with a Cu-Kα radiation source (45 KV, 40 mA). The data were collected in the 2θ range of 20-90°. The XRD patterns were analyzed with X'Pert HighScore (Panalytical, USA) analysis software (160).

4.2.4.2 XRD Low Temperature Annealing. Thermal annealing of the as-deposited PdO deposited on Al_2O_3 and SiO_2/Si substrates was performed with a high temperature chamber (Anton Paar HTK 1200N, AT) back-filled with Ar gas. The peak corresponding to the (011) orientation was monitored. The (011) diffraction data were collected as the temperature was increased from 25 to 525°C at 25°C increments every

180s. Samples were then cooled from 525 to 25°C at 100°C increments. Subsequently, the diffraction data were collected.

4.2.4.3 Morphology. The surface and cross-sectional morphology of the as-deposited metal oxide films deposited on 316 SS and epi-polished c-axis Al_2O_3 substrates were examined with a field emission SEM (Thermo-Fisher Scientific APREO S , USA).

4.2.4.4 Surface Topography. Surface roughness measurements were performed on as-deposited single metal oxide films deposited on 316 SS substrates with an AFM (Jeol SPM 5200, JP) equipped with a reflective aluminum-coated silicon probe (Ted Pella CONTAL-G, U.S.A) operated in contact mode. Subsequent data were processed with Gwyddion SPM software (161), and the roughness is presented as the mean surface area roughness (S_a) in accordance with ISO 2517-2 (162).

4.3 Compositional Analysis

Energy dispersive spectroscopy (EDS) measures the characteristic X-rays generated by transition of outer shell electrons to vacancies (created by the SEM electron beam) in the inner shell electrons of a sample (163,164). The energy of the incident electrons (E_o) is lost when it collides with an electron in the inner shell which transfers an amount of energy (E) to the bound electron ejecting it from the nuclei. The vacancy in the inner shell is then filled by an outer shell electron. The energy of an X-ray is associated with the transfer of an electron from a higher energy shell to a lower energy shell. E_o must be greater than critical energy (E_{crit}) needed to dislodge electrons from the inner shell and thereby generate characteristic X-rays. For EDS E_o should be twice of the E_{crit} to excite enough x-rays for analysis. Since X-rays are generated by the inner-shell electrons, their energy is dependent on the Z number (proton number). This is described by Moseley's Law (165) for transitions from the L-shell to the K-shell (so-called K_α-lines):

$$E = 0.75(Z - 1)^2 \times 13.6\ \text{eV} \tag{22}$$

which states that the energy of a characteristic X-ray line varies approximately with Z^2, with the total intensity divided into several lines. For elements with $Z < 35$ approximately 80% of the intensity is observed in the $K_{\alpha1}$ and $K_{\alpha2}$ lines, while for elements with $Z > 35$, the intensity is divided between the $L_{\alpha1}$ and $L_{\alpha2}$ lines due to system limitations and avoiding electron energies that could damage the sample.

4.3.1 Compositional Analysis Experimental Conditions

The elemental composition of the as-deposited metal oxide films was determined by energy dispersive spectroscopy (EDS) (Oxford Instruments, Ultim Max, U.K.) deposited on 316 SS substrates. An acceleration voltage of 20 keV and beam current of 6.4 nA were used. The L_α lines for PGMs and K_α lines for oxygen were used to semi-quantitatively measure changes in the composition resulting from varying the WPs and OPPs. In this study, the oxygen content is presented as the atomic percent of oxygen (at. %) measured in the films, and the metal concentration in the binary and ternary metal oxide films is reported as the metallic ratio of metals based on at. %.

4.4 Tribological Background and Experimental Conditions

For a film to properly perform its desired function for most applications it must remain adhered to the substrate. Thus, it is necessary to assess the adhesion of a film when strong adhesion is desired. The ASTM D3359 tape test provides a general guideline to assess adhesion of a film on a metal substrate (13). The method is a simple liftoff technique where a piece of specified tape is adhered to a substrate. The tape is left to settle for up to 120 s and swiftly peeled off at 180° (backwards). The adhesion of the film can be assessed on a percentage scale or a ranked scale where lower values indicate better adhesion. For this thesis, the ASTM standard was used as a guideline and the adhesion suitability was assessed by visual inspection. The tape used in this study was 610 Scotch tape (3M, U.S.A.) on selected samples deposited on 316 SS foil substrates.

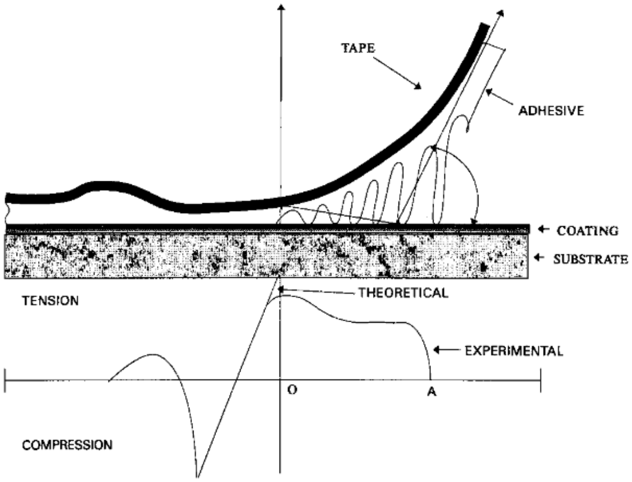

Figure 4.6. ASTM D3359 3M adhesion tape test peel profile (13)**.**

4.5 Biocompatibility

Biocompatibility studies involve testing either the material, its extracts, or both depending on the nature of the end-use. *In-vitro* cell culture studies are usually the first step of evaluating biocompatibility. The cytotoxicity studies were performed in accordance with the ISO-10993-5 (166) standard for biomaterials and medical device testing.

4.5.1 Biocompatibility Experimental Conditions

The single metal oxide materials were evaluated for cytotoxicity, along with silicon (Si) and copper (Cu) which were used as negative and positive controls for cell viability, respectively. The test materials were sputter coated onto wells of otherwise untreated six-well cell culture plates (VWR® Tissue Culture Plates, USA). The coating was done such that only one row of the wells were coated and the other row was left uncoated for a sham comparison. After coating the plates were sterilized by exposure to UV light for 15 min.

A sub-cloned, immortalized neuronal cell line generated by hybridization of mouse neuroblastoma and post-mitotic rat dorsal root ganglion (DRG), ND7/23 was chosen for the studying the biocompatibility of films. These cells are commercially available and expresses low-voltage activated calcium channels making them it useful as a model of neuromodulation-based sensory neuron firing. Cells in culture were split at about 90 % confluence with 0.25 w/v% Trypsin-EDTA. The cells were resuspended in Dulbecco's modified eagle's medium supplemented with 10 vol% fetal bovine serum and 5 vol% penicillin-streptomycin solution and seeded in the coated and uncoated wells. The cells were seeded at a concentration of 50×10^4 cells/mL and incubated at physiological conditions. For samples that were incubated for more than 24 h, the media was changed every two days.

As prescribed by the ISO 10993, cytotoxicity was evaluated by the alamarBlue™ cell viability assay. The cells were incubated for 1, 3, and 7 days. After the period of incubation, the alamarBlue™ reagent was added at 10 vol% and incubated for 5 h. The media solution was then transferred to a 96-well plate, and the absorbance was read with a microplate reader at 570 nm and 650 nm reference. The number of viable cells was obtained by comparing the absorbance of the sample wells to the standard. The percentage of viable cells was calculated by dividing the number of cells from the coated wells by the number of cells from the corresponding uncoated wells and multiplying by 100.

Chapter 5

Single Metal Oxide Thin Films

This chapter outlines the results for the single metal M-oxide (M = Ir, Pd, Ru, Rh) coatings. An investigation of the effect of power density on IrO_x thins films was performed first. This was followed by an investigation of the effects of WP and OPP on the electrochemical properties, microstructure, composition, and crystal structure of the single metal oxide films. Optimal synthesis parameters which resulted in favorable electrochemical properties and structures were identified.

5.1 Iridium Oxide Thin Films

The following sections outline the effects of cathode power density, sputtering WP, and sputtering OPP on the morphology, composition, microstructure, crystal structure, and electrochemical properties of IrO_x thin films.

5.1.1 Power Density Dependence

In the following sections the effect of the pulsed-DC power density on the deposition rate, microstructure, crystal structure, and CSC of IrO_x thin films are discussed.

5.1.1.1 Iridium Oxide Power Density Synthesis. All depositions were performed at ambient substrate temperature with an Advanced Energy Pinnacle Plus pulsed-DC power supply at power densities of 2.5, 4.9, 7.4, and 9.9 W/cm^2 (as calculated from the full target area of ~20.3 cm^2) at a range of reverse periods and frequencies provided in Table 5.1. Fig. 3.4 provides an illustration of the ideal pulsed-DC waveform and defines the three quantities varied during the study. T_{cycle} is the duration of one full cycle, which is the inverse of the f ($1/f$); T_{rev} is the length of time that the pulse amplitude is reversed during one cycle, and T_{on} is the duration of the sputtering process during one cycle ($T_{on} = T_{cycle} - T_{rev}$). Two T_{rev} values were selected for each f to reduce the duty cycle ($100 \times (T_{cycle} - T_{rev})/(T_{cycle})$) to approximately 60% and 75% as shown in Table 5.1. The targeted duty cycles were selected to investigate how films properties may change as duty cycle is decreased. The lower limit for the duty cycle was limited by power supply constraints.

Table 5.1

Pulsed DC Sputtering Parameters

Frequency (kHz)	DC	140	140	250	250	350	350
Reverse Period (µs)	DC	1.8	3.2	1.0	1.6	0.7	1.1
Duty Cycle (%)	100	75	55	75	60	76	62

Reactive magnetron sputtering was performed in a mixture of argon and oxygen gases. The gas mixture was maintained at 95% OPP with an overall WP of 10mTorr. This OPP was selected to ensure the target was being sputtered in compound (poisoned) mode. The overall gas flow-rate ($Ar + O_2$) was held constant at 50 sccm. A summary of the target and sputtering condition specifications are provided in Table 5.2.

Table 5.2

Deposition Conditions for Iridium Oxide Films

Parameters	Details
Target	Ir (99.95%)
Working Pressure (mTorr)	10.00
Oxygen Partial Pressure (%)	95.00
Ar Flow Rate (sccm)	2.50
Oxygen Flow Rate (sccm)	47.50
Iridium Power Density (W/cm^2)	2.5, 4.9, 7.4, 9.9
Deposition Time (min)	15

5.1.1.2 IrO_x Power Density Results and Discussion. Many of the differences in coating properties can be attributed to the changes in particle flux and energy between the power densities, as indicated from the discharge voltage and current response of the power supply shown in Fig. 5.1.

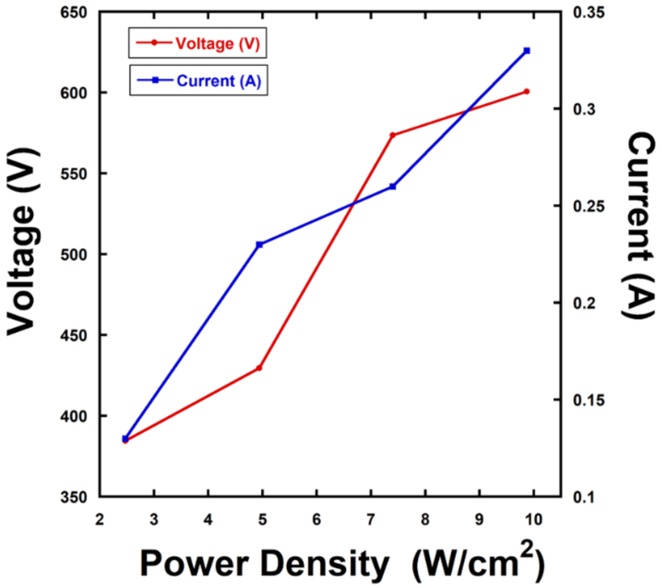

Figure 5.1. Voltage and current responses recorded from the power supply for IrO_x deposited using DC sputtering at the four power densities.

For instance, the incident Ir atoms during deposition of films synthesized at 2.5 and 4.9 W/cm^2 have decreased adatom mobility because of lower cathode discharge energies and landing energies. As a consequence, the coatings were more amorphous and possessed smaller grain sizes at lower power densities. Conversely, films were more crystalline at higher power densities; these characteristics are observed in the SEM micrographs and revealed in the XRD patterns shown in Fig. 5.2 and 5.3, respectively.

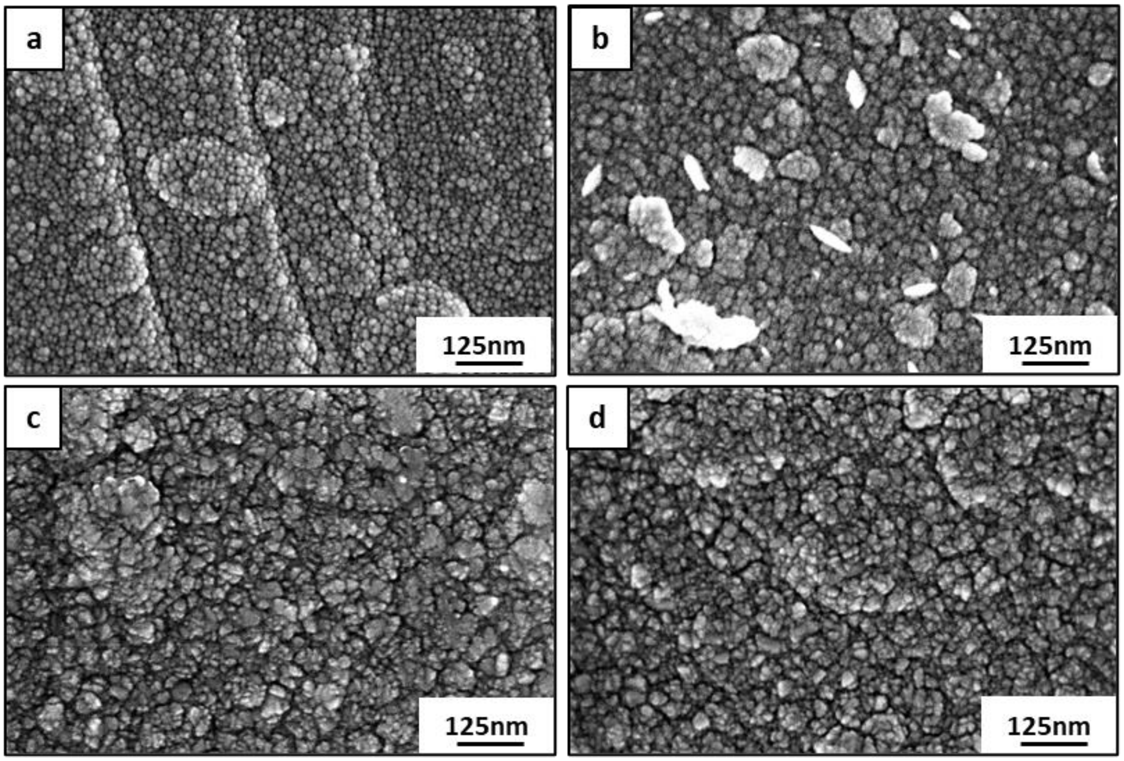

Figure 5.2. SEM micrographs of IrO_x synthesized by reactive DC magnetron sputtering at power densities of (a) 2.5 (b) 4.9 (c) 7.4 (d) 9.9 W/cm^2.

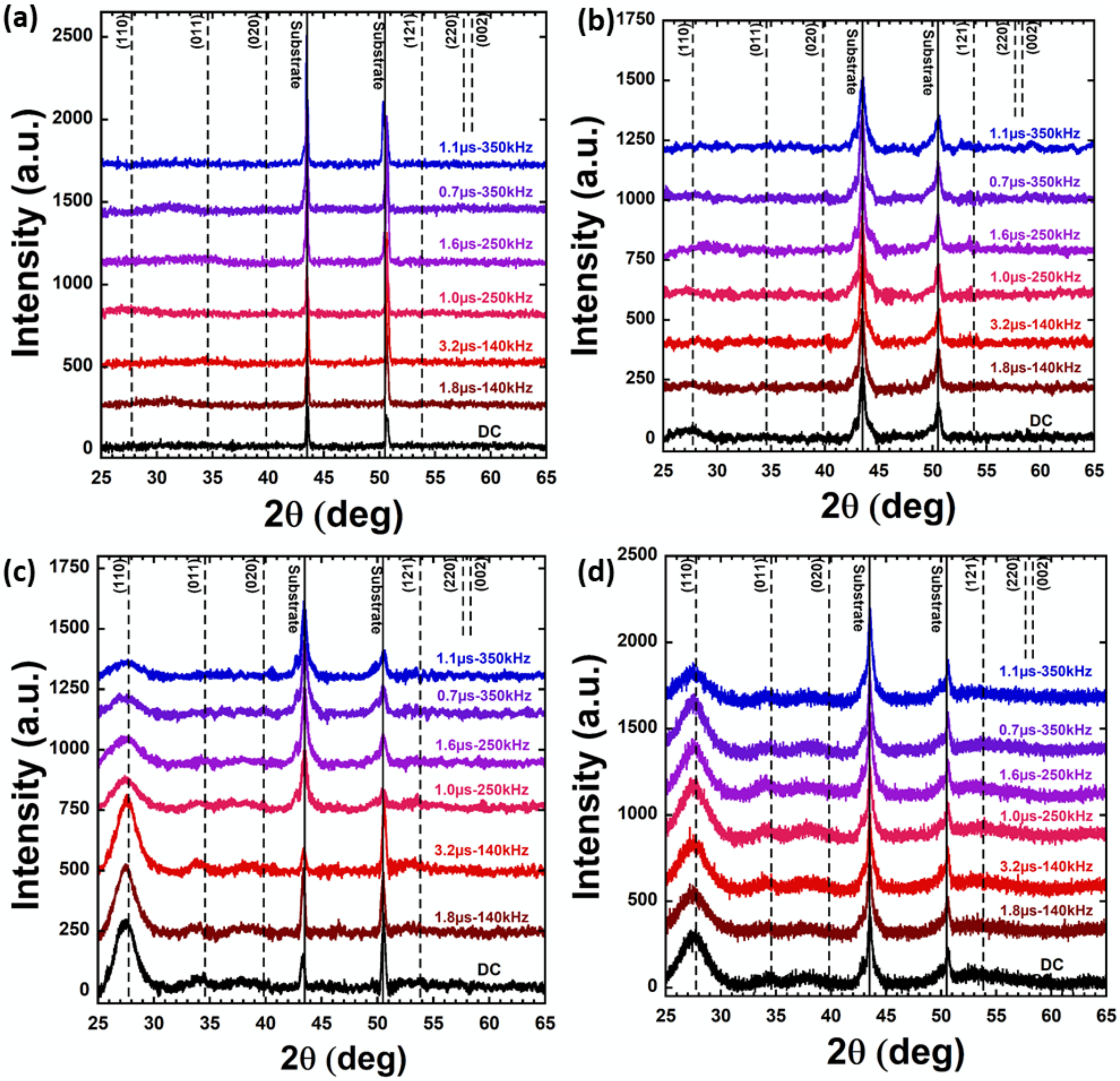

Figure 5.3. X Ray diffraction patterns (offset for better comparison of T_{rev} and frequency) of DC and pulsed DC IrO_x films synthesized at power densities of (a) 2.5 W/cm^2 (b) 4.9 W/cm^2 (c) 7.4 W/cm^2 (d) 9.9 W/cm^2. The dotted vertical lines represent the reference angles for tetragonal IrO_2 (167). The substrate diffraction peaks are represented by the solid black lines.

Sputtering at lower power densities results in a greater amount of oxygen within the deposited IrO_x layer shown in Fig. 5.4. This is due to a lower number of incident Ir atoms and a reduced frequency of preferential resputtering of adsorbed oxygen. On the other hand, coatings synthesized at 7.4 and 9.9 W/cm^2 had higher incident particle flux and energy resulting in increased adatom mobility, increased residual heating, and a greater amount of preferential resputtering. The combined results of these effects are evident in the SEM micrographs, XRD patterns, and EDS analyses which show that the films deposited at higher power densities possessed larger angular grains, were more crystalline, and contained considerably less oxygen than their counterparts deposited at lower power densities.

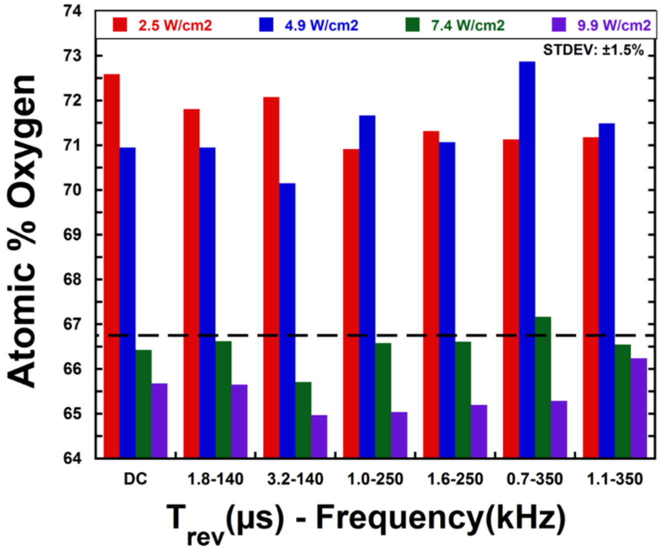

Figure 5.4. Oxygen content as measured by EDS in IrO_x films deposited by DC and pulsed DC sputtering. The horizontal dashed line represents the oxygen content expected from stoichiometric IrO_2.

The disparity in the CSC between the 2.5 and 4.9 W/cm^2 (low power density), and 7.4 and 9.9 W/cm^2 (high power density) IrO_x films shown in Fig. 5.5 have been attributed mainly to the differences in surface morphology and crystal structure. The apparent increased roughness from the radial grains is believed to increase the ESA and hence the number of electrochemically active sites, thereby improving electrochemical performance in lower power density IrO_x films. Conversely, improved crystallization and associated larger grain sizes decreases the number of electrochemically active sites, thus reducing the CSC in the 7.4 and 9.9 W/cm^2 films. However, as implied by the XRD results of the lower power density films, the generally greater electrochemical performance in the 4.9 W/cm^2 over the 2.5 W/cm^2 coatings under both DC and pulsed-DC conditions suggests that some amount of ordering in the crystal is beneficial. However, the extent of influence of the stoichiometry, that is the ratio of Ir : O, on electrochemical performance is unclear. It is worth noting that the highest electrochemically performing coatings are those with Ir:O content notably above stoichiometric IrO_2. This may indicate that the electrochemical performance could be partly influenced by a deficit or surplus of oxygen ions with respect to the iridium within the IrO_x microstructure.

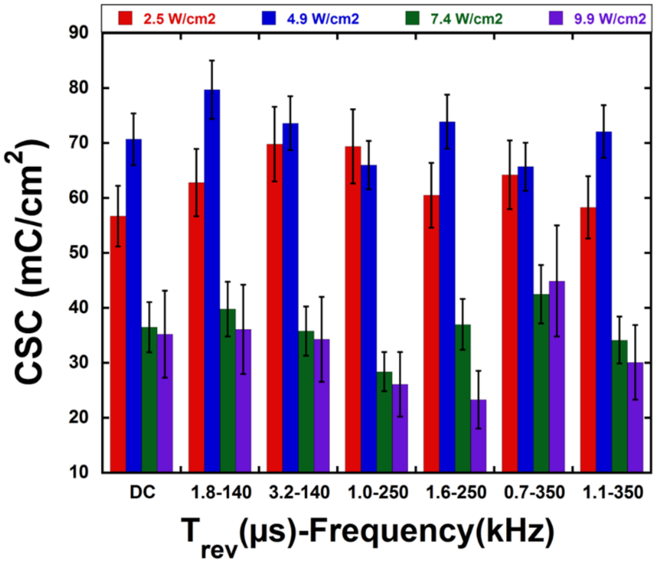

Figure 5.5. Total CSC obtained from cyclic voltammetry recorded in 0.1M PBS solution at a sweep rate of $0.1Vs^{-1}$ of IrO_x films deposited by DC and pulsed DC sputtering.

The charge transfer of IrO_x is proposed to occur via cyclic reduction/oxidation between the Ir^{3+} and Ir^{4+} states of the oxide (however multiple oxidation states could be active). The presence of excess oxygen in the IrO_x layer should push the IrO_x from mixed Ir^{3+}/Ir^{4+} to purely Ir^{4+} material, which has greater electronic conduction and availability of Ir^{4+} for redox charge transfer as shown in the possible redox equations:

$$\mathrm{Ir^{3+}:\ Ir_2O_{3(s)} + H_2O_{(aq)} + 2e^- \rightleftharpoons 2IrO_{(s)} + 2(OH)^-_{(aq)}} \tag{23a}$$

$$\mathrm{Ir^{4+}:\ 2IrO_{2(s)} + H_2O_{(aq)} + 2e^- \rightleftharpoons Ir_2O_{3(s)} + 2(OH)^-_{(aq)}} \tag{23b}$$

$$\mathrm{Ir^{4+}: IrO_{2(s)} + 2H_2O_{(aq)} + 4e^- \rightleftharpoons Ir_{(s)} + 4(OH)^-_{(aq)}} \tag{23c}$$

5.1.1.3 IrO_x Power Density Summary and Conclusions. The surface morphology, crystal structure, chemical composition, and electrochemical properties of IrO_x films were shown to be strongly influenced by the deposition power density. Clear trends were evident when considering films deposited at lower versus higher power densities with coatings deposited at 2.5 and 4.9 W/cm^2 power densities possessing greater charge storage capacity and thus are more favorable. The optimal pulsed-DC parameters which resulted in high CSC and complete arc suppression were identified to be the lower power densities (2.5 - 4.9 W/cm^2) at a f of 140 kHz and T_{rev} of 1.8 μs (based on deposition rate and arc suppression).

5.1.2 Pressure Dependence

In the following sections the effect WP and OPP on the topography, microstructure, crystal structure, composition, and electrochemical properties of IrO_x thin films are discussed. Wulff constructions and interpretation (in part) were performed by Ludovic Briquet (Johnson Matthey, Inc.) in support of this investigation.

5.1.2.1 Results and Discussion. The microstructure of IrO_x films synthesized at a 5 mTorr WP and 20, 50, and 80% OPPs are presented in the SEM micrographs shown in Fig. 5.6. As shown in Fig. 5.6a, IrO_x films synthesized at 20% OPP develop nanosized grains with nearly indistinguishable grain boundaries leading to a relatively dense morphology. The microstructure of IrO_x films synthesized at 50 and 80% OPP and 5 mTorr WP are shown to develop nanosized spherical grains which become increasingly distinguishable with increasing OPP as shown in Fig. 5.6b and 5.6c.

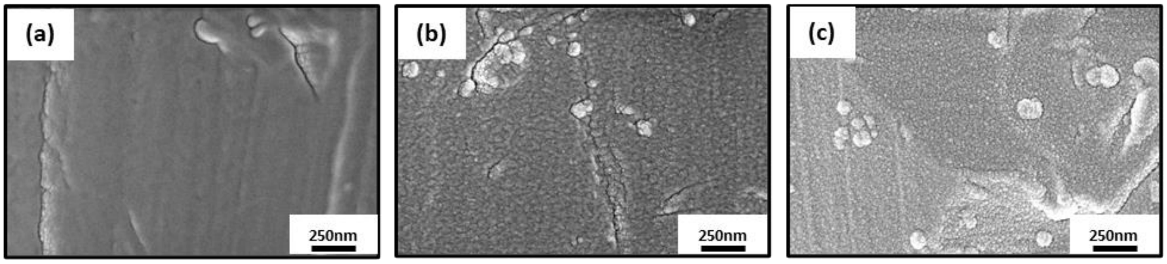

Figure 5.6. SEM micrographs of reactively sputtered IrO_x films deposited on 316 SS substrates synthesized at 5 mTorr and (a) 20% (b) 50% and (c) 80% OPPs.

The morphology of IrO_x films is notably altered when synthesized at 30 mTorr WPs. The first transformation is at 20% OPP as presented in the micrograph shown in Fig. 5.7a. The microstructure no longer consists of tightly packed nano-spherical grains as is the case for films deposited at 5 and 10 mTorr (not shown). Instead, the microstructure was dominated by spherical nanosized grains which grow into large spherical clusters and possess large voids between boundaries that ranged anywhere from

10 to 150 nm in length. The cross-sectional micrograph of the 20% OPP and 30 mTorr films, shown in Fig. 5.8a revealed films when synthesized under these conditions develop a porous columnar substructure. In addition to the large spherical grain clusters, films deposited at 20% OPP and 30 mTorr WP display a secondary type of microstructure referred to as nanoflake or platelet microstructure shown in Fig. 5.8b for films deposited at 30 mTorr and 80% OPP. The presence of nanoflake microstructure is highlighted in films dominated by nano-spherical grain clusters (20% OPP and 30 mTorr WP) shown in Fig. 5.7a.

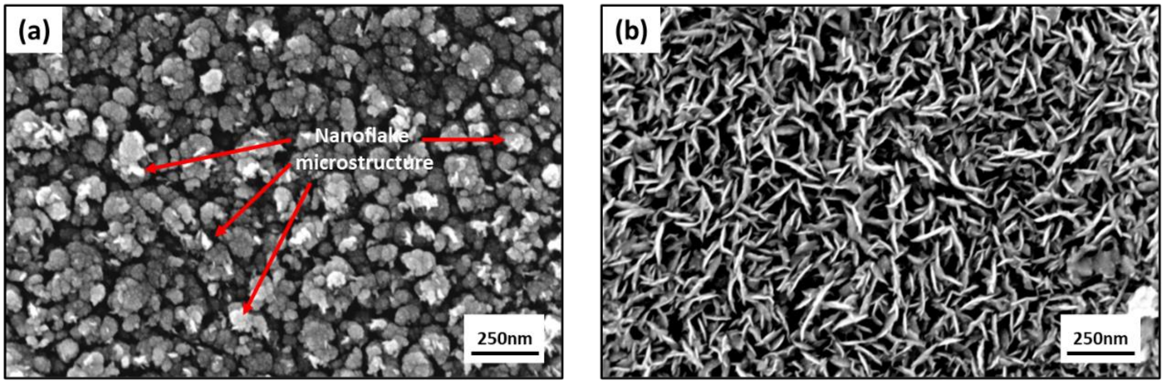

Figure 5.7. SEM micrographs of reactively sputtered IrO_x films deposited on 316 SS substrates and synthesized at 30 mTorr WP and OPPs of (a) 20% and b) 80%.

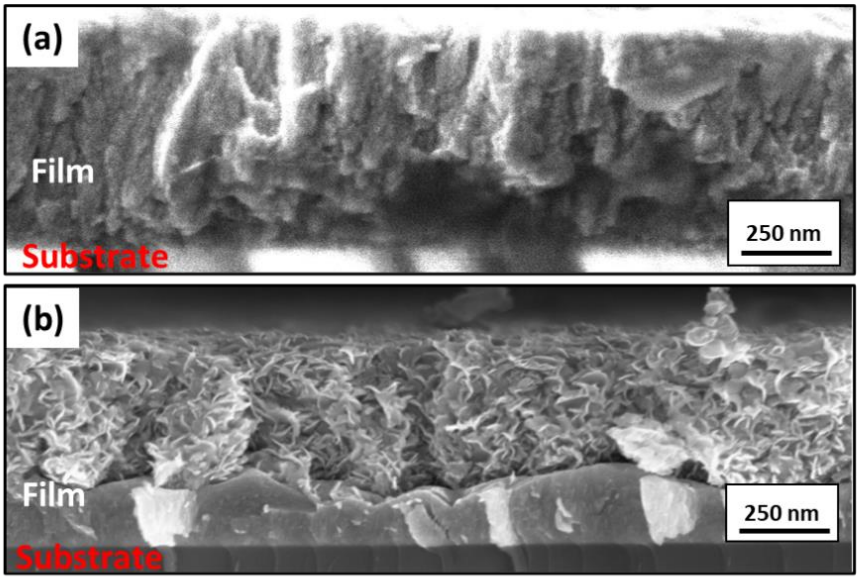

Figure 5.8. Cross-sectional SEM micrographs of IrO_x films synthesized at 30 mTorr WP and (a) 20% OPP (b) 80% OPP IrO_x deposited on Al_2O_3 substrates**.**

Another important characteristic that can be identified from the SEM micrograph of IrO_x synthesized at 20% OPP and 30 mTorr WP is a large amount of variation in surface topography (and greater ESA) and thereby higher surface area. These characteristics are confirmed with the AFM roughness measurements and topographs shown in Fig 5.9a-b.

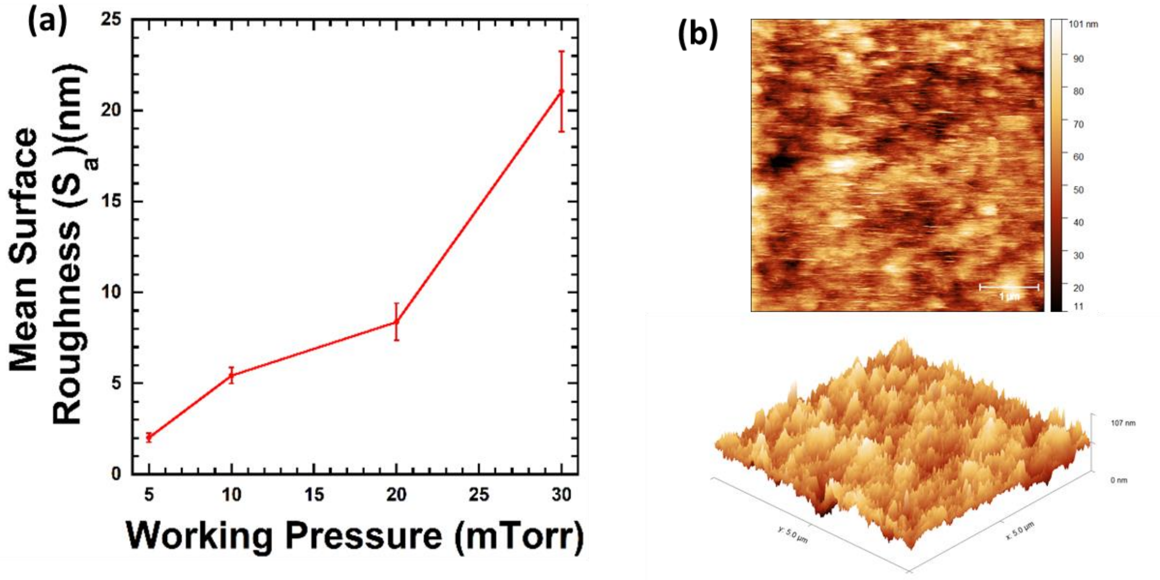

Figure 5.9. (a) Mean surface roughness (S_a) of IrO_x films deposited measured on 316 SS substrates and deposited at 20% OPP.(b) AFM topography of as-deposited IrO_x deposited on 316 SS and synthesized at 20% OPP and 30 mTorr WP.

The microstructure of IrO_x changes considerably when synthesized at 50 (not shown) and 80% OPP and at 30 mTorr WP as shown in Fig. 5.7b. The aforementioned nanoflake microstructure which had sporadic growth at 20% OPP and 30 mTorr, dominates in the higher OPP films with no indications of the granular microstructure present (similar microstructural changes occur in films synthesized at 20 mTorr over similar OPP ranges). The cross section shown in Fig. 5.8b reveals that nanoflake microstructure possesses a high surface area and grows from a more densely packed sublayer.

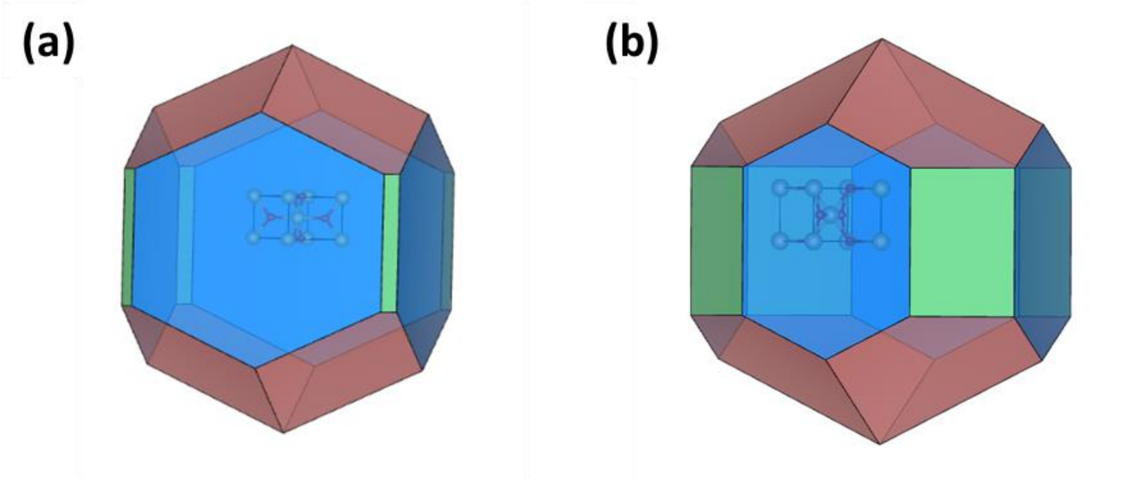

Figure 5.10. Wulff construction of IrO_2 based on (a) pristine surfaces in vacuum (b) when adsorbing O_2 at 80% OPP and 10 mTorr. Blue, red, and green correspond to the (110), (011), and (100) surfaces, respectively.

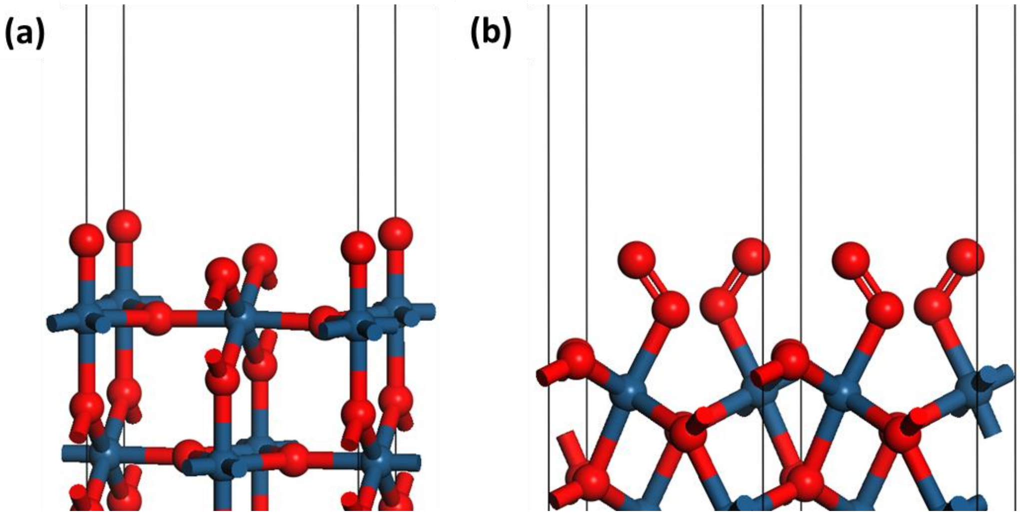

Figure 5.11. Most stable structure for the (a) (110) and (b) (011) rutile IrO_2 surfaces. Dark blue spheres represent Ir atoms; red spheres represent oxygen atoms.

Table 5.3

Surface Energies of IrO_2 and Stability Ratio

Surface	Pristine (J/m^2)	80% OPP (10 mTorr)
(110)	1.48	1.00
(011)	1.77	1.20
(100)	1.99	1.35
(001)	2.55	1.73
(111)	2.57	1.74

In an effort to better understand the nanoflake growth, Wulff constructions which relate the crystallite orientation to the surface energy were modeled for tetragonal rutile IrO_2 (Fig. 5.10), and the corresponding surface energies are presented in Table. 5.3. The stability of the surfaces was calculated by computing the surface energy G_{surf}, pressure P, and surface coverage α of the oxygen adlayer according to the following thermodynamic relations for the free energy of an adsorbing surface:

$$G_{surf} = VdP - SdT + \gamma_{hkl}^{int} dA + \sum_i \mu_i dn_i \tag{24a}$$

$$\gamma_{hkl}^{int} = \gamma_{hkl} + \alpha \frac{E_{ads}}{A_{at}} \tag{24b}$$

$$\text{Width of facet} \propto \frac{1}{\gamma_{hkl}^{int}} \tag{24c}$$

$$\text{Stability ratio} = \frac{\gamma_{110}}{\gamma_{hkl}} \tag{24d}$$

where temperature T was assumed to be 298.15 K, γ_{hkl}^{int} is the interfacial energy, γ_{hkl} is the energy required to create a surface normal to the [*hkl*] vector, E_{ads} is the energy of adsorption, and A_{at} is the area occupied per surface atom, and μ_i is the equilibrium chemical potential related to the partial pressure of the gas mixture. The Wulff construction shown in Fig. 10a is for a pristine IrO_2 tetragonal rutile crystallite in vacuum. Taking into consideration the width of each face and the stability ratios of the surfaces, the (110) surface is shown to be the most stable followed by the (011) though it is considerably less stable. At 80% OPP however, as shown in Fig.5.10b, the width of the (110) surface shrinks, and the (011) face becomes the most stable surface. Further analysis of the surfaces and corresponding structures reveals that the (110) surfaces dissociate adsorbed oxygen (Fig. 11a), while the (011) surface does not (Fig.11b). This difference in chemisorptive behavior of the surfaces may explain the subsequent nanoflake microstructure of the (011) surface. In the context of the sputtering parameters investigated in this thesis, the growth of the (011) orientation can be promoted by sputtering at higher OPPs, increased WPs (increasing the adlayer and residence time of oxygen), or both.

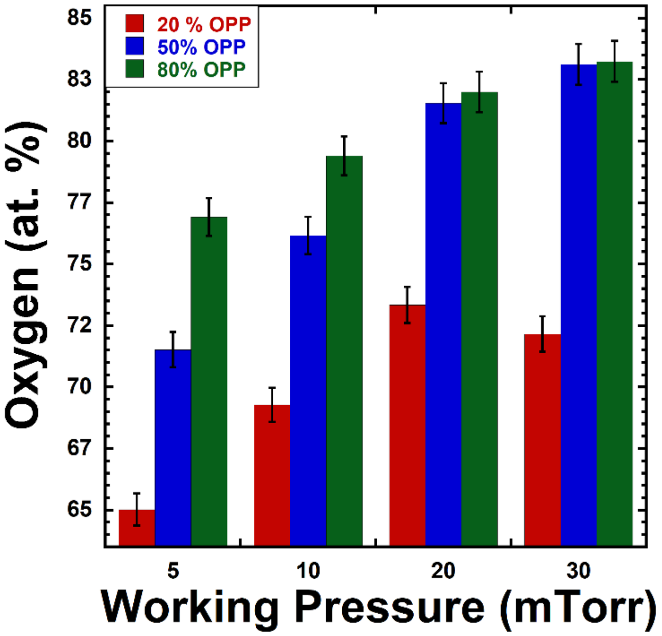

Figure 5.12. Oxygen content in films as measured by EDS for IrO_x deposited on 316 SS.

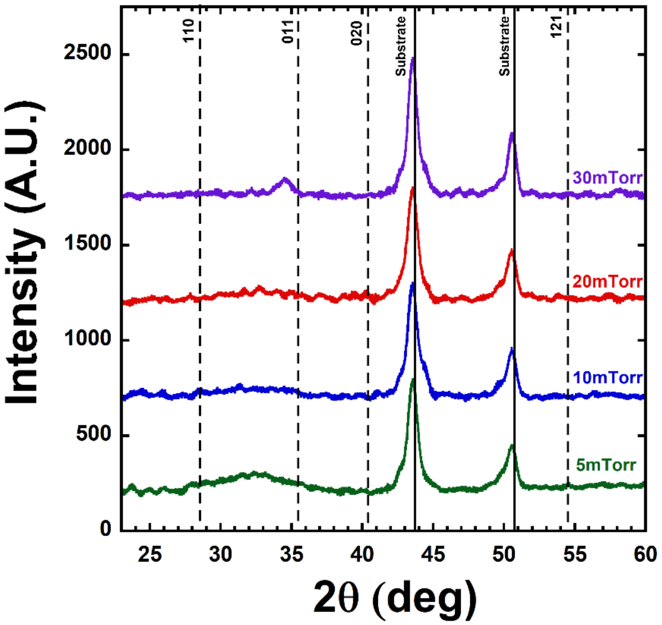

Figure 5.13. IrO_x films deposited on Al_2O_3 substrates synthesized at 20% OPP and 5, 10, 20, and 30 mTorr WPs; dashed lines represent reference angles IrO_x (168); solid lines denote substrate diffraction peaks.

Despite the films measuring over-stoichiometric oxygen content (Fig. 12), the presence of the (011) surface is observed in the XRD patterns shown in Fig. 5.13 for the as-deposited IrO_x films deposited at 20% OPP and 30 mTorr WP, confirming the growth of the rutile IrO_2 and a change in the surface energy of films from deposition at increased WPs and OPPs.

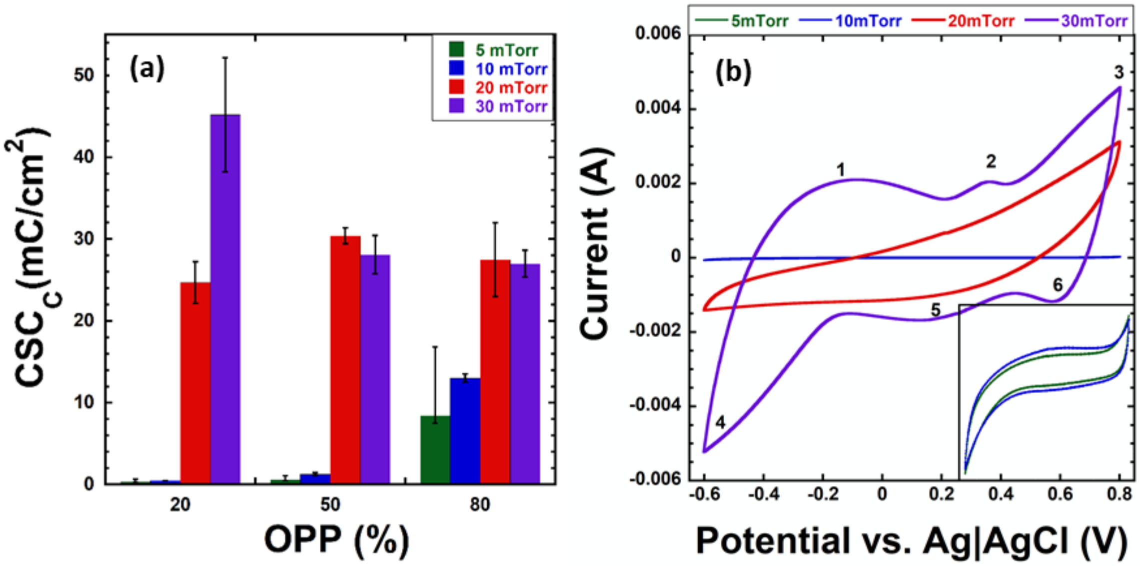

Figure 5.14.(a) Evolution of CSC$_C$ with increasing WP and OPP for IrO$_x$ films deposited on 316 SS substrates obtained from CV measurements. (b) Typical cyclic voltammograms (20th cycle) IrO$_x$ films deposited on 316 SS substrates and synthesized at 20% OPP and 5, 10, 20 and 30 mTorr WPs; voltammograms and inserts for lower pressure films are rescaled for better comparison. The numbers on the 30 mTorr profile represent the peak potentials.

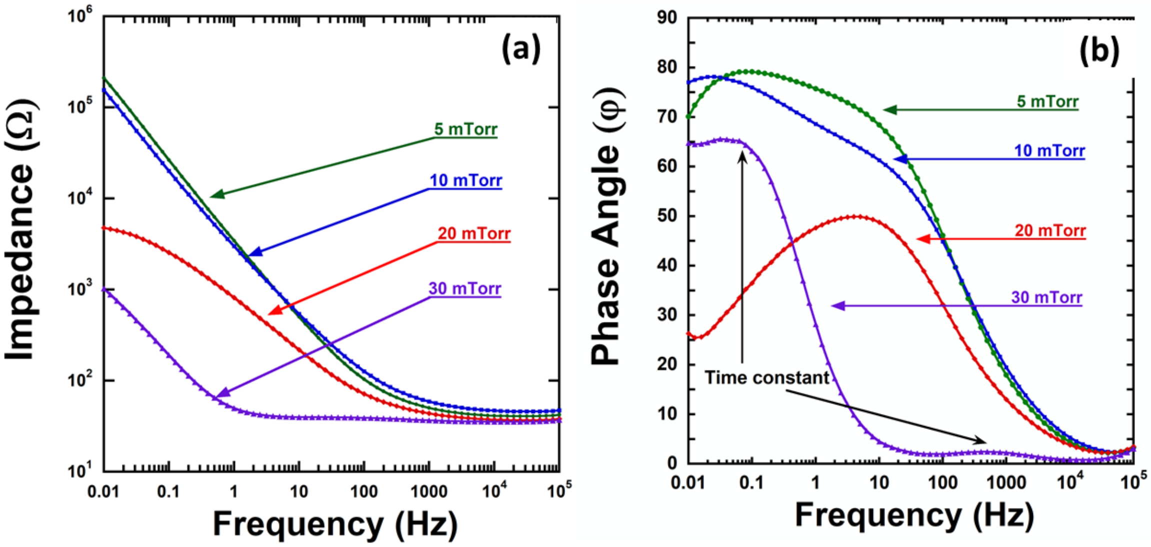

Figure 5.15. EIS spectra Bode modulus plots for (a) the impedance magnitude (b) phase angle for IrO$_x$ films deposited on 316 SS substrates and synthesized at 20% OPP.

The changes in the electrochemical properties are shown in the cathodic charge storage capacity (CSC_C) (Fig. 5.14a) and the EIS spectra (Fig. 5.15). It is clear from the CSC_C measured in films shown in Fig. 5.14a that deposition of films at higher WPs results in higher electrochemical performance. On the other hand, low sputter deposition performed at the lower two WPs result in films with considerably lower CSC_C. There is a notable increase in electrochemical performance at the low WP for films deposited at 50 and 80% OPP. This is attributed to the presence of the additional surface area provided by the nano-spherical grain clusters and nanoflake microstructure. The difference the CSC_C performance of coatings between the higher WPs, specifically those deposited at 30 mTorr are attributable to the difference in microstructure and therefore the ESA between the 20 and, 50 and 80% OPP films. Additional changes in the electrochemical response of coatings are evident in the CV curves for films deposited at 20% OPP shown in Fig. 5.14b. The 5 and 10 mTorr, 20 mTorr, and 30 mTorr WP coatings each display characteristically different curves. For instance, for the films synthesized at lower 5-20 mTorr WPs the peak currents relating to IrO_x are not visible, indicating a comparatively slower reaction rate for these films. However, for films synthesized at 30mTorr WP the redox reaction rate of films increased. This is indicated by the presence of the 2-5 redox peak currents shown in Fig. 5.14b which are clearly visible and can be attributed to the Ir(III)/Ir(IV) redox couple (although additional reactions are possible as suggested by the various redox couples from Eqns. 23a-c).

This transition in the electrochemical response of films as a function of WP is evident in the EIS spectra as shown in the Bode plots for the 20% OPP films presented in Fig. 5.15a-b. A clear divide in the impedance response, particularly at the lower frequency range between the 5 and 10mTorr, and the 20 and 30 mTorr WP films, is evident as shown in Fig.5.15a. Films deposited at 20 and 30 mTorr possessed considerably lower impedance than their lower WP counterparts. This lower impedance response has been attributed to the apparent increase in porosity that developed in the higher WP coatings. The Bode phase angle plots shown in Fig. 15b further elucidates and confirms the differences in the electrochemical properties of films deposited at different WPs. The phase angle response for the lower WP films indicates a pseudo-double layer capacitive process (adsorption of counter ions on an "impermeable" surface) at low frequencies as determined by the higher phase angles, suggesting the 5 and 10 mTorr films behave more as passive coatings. This at least partially explains their notably low CSC_C. The transition in electrochemical response is most evident in the Bode phase angle plot for the 20 mTorr films which showed a mixed kinetic-diffusion response with a large kinetically slow driven faradaic peak spanning from high to mid frequency which tapered off to lower angles at low frequencies indicating diffusion control. Finally, the phase angle response for the 30 mTorr films possesses two-time constants which indicates two distinct capacitive processes. The first time constant evident and dominant at higher frequencies is likely related to the fast faradaic reactions occurring at the electrode surface (which is also indicated by the peak potentials). The second time constant may be related to slower kinetically driven processes. Additionally, the higher phase angle at lower frequencies indicates that the films behave more capacitively at low perturbations. This is likely caused by trapping of solution in pores causing a larger "pore" capacitance (which is a pseudo-double layer response related adsorption of counterions).

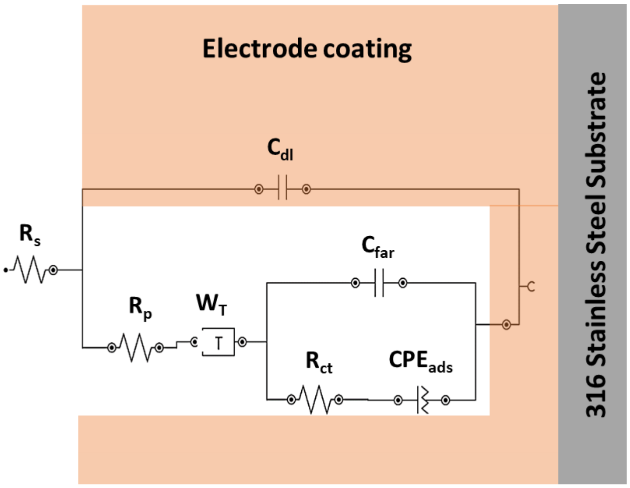

Figure 5.16. Equivalent circuit models (ECM) IrO_x synthesized at 20% OPP and 30mTorr WP.

The ECM for IrO_x films synthesized at 30mTorr is shown in Fig. 5.16, and the corresponding parameter values are provided in Table. 5.4. The model is physically significant considering the aforementioned evidence. The EC consists of a double layer capacitance element (C_{dl}) in parallel with an polarization resistance (R_p) relating to the adsorptive behavior of the electrostatic double layer capacitance, and a bounded Warburg element (W_T) to account for the surface and porous electrode-electrolyte interfaces relating to double layer impedance effects. The R_p and W_T branch is in series with a parallel RC component which accounts for the faradaic charge exchange (C_{far}) and charge transfer resistance (R_{ct}), respectively. An additional constant phase element is required (CPE_{ads}) that represents adsorption of counter-ions at the electrode-electrolyte interface (presumably within pores).

Table 5.4

ECM Elements and Impedance Values for IrO_x

Element	R_S	R_{dl}	W_T		C_{dl}	R_{ct}	C_{far}	CPE_{ads}	
Parameter	R (Ω)	R (Ω)	$Y_0(S\cdot s^{1/2})$	$B(s^{1/2})$	C (F)	R (Ω)	C(F)	Y_0 $(S\cdot s^N)$	N
Value[b]	36	3.2	0.079	1.3	7.6E-05	150	0.0076	0.0035	0.54

[a] Film Synthesized at 30mTorr WP and 20% OPP

[b] χ^2 : 0.01

The benefits of the mixed nanoflake and nanoflake microstructure, whether it be better redox characteristics, higher ESA, or both, are limited by their lack of suitable adhesion to the substrate and mechanical fragility when handled. These properties make these otherwise high performing coatings generally less suitable for use as electrode/microelectrode coatings for implantable neural interfacing applications. This poor adhesion and fragility are demonstrated by the 3M tape test outlined in section 4.4 and shown in Fig. 5.17. The nanoflake microstructure fails the 3M tape test while the non-nanoflake spherical nanosized grain microstructure passes. While this test may seem trivial, the adhesion and mechanical robustness of films are critical for the longevity, safety, and efficacy of implantable electrode devices.

Figure 5.17. ASTM D3359-02 & 3M tape test on IrO_x deposited on 316 SS at 80% OPP and 10mTorr with (top) non-nanoflake microstructure and (bottom) nanoflake microstructure.

5.1.2.2 Iridium Oxide Pressure Dependence Conclusions. The synthesis of IrO_x films at higher WPs and lower OPPs led to films with favorable electrochemical properties as measured by CV and EIS as shown in Table 5.5.

Table 5.5

Cathodic Charge Storage Capacity and Maximum Impedance of $IrO_x{}^a$

Working Pressure (mTorr)	5	10	20	30
CSC_C (mC/cm^2)	0.33 ± 0.033	0.46 ± 0.0042	25± 4.01	45 ± 7.01
Impedance (Ω)	210410	155210	4756	1036

[a] *Film Synthesized at 30mTorr WP and 20% OPP*

The surface microstructure was altered as a result of increased surface energy from the oxygen adlayer and as a consequence of the growth of the less stable (011) crystallite surfaces associated with nanoflake growth. Despite nanoflake microstructure being less desirable for use as an implantable neural interfacing electrode coating, it may be beneficial in some other applications. However, it has been demonstrated to be less suitable in applications where mechanical toughness and strong adhesion are important. The columnar substructures that develop at high WPs are predicted by the SZM (Fig. 3.11) and relate to Zone 1 or Zone T (for lower pressures and temperatures) depending on the exact sputtering conditions. Additionally, it is clear that synthesis at higher WPs and lower OPPs is favorable to the electrochemical performance of the films through increasing the ESA as well as activating higher oxidation states as indicated by SEM, CV, EIS, and ECM analyses. Thus, the synthesis parameters which considerably enhanced the electrochemical properties of IrO_x while still maintaining suitable microstructure and mechanical properties are 30 mTorr WP, 20% OPP, and cathode power densities ≤ 4.9 W/cm^2.

5.2 Palladium Oxide Thin Films

In the following sections the effect WP and OPP on the topography, microstructure, crystal structure, composition, and electrochemical properties of PdO thin films are discussed. The synthesis parameters for PdO are outlined in sections 3.4.1.

5.2.1 Results and Discussion

The PdO oxide system offers unique insight into the growth of the binary PGM oxide thin films. PdO features large grain sizes and a high degree of crystallinity when compared to the other three single metal oxide systems studied. PdO films synthesized at 5 mTorr develop two distinct microstructures as shown in Figs. 5.18a-c. When synthesized at 20% OPP (Fig. 5.18a), PdO films develop large radial shaped particles with a layered growth characteristic and exhibit tightly packed well-defined boundaries. The 50 and 80% OPP films develop particles of similar size and shape as shown in Figs. 5.18b and 5.18c, the irregularly shaped lamellar surfaces that develop at 20% OPP are no longer present. Instead, grains are planarized and polygonal, and they possess a high aspect ratio (Figs. 5.18b and 5.18c) particle with the overall morphology having much less variation.

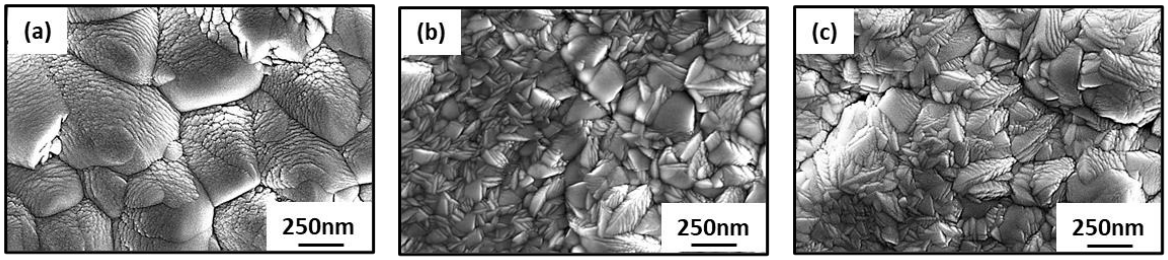

Figure 5.18. SEM micrographs PdO films deposited on 316 SS substrates and synthesized at 5mTorr WP and (a) 20 (b) 50 (c) 80% OPPs.

As WP was increased the surface variation of coatings increased and films developed microstructures defined by large pyramidally shaped particles with rough surfaces consisting of well-defined elongated grains as shown in the micrograph in Fig. 5.19 for PdO films synthesized at 20% OPP and 30 mTorr WP.

Apart from the films deposited at 20% OPP, the surface roughness increased with increasing WP and decreased with increasing OPP as shown in Fig. 5.20. The particularly high surface roughness measured in films synthesized at 20% OPP and 5 mTorr WP is attributed to the large radial grains. Similar to the IrO_x films, the substructure of PdO films grows to become more columnar and porous as WP is increased as shown in the cross-sectional micrograph in Fig. 5.21 for PdO films deposited 20% OPP and 30 mTorr WP.

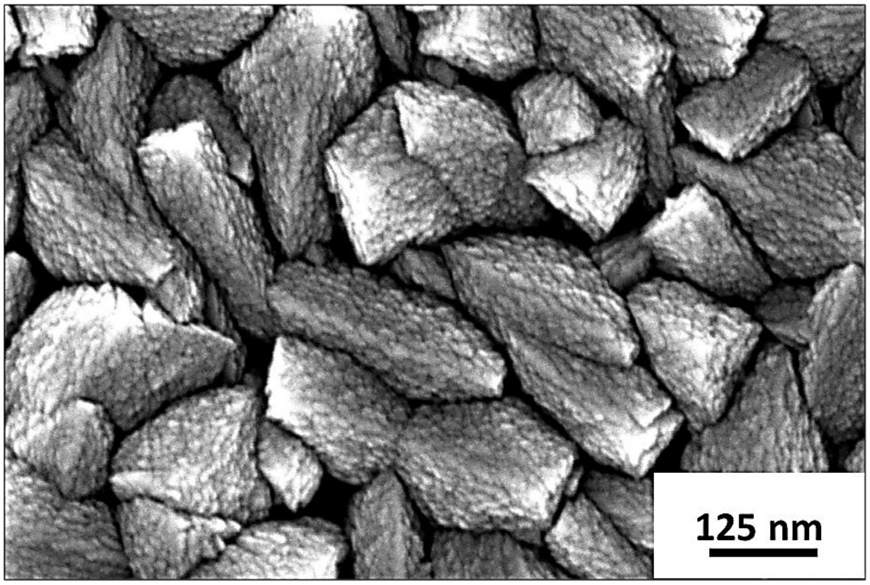

Figure 5.19. SEM micrographs of reactively sputtered PdO films deposited on 316 SS substrates and synthesized at 30 mTorr WP and 20% OPP.

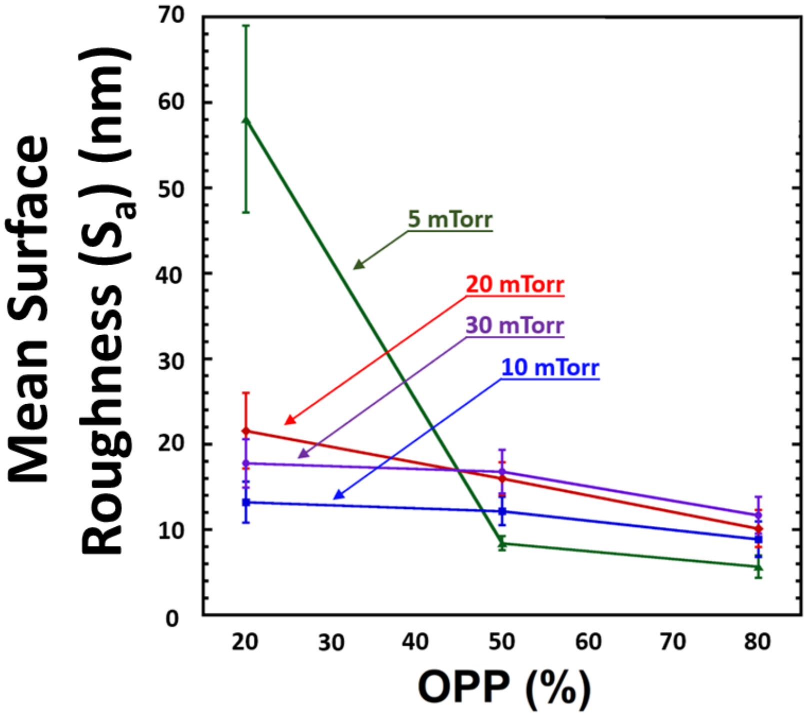

Figure 5.20. Mean surface area (S_a) roughness of PdO films deposited on 316 SS substrates.

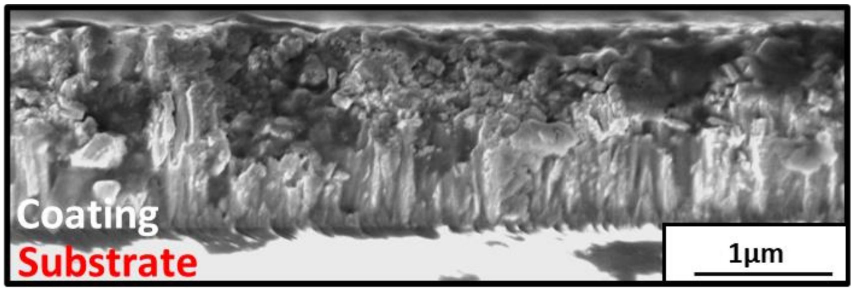

Figure 5.21. SEM micrograph cross section of PdO films deposited on Al_2O_3 substrates synthesized at 30mTorr WP and 20% OPP.

XRD analysis reveals that the PdO films synthesized at 20% OPP are polycrystalline with a palladinite crystal structure as shown in Fig. 5.22a. Films show apparent texturing in the (110) orientation with increased WP. Diffraction patterns for the PdO films synthesized at 20% OPP (shown in Fig. 5.22a) and 5 and 10 mTorr feature a broad metallic (110) cubic Pd peak around 39.6°. The presence of this peak suggests that under these lower pressure synthesis conditions, PdO films are only partially oxidized as suggested by Meyer and Muller-Buschbaum (169). The growth of the large irregularly shaped lamellar grains at 5 mTorr and 20% OPP (Fig. 5.18a) PdO films likely develop as a result of this apparent partial oxidation of Pd as indicated by the EDS results shown in Fig. 5.23. The presence of the metallic peak disappears at the higher two OPPs. PdO oxide films synthesized at 50 and 80% OPP grew preferentially in the (011) orientation (similar to the higher WP, 20% OPP films) as shown in Fig. 5.22b-c. Of the films deposited at the higher OPPs, the 5 mTorr WP films possessed the weakest apparent (011) texturing.

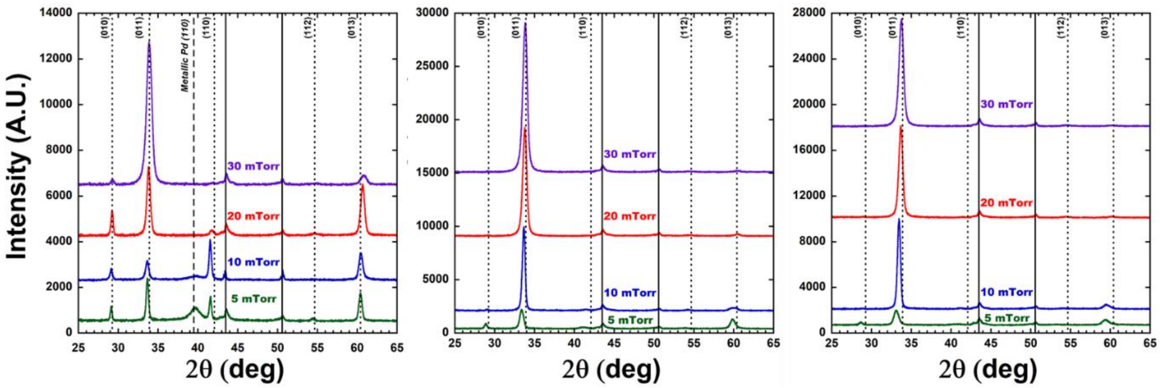

Figure 5.22. X Ray diffraction patterns of reactively sputtered PdO films (scaled for better comparison of working pressure) synthesized at (a) 20% OPP (b) 50% OPP (c) 80% OPP. The dotted lines and dashed lines, represent the reference angles for tetragonal PdO (170) and cubic metallic Pd (171) respectively. Solid lines denote substrate diffraction peaks.

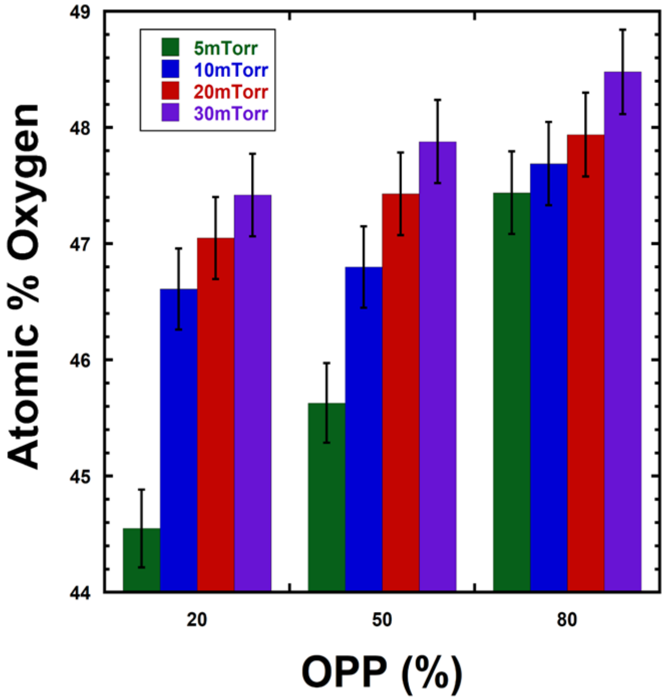

Figure 5.23. EDS results displaying the dependence of OPP and WP on the amount of dissolved oxygen in PdO films.

PdO is comparatively crystalline compared to the other three single metal oxide systems for depositions performed at ambient temperatures. Through monitoring the (011) peak additional structural characteristics and changes can be inferred resulting from deposition conditions and low temperature annealing of films. The conclusions identified from these changes are assumed to be generally applicable to the other systems due to the similar synthesis conditions across the single, binary, and ternary metal oxides investigated in this thesis.

As shown in Fig. 5.22a-c, the diffraction peaks shift to lower angles with decreased WP and increased OPP. These shifts are attributed to an expansion in the lattice constant and are depicted by the changes in the (011) d-spacing shown in Fig.

5.24a. The displacement of the (011) lattice constant from its thermodynamic equilibrium position for the stoichiometric phase (170) is substantial. The (011) lattice expansion increased in films deposited at lower WPs and higher OPPs as shown in Fig. 5.24b. As expected, the films synthesized at 5 mTorr WP and 80% OPP possessed the largest (011) lattice constant expansion of approximately 2.7%.

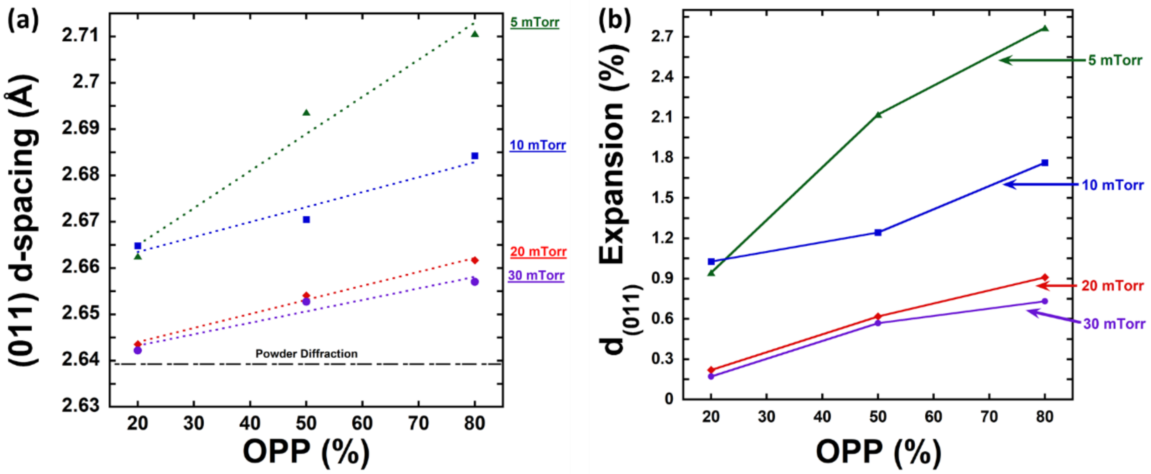

Figure 5.24. (a) (011) Lattice constant expansion for PdO oxide thin films; the horizontal dashed line represents the reference lattice constant for the (011) tetragonal PdO orientation. (b) % expansion of the (011) d-spacing.

To better understand the nature and origin of the morphological, surface texture, structural, compositional, and subsequent electrochemical changes observed, SIMTRA (172) a Monte-Carlo method simulation was used to model the λ_{mfp} and energies of incident sputtered atoms on the substrate. The incident angle of ions on the target was set to 0° (with respect to the surface normal of the target) and the ion energies of 475, 545, and 585 V for 20, 50, and 80% OPP, respectively, were used. The ion energies relate to the average discharge voltages (V_d) which were observed to be stable across the range of WPs tested. The vapor transport of sputtered particles to the substrate was simulated with a Coulomb interaction potential with Moliere screening with background temperature of 300K. It should be noted that, while the incident energies and λ_{mfp} are believed to be generally accurate in the their trends (173), this model does not account for the occurrence or energies of negative oxygen ions (NOIs) or reflected neutral atoms that form in the plasma. These particles have been shown to have incident energies up to several hundred eVs (138,142) at comparable plasma temperatures and can modify the structure of growing films(7). Furthermore, this model does not account for cluster formation of sputtered particles during vapor transport to the substrate.

The simulated λ_{mfp} (Fig. 5.25a) is shown to decrease rapidly as the working pressure is increased. However, there is little deviation observed in the λ_{mfp} based on the OPP. This small change is likely a result of the similar interaction radii of the background gas atoms. As a result, the incident energy of sputtered Pd does not vary significantly with the OPP, but the flux of material will be lower at higher OPPs due to the reduction in sputtering yield resulting from the mass difference between the O^+ ions and target atoms and the lower amount of Ar^+ ions incident on the target during sputtering. The incident energy is considerably higher at lower WPs as shown in Fig. 5.25b. This is not surprising, since the λ_{mfp}, incident energy, and WP are intimately connected variables during particle vapor transport to the substrate. To state it succinctly at higher WPs particles will collide more during vapor transport as indicated by the shorter λ_{mfp}. As a consequence, the incident particle energies on the substrate will decrease in accordingly.

Structurally, the increase in porosity from deposition at higher WPs can be easily explained by the reduction in incident particle energies (resulting from thermalization during vapor transport) causing particles to “stick” where they land on the substrate akin to the Volmer-Weber growth mode (Fig. 3.10a). As a result of this lack of adatom mobility, films will be more columnar and less dense. In contrast, films sputtered under lower WP conditions are denser due to higher incident particle energies (ballistic and mobility driven densification). This is qualitatively observed in the cross-sectional micrograph for the PdO films synthesized at 5 mTorr and 80% OPP shown in Fig. 5.26. Additionally, due to higher incident energies of Pd and reflected Ar neutral atoms under lower WP and lower OPP sputtering conditions, leads to the occurrence of preferential resputter of weakly adsorbed adatoms and lighter admolecules such as O_2. This helps provides a partial explanation of why the oxygen content in the 5 mTorr films sputtered at 20 and 50% OPP is considerably lower than that of their higher WP counterparts.

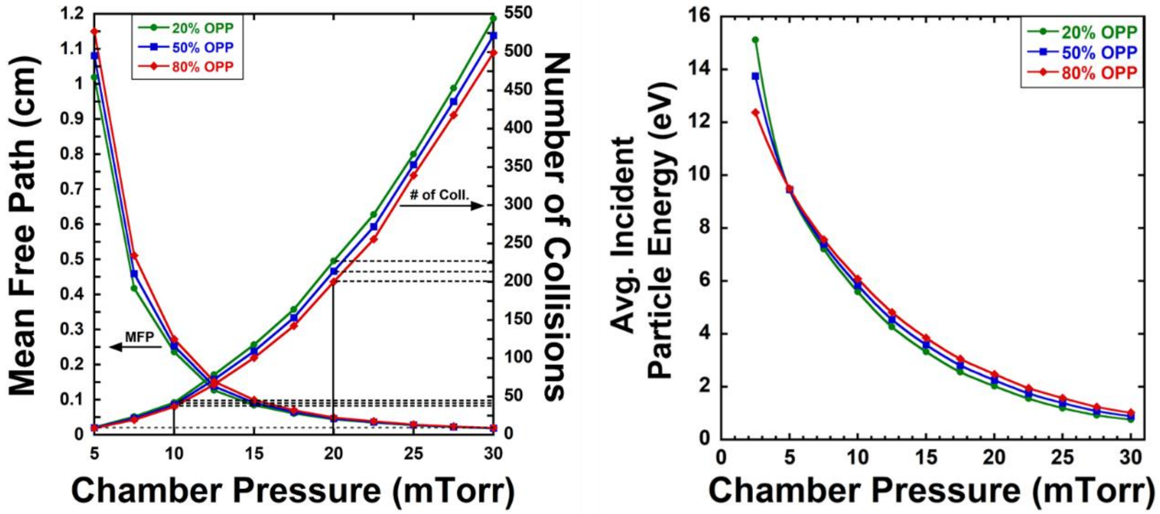

Figure 5.25. (a) Mean-free path and number of collisions from 5 to 30 mTorr WP for sputtered Pd atoms at sputtered at 20, 50, and 80% OPP as simulated by the Monte-Carlo method; the solid black lines correspond to sputtering pressures used; the dashed lines correspond to the respective number of collisions. (b) Simulated change in average arrival energy of Pd atoms at normal incidence on a substrate, 10 cm distance from cathode.

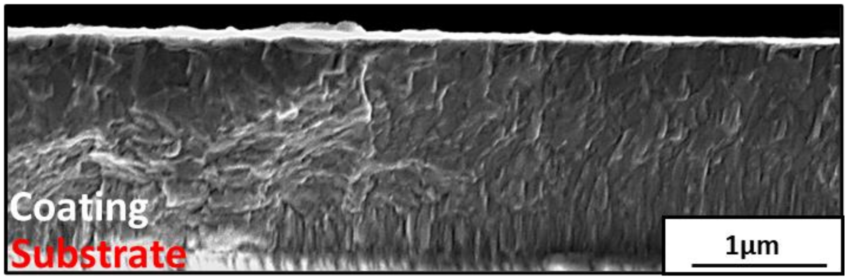

Figure 5.26. SEM micrographs cross sections of reactively sputtered PdO films deposited on Al_2O_3 substrates synthesized at 80% OPP and 5 mTorr WP.

An underdetermined feature of sputtering with reactive gas at high partial pressures is the occurrence of ion bombardment from NOIs generated in the plasma (as described in Section 3.2.2). For this thesis, extrinsic stress-inducing factors such as temperature are assumed to be negligible as films are sputtered at ambient temperatures and at low power densities. It is therefore assumed that the impingement of these NOIs on the growing film is the underlying mechanism behind the increasing amounts of strain that develop in films synthesized at higher OPPs and lower WPs (138,174,175). These energetic particles have been reported to increase compressive stress in films from trapping and interstitial implantation, and induce planarization (7,176,177). The latter effect gives some explanation to the planarized surfaces at lower WPs and high OPPs and the decreases in surface roughness with increasing OPP across all WPs. High energy ions are also known to cause defects in the crystal lattice and microdamage to the crystal structure through dislodging of atoms from equilibrium (which can cascade into adjacent structures) and interstitial implantation. As a result, films will become more amorphous, more dense, and experience a greater amount of strain (7,139,175,178,179).

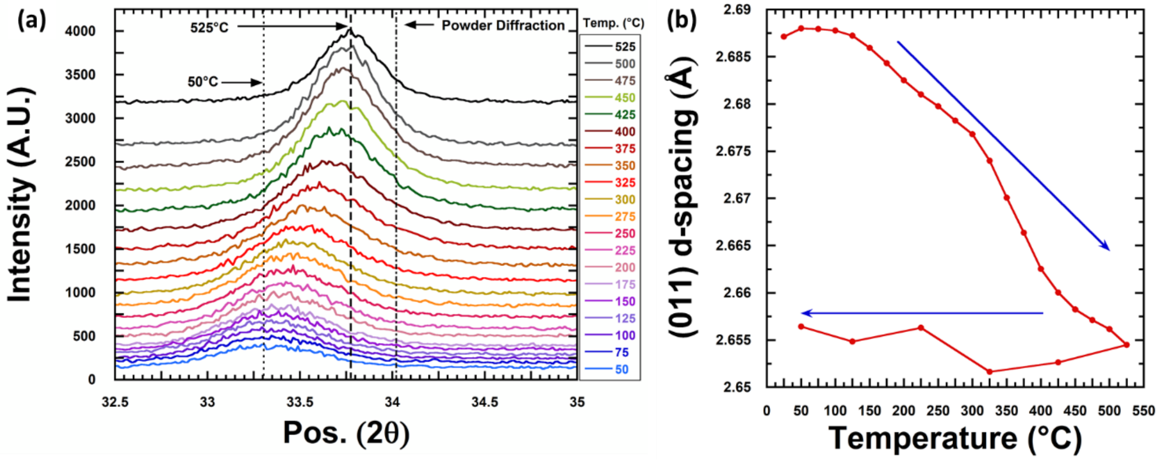

Figure 5.27. (a) Shift in the (011) diffraction peak through annealing of PdO deposited on Al$_2$O$_3$ and synthesized at 20% OPP and 5 mTorr WP. The annealing temperature range was 50° to 525°.(b) d-spacing of the (011) crystallite plane as a function of annealing temperature (blue arrows indicate cycling direction).

To better study these apparent NOI defect driven effects low temperature annealing of the 5 mTorr and 80% OPP PdO films was performed as outlined in Section 4.2.4.1. The shift in the (011) diffraction peak as a function of temperature is shown in Fig. 27a. Increased temperature is shown to result in a shift towards the powder diffraction reference angle. Notably, the EDS was performed on the as-deposited and post-annealed films. The results show only a slight decrease in oxygen content after annealing to 400°C as shown in Table 5.6. When annealed to 525°C the oxygen content in the films was reduced to 0% (not shown). This suggests between 400-525°C the PdO films begin to disassociate. This is evidenced by comparing the as-deposited and post-anneal diffraction patterns shown in Fig. 5.28. The presence of the (111) metallic Pd peak is not observed for the as-deposited pattern. On the other hand, for the post-annealed film, both the PdO (011) and the metallic Pd (111) are present.

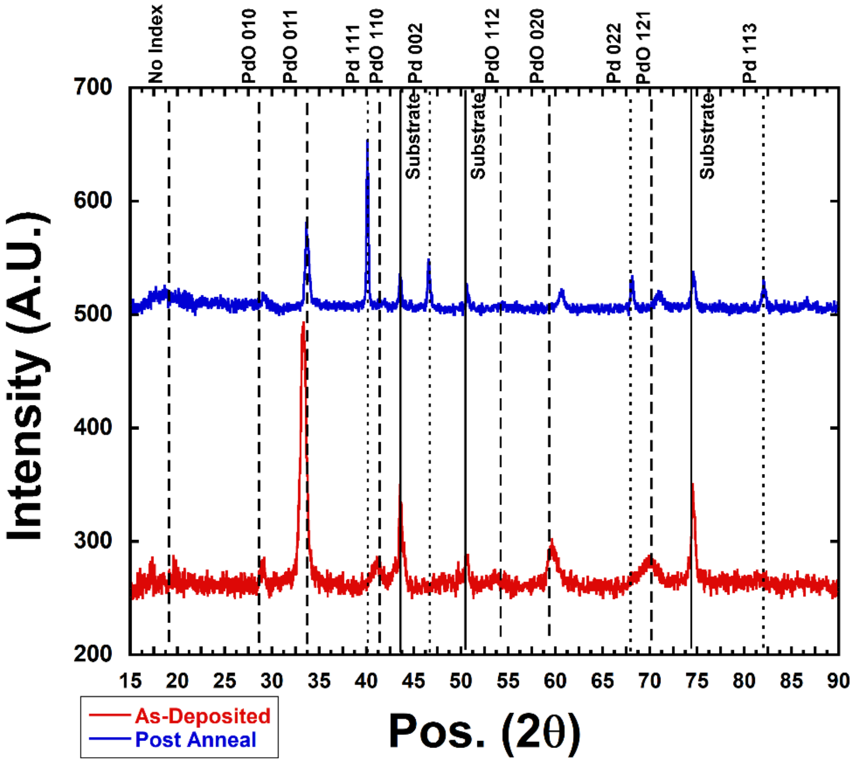

Figure 5.28. XRD patterns of as-deposited and post-anneal (525°C) PdO films deposited on 316 SS substrates. Dashed lines represent the reference peak locations for PdO. Dotted lines represent the reference peak locations for cubic Pd metal. The solid lines represent the substrate diffraction angles.

The (011) d-spacing as a function of annealing temperature is shown in Fig. 27b. The lattice constant tended towards the reference value as the annealing temperature increased. This is expected behavior because the additional energy provided to the interstitial and displaced atoms through thermal annealing allows for migration to equilibrium positions resulting in structural relaxation and crystallization. As suggested by Scherrer's equation (180), the broadening of diffraction peaks are associated with microstrain and smaller crystallite sizes. On the other hand, crystallization and annihilation of defects would result in a narrowing of diffraction peaks. In additional, an increase in intensity is also associated with an increase in crystal ordering. These characteristics can be inferred by the change in the FWHM and the integrated area of the (011) peak during thermal annealing shown in Fig. 5.29a-b. The FWHM is observed to decrease with increasing temperature as shown in Fig. 5.29a, suggesting crystallization and defect annihilation has occurred. In further support, the integrated area of the (011) peak is observed to increase as annealing temperature is increased as shown in Fig. 5.29b. Some additional contributions to the decrease of the FWHM are texturing and oxygenation of Pd. However, the contribution due to oxygenation of Pd is assumed to be minimal because annealing was performed in an Ar-rich atmosphere. At 450°C the integrated area is observed to start to decrease with increasing temperature. This may indicate that at 450°C dissociation begins to occur.

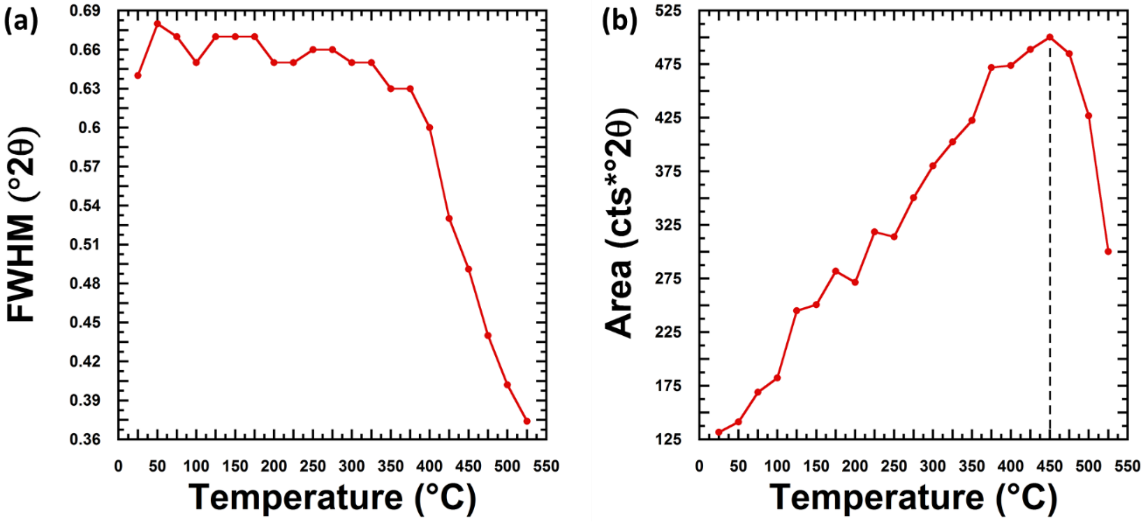

Figure 5.29. FHWM of the (011) diffraction peak through annealing of PdO deposited on Al_2O_3 and synthesized at 80% OPP and 5 mTorr WP. Vertical dashed lines depict the apparent temperature in which films begin to disassociate.

Table 5.6

Oxygen content (at. %) Before and After Annealing at 400°C [a]

Element	Pd	O
As-Deposited	49.98	50.02
Post-Anneal	48.11	51.89

[a] *Film Synthesized at 30mTorr WP and 20% OPP*

The trend in electrochemical performance of PdO films are similar to that of IrO_x, albeit with lower electrochemical performance. As shown in Fig. 5.30a-b and Table 5.7, the CSC_C increased, and impedance decreased with increasing WP, while at each WP, the CSC_C decreased with increasing OPP. The improvement of the electrochemical performance of films is attributed to the apparent increase in porosity and thereby the ESA with increasing WP. Additionally, the full oxidation of Pd may also be a contributing factor. Interestingly, the partial oxidation of PdO films synthesized at 20% OPP and 5 and 10 mTorr WP is confirmed by CV curves shown in Fig. 5.31. The voltammograms of these films possess a characteristic reduction peak around -200 mV relating to the Pd^{2+} oxidation state. In further support, the CV curves for the partially oxidized films investigated in this thesis match those measured by Zhang *et al.*, (181) who investigated partially oxidized Pd films in PBS solutions. The redox reaction expected for PdO films is given by the following the reaction equation:

$$\mathrm{Pd^{2+}}:\ \mathrm{PdO_{(s)}} + \mathrm{H_2O_{(aq)}} + 2e^- \rightleftharpoons \mathrm{Pd_{(s)}} + 2(\mathrm{OH})^-_{(aq)} \qquad (25)$$

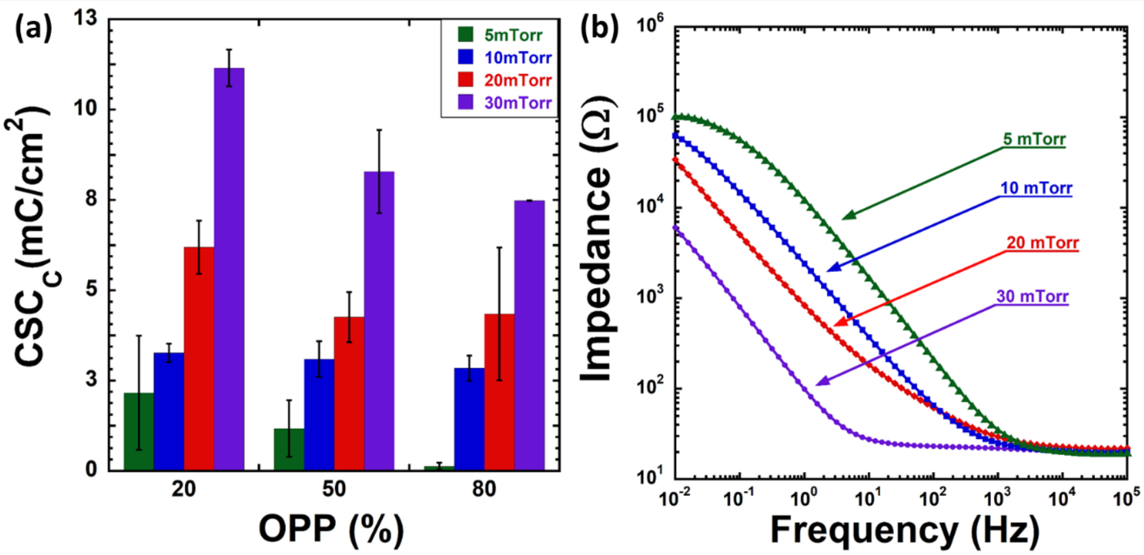

Figure 5.30. (a) Evolution of CSC_C as a function of OPP and WP in PdO films obtained from CV measurements (b) Electrochemical impedance Bode modulus plot of reactively sputtered PdO films deposited at 20% OPP.

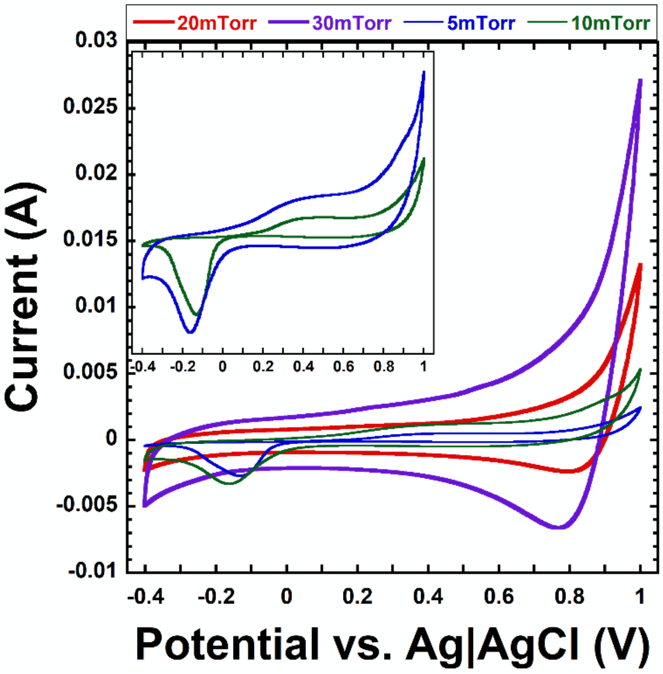

Figure 5.31. Typical cyclic voltammograms (20th cycle) PdO films deposited on 316 SS substrates deposited at 20% OPP and 5, 10, 20 and 30 mTorr WPs. Voltammogram inserts for lower WP films are rescaled for better comparison.

Table 5.7

Cathodic Charge Storage Capacity and Maximum Impedance of PdO[a]

Working Pressure (mTorr)	5	10	20	30
CSC_C (mC/cm^2)	0.24 ± 0.013	1.4 ± 0.82	15 ± 3.4	30 ± 0.72
Impedance (Ω)	104100	62986	34271	6072

[a] *Film Synthesized at 30mTorr WP and 20% OPP*

The Nyquist plot and ECM of PdO films synthesized at 20% OPP and 30 mTorr are presented in Fig. 5.32a, and the corresponding values for the ECM elements are provided in Table 5.8. The Nyquist impedance response suggests an increase in film porosity. The response is characteristic of finite space or bounded Warburg (W_T) behavior wherein at lower frequencies the impedance is determined by capacitive behavior relating to adsorption effects and to counter-ion confinement in pores. This is reflected in the phase angle response (Figs. 5.32b) that tend towards 90° with decreasing frequency. In addition, the ECM of the 30 mTorr films requires the use of a W_T element to describe the impedance responses. This is consistent with the SEM cross-section observations and lends physical significance to the models.

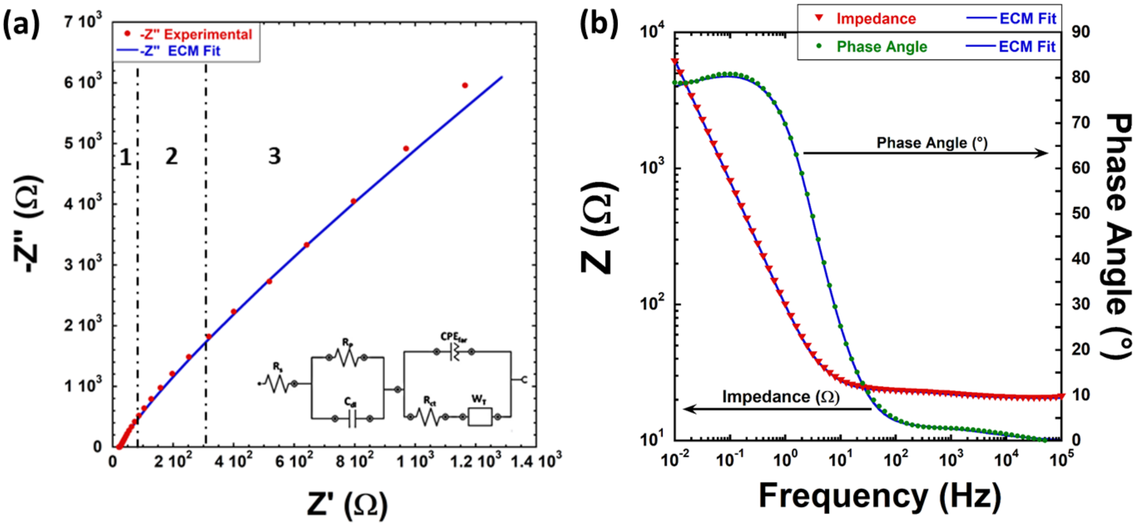

Figure 5.32. (a) Nyquist impedance plots and equivalent circuit models (ECM) of PdO synthesized at 20% OPP and 30 mTorr the regions labeled 1, 2, and 3 represent the approximate regions corresponding to (1) internal resistance which includes the solution, charge transfer, and double layer resistance (2) bounded diffusion region (3) bounded diffusion and pseudocapacitive region. (b) Bode modulus impedance and phase angle responses of PdO synthesized at 20% OPP and 30 mTorr.

Table 5.8

ECM Elements for PdO Parameters, and Values[a]

Element	R_s	R_p	C_{dl}	R_{ct}	CPE_{far}		W_T	
Parameter	R(Ω)	R(Ω)	C(F)	R(Ω)	$Y_0(S{\bullet}s^N)$	N	$Y_0(S{\bullet}s^{1/2})$	$B(s^{1/2})$
Value[b]	21	3.6	0.00579	2.4	5.76E-04	0.724	0.0204	0.0679

[a] *Films synthesized at 20% OPP and 30mTorr WP*

[b] *$\chi^2 = 0.061$*

5.2.2 Summary and Conclusions

PdO films develop large pyramidal grains that possess a high degree of crystallinity for coatings synthesized at ambient temperatures. The apparent increase in film porosity and columnar growth with increasing WP are similar to previous observations in IrO_x. This is not surprising as the mechanics of sputtering related to vapor transport do not change considerably across the different metal oxide systems. The sputtering mechanics were further explored for PdO films through the use of Monte-Carlo method simulations. The simulations suggest that the morphological changes such as columnar growth and porosity are strongly influenced by the effects of WP on the λ_{mfp} and incident energies of sputtered particles. Less general characteristics such as grain size, shape, and topography are attributed to the material properties of the target. The simulations do not account for sputter of oxide from the target, cluster formation during vapor transport, energetic neutral atoms, or ions formed in the plasma, all of which can have profound effects on the morphology, microstructure, composition, and crystal structure of films. The effect of lattice expansion and defects on the electrochemical properties of films remains largely ambiguous. However, it is worth noting that films which possess d-spacings closer to the reference values *i.e.*, those deposited at 20% OPP are the highest performing electrochemically. This suggests that interstitials and defects may weakly influence the electrochemical properties of films.

The determining factor in electrochemical performance of the PdO films is believed to be the porosity as is indicated by the ECM and EIS analyses and SEM cross-sections. The CV curves also suggest that activated oxidation states influence the electrochemical performance of films. The highest CSC_C and lowest impedance films were those deposited at 20% OPP and 30 mTorr WP. These observations are consistent with the conclusions from the IrO_x investigation.

5.3 Rhodium Oxide Thin Films

In the following section the synthesis and characterization of Rh_xO_y thin films deposited under various OPP and WP conditions are discussed. The results presented in this section are components of the unpublished manuscript. The synthesis parameters for Rh_xO_y are outlined in sections 3.4.1.

5.3.1 Results and Discussion

The surface microstructures for Rh_xO_y films synthesized at 20% OPP are shown in Fig. 5.33 a-d. The microstructure is also representative of the changes observed in the films grown at 50 and 80% OPPs (not shown). At 5 mTorr, the Rh_xO_y films grow nano-spherical grains that were tightly packed but well defined. As the WP was increased the grain shape and size remain largely unchanged. However, grains begin to cluster in a similar fashion similar to the those of 20% OPP and 30mTorr WP IrO_x films (Fig. 5.8), albeit with much smaller voids between boundaries as shown in Fig. 5.32d. The changes observed in the surface microstructure are somewhat reflected in the mean surface roughness shown in Fig. 5.36a. Roughness increased with increasing WP for films deposited at 20% OPP. Interestingly, the S_a increased considerably in films deposited at 20 and 30 mTorr WP.

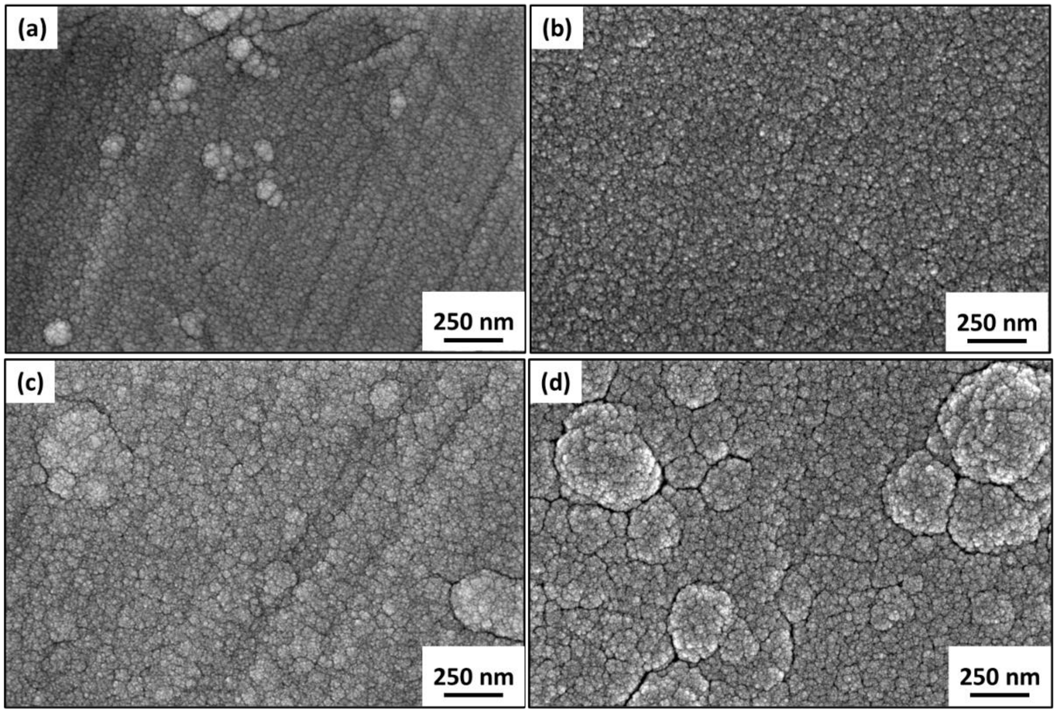

Figure 5.33. SEM micrographs of reactively sputtered Rh_xO_y films deposited on 316 SS substrates and synthesized at 20% OPP and (a) 5 (b) 10 (c) 20 and (d) 30 mTorr WPs.

The films developed an increasingly columnar substructure as WP was increased in Rh_xO_y similar to what was observed in the other single metal oxide systems as shown in Fig. 5.34, which depicts the cross-section of a Rh_xO_y film deposited at 30 mTorr WP and 20% OPP. However, unlike the other systems which become more fibrous at 30 mTorr, the columnar substructure for Rh_xO_y is mainly intact at 30 mTorr. It is likely that the transition to more porous and fibrous sub-structures will develop at higher WP.

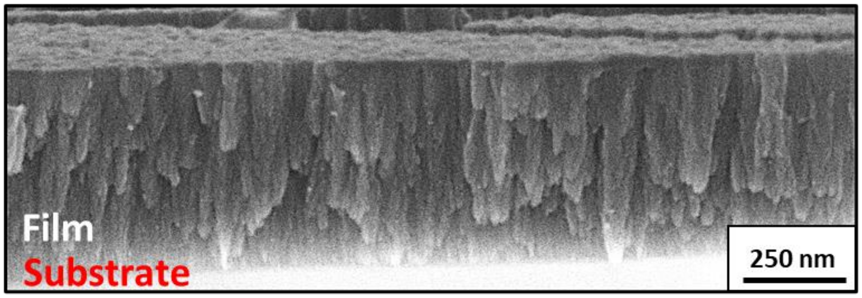

Figure 5.34. Cross-sectional SEM micrographs of Rh_xO_y, films deposited on Al_2O_3 substrates synthesized at 30 mTorr WP and 20% OPP.

Indexing of the XRD patterns of Rh_xO_y films indicate that films develop an apparent corundum crystal structure as shown in Fig. 5.35a-c. The expected stoichiometry of these films is Rh_2O_3; however, coatings were measured by EDS to be near or over-stochiometric as shown in Fig. 5.36b. Overall, Rh_xO_y films are nearly amorphous, with only a broad reflection centered on the primary (211) peak (around 34.5°) observed in diffraction patterns for all WPs in Rh_xO_y films deposited at 20% OPP as shown in Fig 5.35a. This broad peak is likely a result of a combination of small grain size, inhomogeneous strain, and the presence of metastable phases. Films become more amorphous with increased OPP as indicated by the (211) peak gradually broadening as shown in Figs. 5.35b and 5.35c for films deposited at 50 and 80% OPP, respectively. Additionally at 50 and 80% OPP films are shown to become more disordered with increasing WP. These changes are generally in line with the previously discussed sputtering dynamics and kinetics.

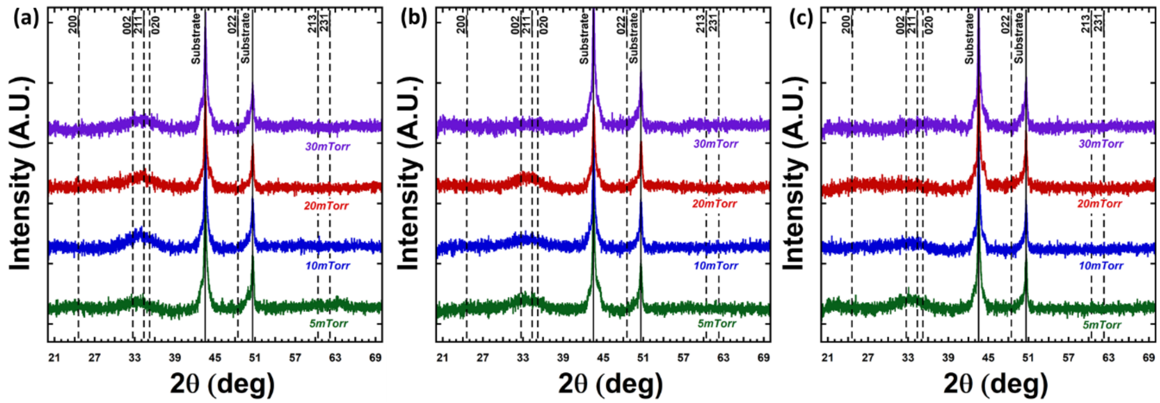

Figure 5.35. X-ray diffraction patterns of Rh_xO_y, films deposited on 316 SS substrates synthesized at (a) 20 (b) 50 (c) 80% OPP. Dashed lines represent reference angles for Rh_xO_y (182); solid lines denote substrate diffraction peaks.

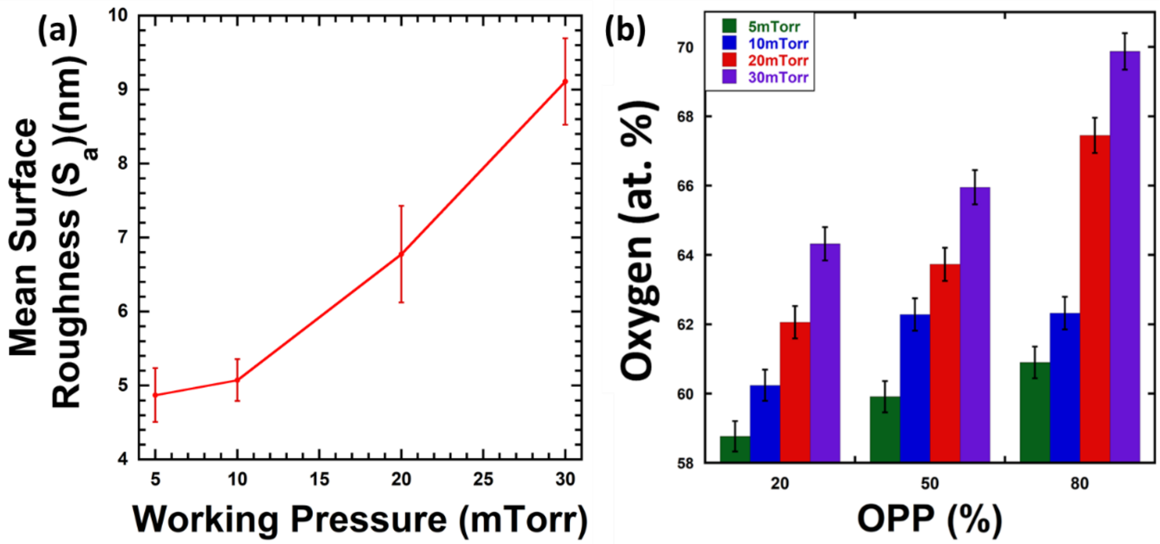

Figure 5.36. (a) Mean surface area roughness (S_a) of Rh_xO_y films synthesized at 20% OPP and deposited on 316 SS substrates. (b) Oxygen content (at. %) of Rh_xO_y films as measured by EDS as a function of sputter deposition OPP and WP.

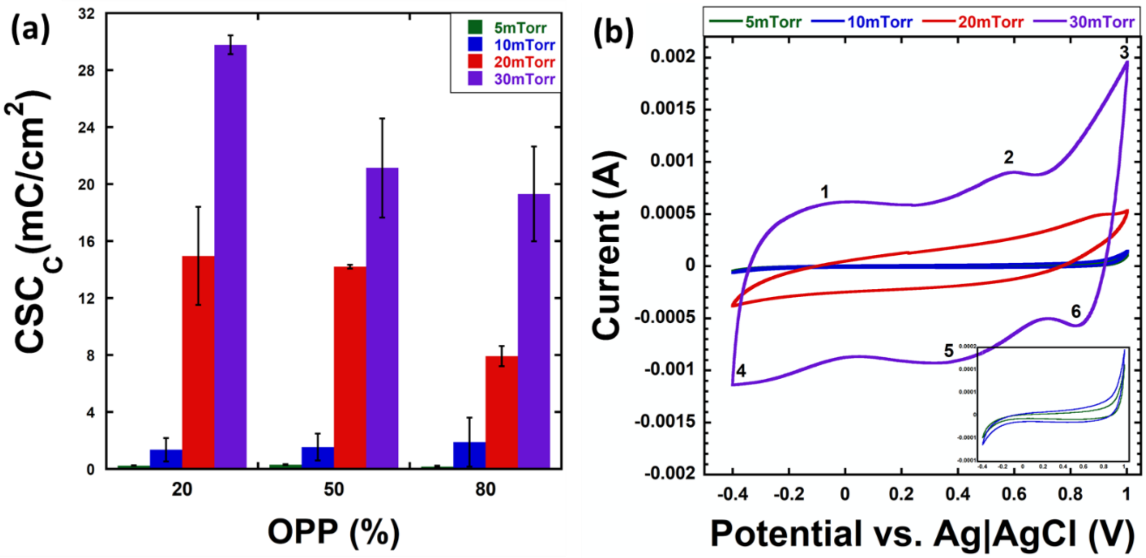

Figure 5.37. (a) Evolution of CSC$_C$ with increasing WP and OPP for Rh$_x$O$_y$ films deposited on 316 SS substrates obtained from CV measurements. (b) Typical cyclic voltammograms (20th cycle) Rh$_x$O$_y$ films deposited on 316 SS substrates deposited at 20% OPP and 5, 10, 20 and 30 mTorr WPs; voltammograms and inserts for lower pressure films are rescaled for better comparison; the numbers on the 30 mTorr profile represent the peak potentials.

The electrochemical properties of Rh$_x$O$_y$ films mirror those of the other single metal oxide systems, wherein improvements in electrochemical performance occur at higher synthesis WPs but a reduction in performance occur in response to higher OPPs. The results for the CSC$_C$ and impedance are shown in Figs. 5.37a and 5.38, respectively. The highest electrochemically performing films are those deposited at 30 mTorr WP and 20%OPP.

Voltammograms for films deposited at 5-20 mTorr and 20% OPP shown in Figs. 5.37b display no redox peak currents indicative of Rh(II)/Rh(III). At 30 mTorr, the Rh$_x$O$_y$ system begins to exhibit pseudocapacitive behavior as evidenced by the voltammogram shown in Fig. 5.37b, wherein peaks 2 and 5 are believed to be associated with the

Rh(II)/Rh(III) redox couple. Redox equations for typical Rh_xO_y oxidation states are presented in the following redox equations:

$$Rh^{3+} : \; Rh_2O_{3(s)} + H_2O_{(aq)} + 2e^- \rightleftharpoons 2RhO_{(s)} + 2(OH)^-_{(aq)} \qquad (26a)$$

$$Rh^{4+} : \; 2RhO_{2(s)} + H_2O_{(aq)} + 2e^- \rightleftharpoons Rh_2O_{3(s)} + 2(OH)^-_{(aq)} \qquad (26b)$$

while peaks 3 and 6, and 1 and 4 are related to the reduction and oxidation of water (183). The ECM for Rh_xO_y films deposited at 30 mTorr is identical to the IrO_x ECM synthesized at the same conditions (Fig. 5.16). The reasoning for the use of this model for the Rh_xO_y system is similar to justification behind its use for the IrO_x system. The appropriate fitting parameters are provided in Table. 5.9.

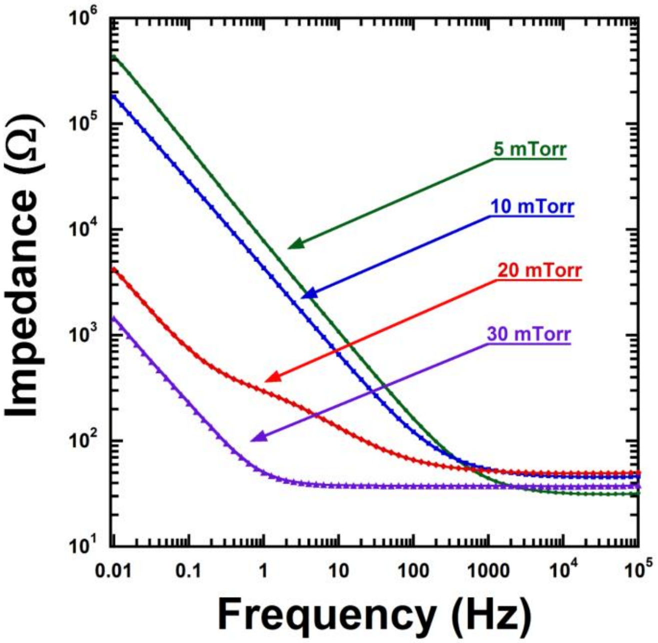

Figure 5.38. Electrochemical impedance Bode modulus plot of reactively sputtered Rh_xO_y films deposited on 316 SS substrates and synthesized at 20% OPP.

Table 5.9

ECM Elements for Rh_xO_y Parameters, and Values[a]

Element	R_s	R_p	W_T		C_{dl}	R_{ct}	C_{far}	CPE_{ads}	
Parameter	R(Ω)	R(Ω)	$Y_0(S \cdot s^{1/2})$	$B(s^{1/2})$	C(F)	R(Ω)	C(F)	$Y_0(S \cdot s^{1/2})$	N
Value[b]	19	1.5	0.062	0.81	1.4E-05	134	0.0047	0.0055	0.76

[a] *Films synthesized at 20% OPP and 30mTorr WP*

[b] *$\chi^2 = 0.005$*

5.3.2 Summary and Conclusions

Rh_xO_y films have growth characteristics similar to those of the previously discussed single metal oxide systems. Rh_xO_y films become increasingly porous with increasing WP, and as a result the ESA is increased thus improving the charge exchange characteristics of films. The common +3 oxidation state is assumed to be the primary redox couple for charge exchange based on stoichiometry and the generally lower CSC_C when compared to the IrO_x films but higher CSC_C than the PdO films (which have +4 and +2 common oxidation states, respectively). Importantly, the substructure of Rh_xO_y films remains columnar at 30 mTorr which hints that increasing the WP further will increase the electrochemical properties without immediately jeopardizing the mechanical properties of the films (too porous/low density) which could make it unsuitable for implantable neural interfaces. A table summarizing the maximum impedance and CSC_C values for films deposited at 20% OPP are shown in Table 5.10.

Table 5.10

Cathodic Charge Storage Capacity and Maximum Impedance of Rh_xO_y[a]

Working Pressure (mTorr)	5	10	20	30
CSC_C (mC/cm^2)	0.24 ± 0.013	1.4 ± 0.82	15 ± 3.4	30 ± 0.72
Impedance (Ω)	434330	180000	4178	1447

[a] *Film Synthesized at 30mTorr WP and 20% OPP*

5.4 Ruthenium Oxide Thin Films

In the following section the synthesis and characterization of RuO_x thin films deposited under various OPP and WP conditions are discussed. The results presented in this section are components of published results. The synthesis parameters for RuO_x are outlined in sections 3.4.1.

5.4.1 Results and Discussion

The microstructure of RuO_x films deposited at 20% OPP are shown in Fig 5.39a-d. The surface microstructure is shown to be similar to that of the Rh_xO_y films. The grains of RuO_x films synthesized at 5 mTorr (Fig. 5.39a) are nanospherical and tightly packed. As WP is increased the spherical grains begin to cluster into spherical particles as shown in Figs. 5.39b and 5.39c. The surface microstructure of RuO_x deposited at 20% OPP and 30mTorr WP is shown in Fig. 5.39d. Films develop nano-spherical grains which cluster into polygonal-like shapes. The substructural growth observed in the RuO_x films deposited at 20% OPP mirrors that of the previously investigated single metal oxide systems as shown in Fig. 5.40. which depicts the substructure of RuO_x films deposited at

30 mTorr. Notably, the substructural growth is less columnar and more porous. This substructure resembles that of the IrO_x substructure more so than that of Rh_xO_y.

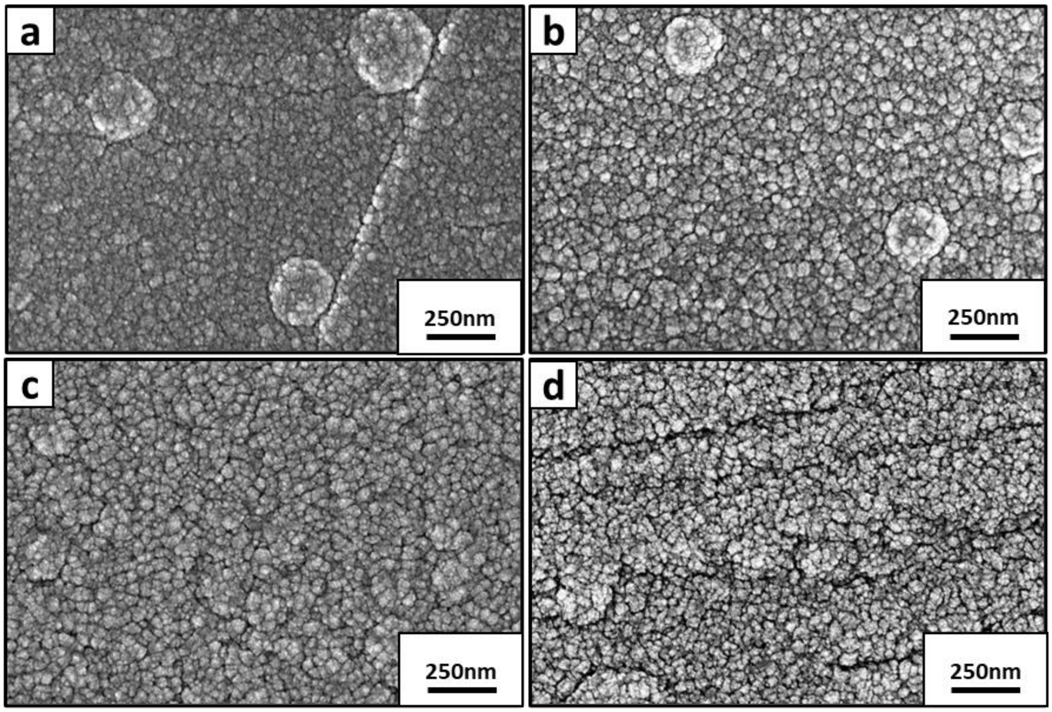

Figure 5.39. SEM micrographs of reactively sputtered RuO_x films deposited on 316 SS substrates and synthesized at 20% OPP and (a) 5, (b) 10, (c) 20, and (d) 30 mTorr WPs.

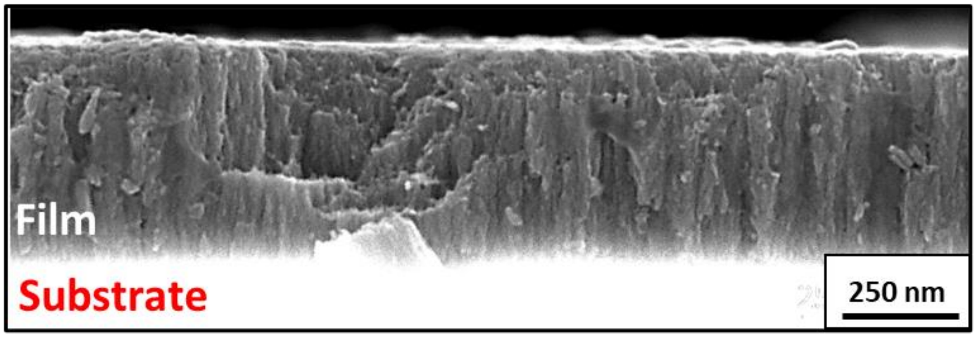

Figure 5.40. Cross-sectional SEM micrographs of RuO_x, films deposited on Al_2O_3 substrates and synthesized at 30 mTorr WP and 20% OPP.

The surface microstructure of the RuO_x films changes considerably at 20 and 30 mTorr WPs as OPP is increased (20 mTorr films not shown) as shown in Figs. 5.41. The surface microstructure of RuO_x deposited at 20% OPP and 30mTorr WP is shown in Fig. 5.39d. The films develop nano-spherical grains which cluster into polygonal-like shapes at low OPPs. When deposited at 50% OPP the RuO_x develop into planarized angular grains as shown in Fig. 5.41a. Close inspection of these surfaces reveals that the presence of nano-spherical grains, suggesting this transformation is a form of early-stage crystallization which is surprising due to the low ambient deposition temperatures. The films grown at 80% OPP reveal much of the same microstructure observed in the 50% OPP films as shown in Fig. 5.40b. However, the additional nano-spherical surface features on the grains are no longer present. Congruent with the other single metal oxides, the surface roughness is shown to increase with increasing WP for RuO_x films deposited at 20% OPP as shown in Fig. 5.42.

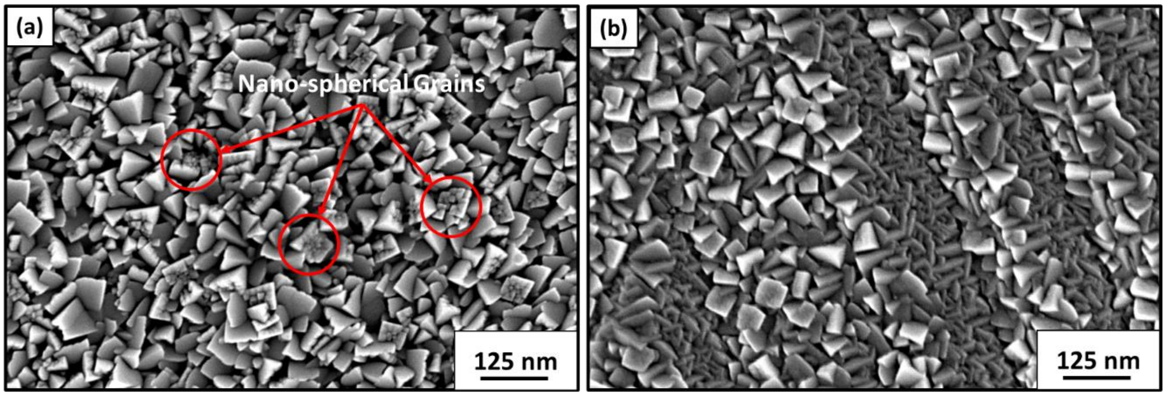

Figure 5.41. SEM micrographs of reactively sputtered RuO_x films deposited on 316 SS substrates and synthesized at 30 mTorr WP and at (a) 50 (b) and 80% OPPs.

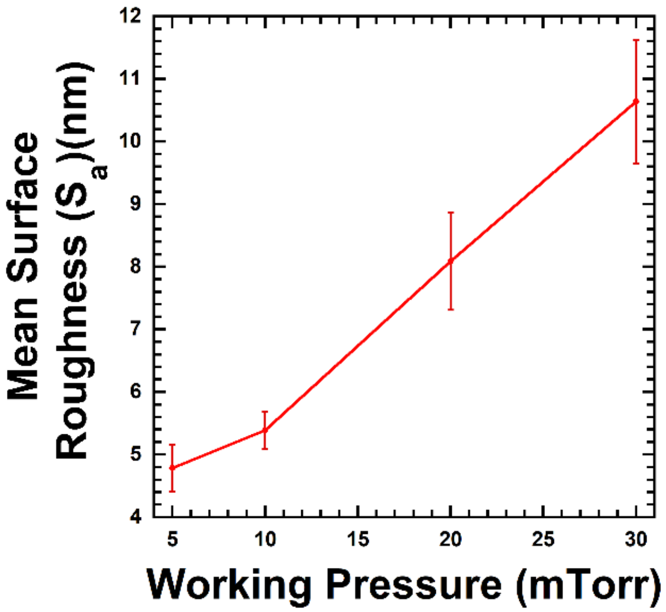

Figure 5.42. Mean surface area roughness (S_a) of RuO_x films synthesized at 20% OPP and deposited on 316 SS substrates.

XRD analysis of the RuO_x reveals films grow with a rutile crystal structure as shown in Fig. 5.43a-c, consistent with an expected stoichiometry of RuO_2. Films deposited at 20% OPP presented in Fig. 5.43a shows that at low WPs films are untextured and polycrystalline. As WP is increased RuO_x films show preferential growth in the (110) orientation with the (020) and (121) reflections broadening and decreasing in intensity (with the exception of the 10 mTorr sample). Surprisingly, films deposited at 50% OPP shown in Fig. 5.43b are the most crystalline of the three OPPs and show preferential growth in the (110) orientation. Additionally, the presence of the (011) reflection is present at 20 and 30 mTorr which coincides with the growth of the planarized polygonal grains. Films deposited at 80% OPP shown in Fig. 5.43c are less crystalline than their lower OPP counterparts. However, the presence of the (110) and the (011) orientations particularly at 20 and 30 mTorr OPP does suggest the (011) surface is related to the flat polygonal particle growth. Similar to what was found in IrO_x the presence of this surface may be related to increased surface energies such that the equilibrium (lowest stability ratio) phase cannot form. Notably, the RuO_x films that do not develop the planarized grains generally are measured as being close to or under-stoichiometric whereas those that do possess the polygonal planarized microstructure are shown to be largely over stoichiometric (Fig. 5.44). Based on the chemical composition, the planarized grains possess oxygen content which would indicate the growth of RuO_4. However, the presence of RuO_4 is highly unlikely, and it is more likely the excess oxygen is interstitially implanted and/or trapped. The morphology of the surfaces may be related to a surface reconstruction, or a more stable rutile surface as indicated by the presence of the (011) peak resulting from the O_2 adlayer. Details of these surface should be investigated further in future work.

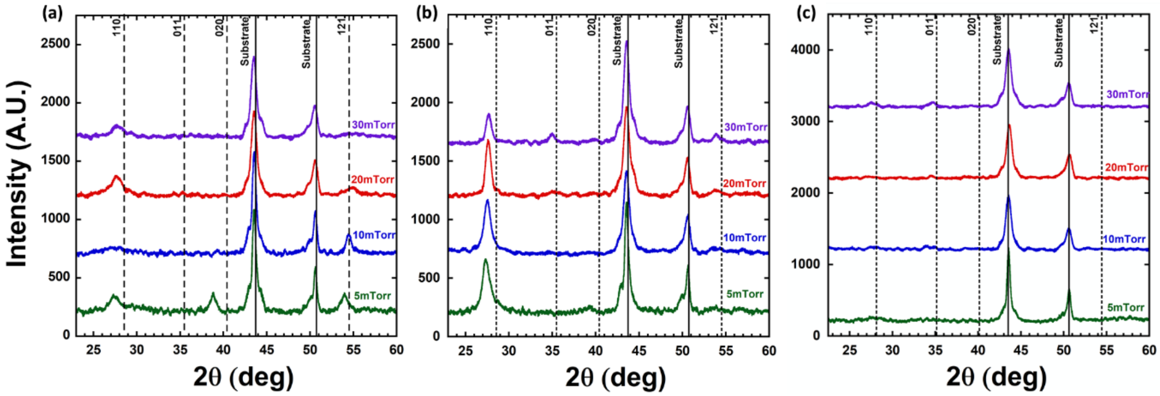

Figure 5.43. X-ray diffraction patterns of RuO_x, films deposited on 316 SS substrates synthesized at (a) 20 (b) 50 (c) 80% OPP; dashed lines represent reference angles for RuO_2; solid lines denote substrate diffraction peaks.

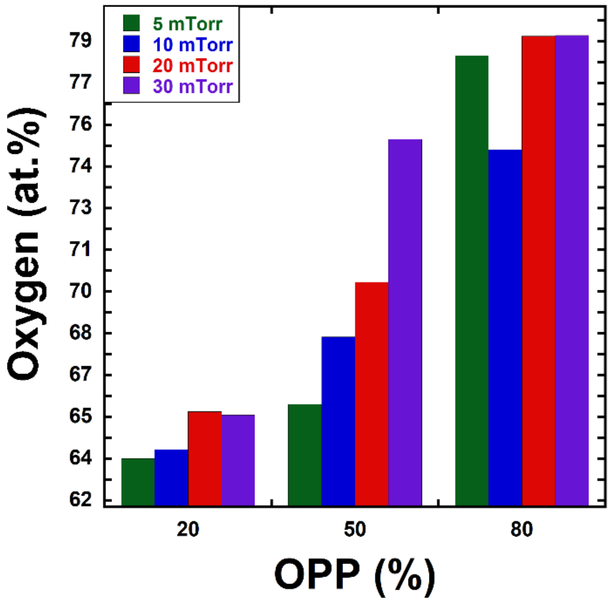

Figure 5.44. Oxygen content of RuO_x films deposited on 316 SS substrates as measured.

The CSC_C for RuO_x films is shown in Fig. 5.45a. RuO_x films deposited at 20% OPP show a similar electrochemical response to those observed in the other binary oxide systems wherein as WP is increased the CSC_C increases with similar explanation. The CSC_C of the 50 and 80% OPP films *i.e.*, those that develop the planarized polygonal grains, have low CSC_C. This is expected as the ESA of the films is severely diminished by this microstructure. The corresponding CV curves for films deposited at 20% OPP shown in Fig. 5.45b suggest that the activation of Ru(III)/Ru(IV) given by Eqn. 27, occurs at WPs as low as 10 mTorr as the 2/5 peak potentials (these are assumed to be indicative of the R(III)/Ru(IV) redox couple) are clearly visible on this curve.

$$Ru^{3+}: \; Ru_2O_{3(s)} + H_2O_{(aq)} + 2e^- \rightleftharpoons 2RuO_{(s)} + 2(OH)^-_{(aq)} \qquad (27a)$$

$$Ru^{4+}: \; 2RuO_{2(s)} + H_2O_{(aq)} + 2e^- \rightleftharpoons Ru_2O_{3(s)} + 2(OH)^-_{(aq)} \qquad (27b)$$

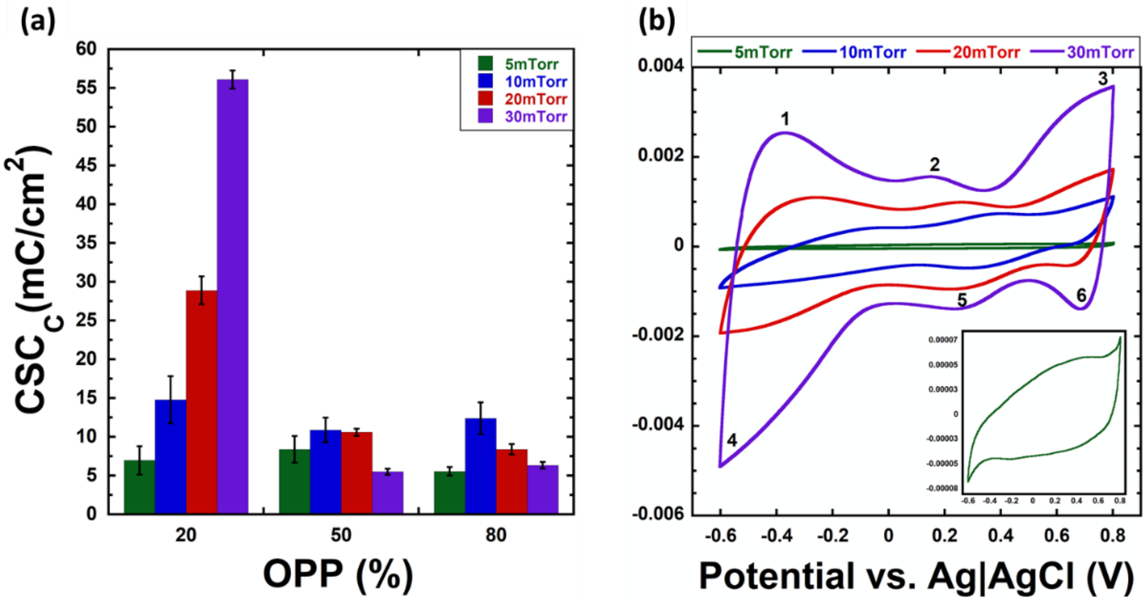

Figure 5.45. (a) Evolution of CSC_C with WP and OPP for RuOx films deposited on 316 SS substrates obtained from CV measurements. (b) Typical cyclic voltammograms (20th cycle) RuO_x films deposited on 316 SS substrates and synthesized at 20% OPP. Voltammograms and inserts for lower WP films are rescaled for better comparison; the numbers on the 30 mTorr profile represent the peak potentials.

To assess the substrate dependence on the electrochemical properties the total CSC was measured on as-deposited films grown on 316 SS and SiO_2/Si substrates, and the results are presented in Fig. 5.46. The 316 SS substrate does result in a higher CSC (from the as-rolled surface texture of the substrate) over the comparatively much less rough SiO_2/Si substrate. However, the difference in performance between films deposited on the different two substrates is roughly 10% (around a maximum 5mC/cm^2) and the trend of performance as a function of thickness is nearly identical. This demonstrates that the as-rolled stainless substrates are a suitable and effective test platform for investigating the electrochemical properties of these films.

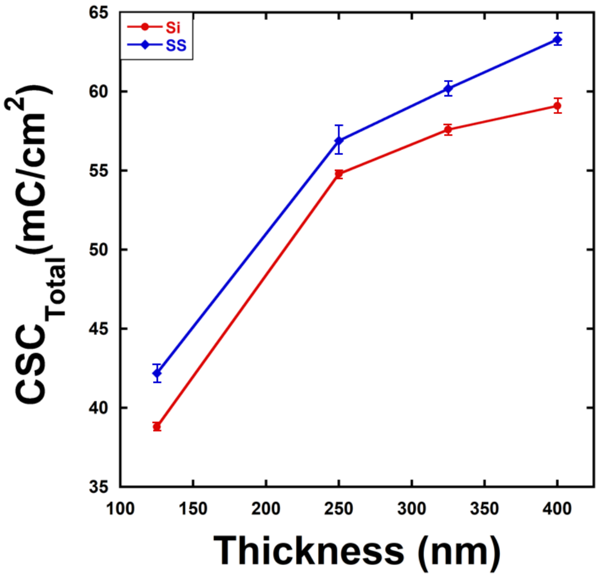

Figure 5.46. Total CSC of RuO_x films deposited on 316 SS and SiO_2/Si substrates as a function of thickness.

The EIS spectra for RuO_x films deposited at 20% OPP are shown in Fig. 5.47a-b. Similar to the other single metal oxide systems, the impedance decreases with increasing WP (Fig. 5.47a). As inferred from the CV curves, a change in the electrochemical response is observed when WP is increased to 10 mTorr (which is comparatively lower WP than the 20 mTorr in the other single metal oxide systems). This is confirmed in the phase angle response shown in Fig. 5.47b, which shows a large inflection in the phase angle at approximately 100 Hz. This is characteristic of a kinetically slow time constant indicative of mixed kinetic and diffusion-controlled response. In other words, the charge exchange or reaction rate is fast enough where there is depletion of the electroactive species at the electrode which promotes diffusion via a concentration gradient. However, it is much slower when compared to that of the films grown at the higher WPs. This is likely related to the activation of Ru(II)/R(III) and the Ru(III)/Ru(IV) oxidation states as well as increases in film porosity. Additionally, the ECM used to describe the EIS results from the 20% OPP and 30 mTorr WP IrO_x and Rh_xO_y films is translatable to the RuO_x films. The appropriate fitting parameters are shown in Table 5.11.

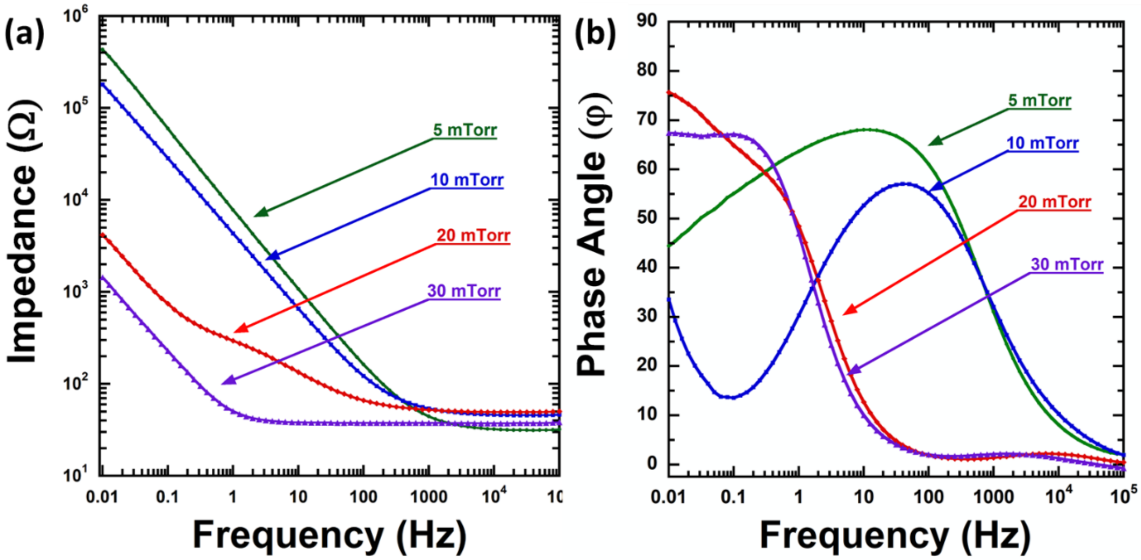

Figure 5.47. EIS Bode (a) modulus impedance (b) phase angle plots of reactively sputtered RuO_x films deposited on 316 SS and synthesized at 20% OPP.

Table 5.11

ECM Elements for RuO_x Parameters, and Values[a]

Element	R_s	R_p	W_T		C_{dl}	R_{ct}	C_{far}	CPE_{ads}	
Parameter	R(Ω)	R(Ω)	$Y_0(S\bullet s^{1/2})$	$B(s^{1/2})$	C(F)	R(Ω)	C(F)	$Y_0(S\bullet s^{1/2})$	N
Value[b]	34	0.43	0.075	0.84	3.3E-05	116	0.0065	0.0077	0.65

[a] *Films synthesized at 20% OPP and 30mTorr WP*

[b] *$\chi^2 = 0.005$*

5.4.2 Summary and Conclusions

Despite the lower performance of films synthesized at 50 and 80% OPP, RuO_x films deposited at 20% OPP show the highest electrochemical performance among the four single metal oxide systems as measured by CSC_C and as shown in Table 5.12. This is assisted by the apparent activation of the Ru(III)/Ru(IV) oxidation states at lower WPs. Similar developmental progression of microstructure as a function of WP observed in the other three single metal oxide systems occurs in the RuO_x system. This is confirmed by SEM cross sections and electrochemical analyses. However as previously mentioned, the planarized polygonal grains that grow at 50 and 80% OPP are detrimental to electrochemical performance. This decrease is attributed to decreased roughness and more generally a decrease in the ESA in these coatings. RuO_x films were also used to demonstrate the effect of substrate dependence on electrochemical performance by comparing the CSC of films deposited on as-rolled 316 SS and SiO_2/Si substrates. The results demonstrate that for the substrate materials utilized in this thesis, the contributions of substrate, whether it be templating or otherwise towards the enhancement of electrochemical performance is small and the fundamental trends are not impacted by choice of substrate material.

Table 5.12

Cathodic Charge Storage Capacity and Maximum Impedance of RuO_x[a]

Working Pressure (mTorr)	5	10	20	30
CSC_C (mC/cm^2)	7.0 ± 1.8	15 ±3.0	29 ± 1.8	56 ± 1.2
Impedance (Ω)	85414	3617	1385	942

[a] *Films synthesized at 20% OPP and 30mTorr WP*

5.5 Single Metal Oxide Thin Films Cytotoxicity

Cytotoxic testing of binary oxide films synthesized at 30 mTorr and 20% OPP were carried out as outlined in section 4.5. As shown in Fig. 5.48, no cytotoxic effects were identified in day 1. After the third day, IrO_x, Rh_xOy, and PdO films continue to show no significant cytotoxic effects while the RuO_x films did show a reduction in cell viability. The IrO_x, Rh_xOy, and PdO films can be said to have good cell adhesion and do not cause cell lysis via apoptosis. On the other hand, the results from the RuO_x cell cultures experience about a 40 % decrease in cell population viability on day 3. This may be due to the cells not adequately adhering to the coated surface or the materials causing apoptotic cell death, or both. All test materials however show excellent cell viability on day 7 including RuO_x which had reduced viability after day 3.

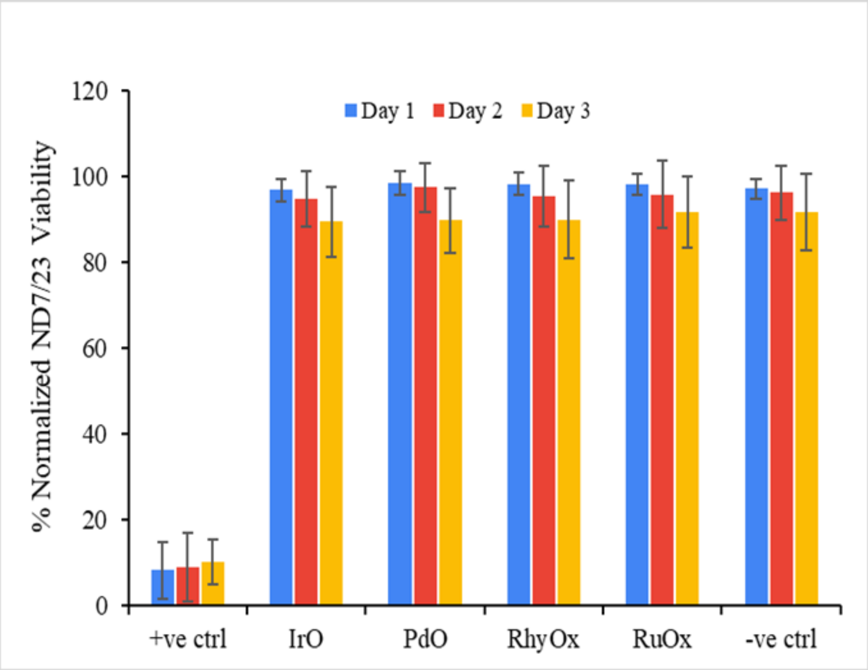

Figure 5.48. Viability of cells grown on the single metal oxide thin films. The Cu and Si are the positive and negative controls, respectively.

5.6 Single Metal Oxide Thin Films Summary and Conclusions

The IrO_x power density study demonstrated that the electrochemical properties of films are improved when sputter deposition of films is performed at lower power densities (specifically 2.5 and 4.9 W/cm^2). The λ_{mfp} and incident energies of PdO were modeled by Monte Carlo method simulations. The simulations along, with the SEM micrographs and, ECM suggest that the growth of columnar and porous substructures observed across all single metal oxide systems is a consequence of shorter λ_{mfp} and thereby lower incident particle energies. XRD analysis of the as-deposited PdO films revealed that films experience a considerable expansion in d-spacing as measured by the (011) lattice constant. This expansion is assumed to be from interstitial implantation of oxygen from energetic NOI bombardment. These effects were shown to be greater in films synthesized at higher OPPs and lower WPs. Thermal annealing of the PdO films suggested films undergo defect annihilation and interstitial oxygen migration at temperatures up to 450°C adding credibility to the non-equilibrium configuration argument. Additionally, PdO films which experience the least amount of lattice expansion *i.e.*, those deposited at 20% OPP have improved electrochemical performance. This response indicates that the electrochemical properties of films may be weakly influenced by lattice expansion/contraction. The dependence of substrate material on the electrochemical performance of RuO_x films deposited on 316 SS and SiO_2/Si substrates was investigated. Results clearly demonstrated that the electrochemical performance of films is only slightly influenced by the substrate materials used in this thesis and the trends as a function of deposition parameter are substrate independent

The electrochemical performance was demonstrated to improve with increasing WP for all single metal oxides when synthesized at 20% OPP as shown in Fig. 5.49a and Table 5.13. The evidence strongly suggests that these improvements are a consequence of an increase in porosity and thereby an increase in the ESA of the coatings, as well as the activation of higher oxidation states for the different systems. Considerable microstructural changes occur for the IrO_x and RuO_x systems when synthesized at higher WPs and OPPSs. For IrO_x the resultant nanoflake microstructure, while high performing electrochemically, is mechanically fragile and not well adhered to the substrate. These characteristics make these otherwise high performing films generally less suitable for implantable neural interfacing applications. Additionally, the nanoflake microstructure which is undesirable is shown to grow (but not dominate) at 20% OPP and 30 mTorr WP. On the other hand, RuO_x films at synthesized at high WPs and OPPs grow planarized polygonal grains. The growth of this planarized microstructure results in a considerable reduction in the electrochemical performance of RuO_x. This reduction in performance is attributed to the reduction in ESA and surface roughness making them less suitable for use as implantable neural interface coatings.

Thus, the synthesis conditions which result in films that possess favorable electrochemical and structural properties are identified to be those deposited at 30 mTorr WP, 20% OPP, and lower power densities. These optimal parameters are consistent across all four single metal oxides. With this understanding it is worthwhile to compare the electrochemical performance as a function of thickness of the single metal oxide systems synthesized at the optimized conditions. As shown in Fig. 5.49b, when directly compared the RuO_x, IrO_x, Rh_xO_y, and PdO films are the best to least electrochemically performing, respectively. Interestingly, as shown in Table 5.14 a linear fit of the thickness dependent binary oxide (Fig. 5.49b) films reveals that the Rh_xO_y has the largest gradient across the thicknesses investigated (nearly double that of RuO_x and IrO_x), followed by the RuO_x and IrO_x which have similar gradient, and then the PdO with the most modest slope. This suggests at sufficiently large thicknesses Rh_xO_y will outperform all other single metal oxides assuming the linear dependence is maintained at greater film thicknesses. The differences may be related to the smaller nano-spherical grain clusters observed in the Rh_xO_y films.

The investigation of the single metal oxides has produced a consistent set of synthesis parameters which yield exceptional electrochemical properties and favorable microstructures. Furthermore, investigations into the biocompatibility of films via a cell viability assay using neuronal cells suggests that the binary oxide materials are non-cytotoxic with all materials showing strong cell viability after 7 days. In aggregate, these findings were used to facilitate and expedite the investigation of the binary and ternary metal oxides in the following chapters.

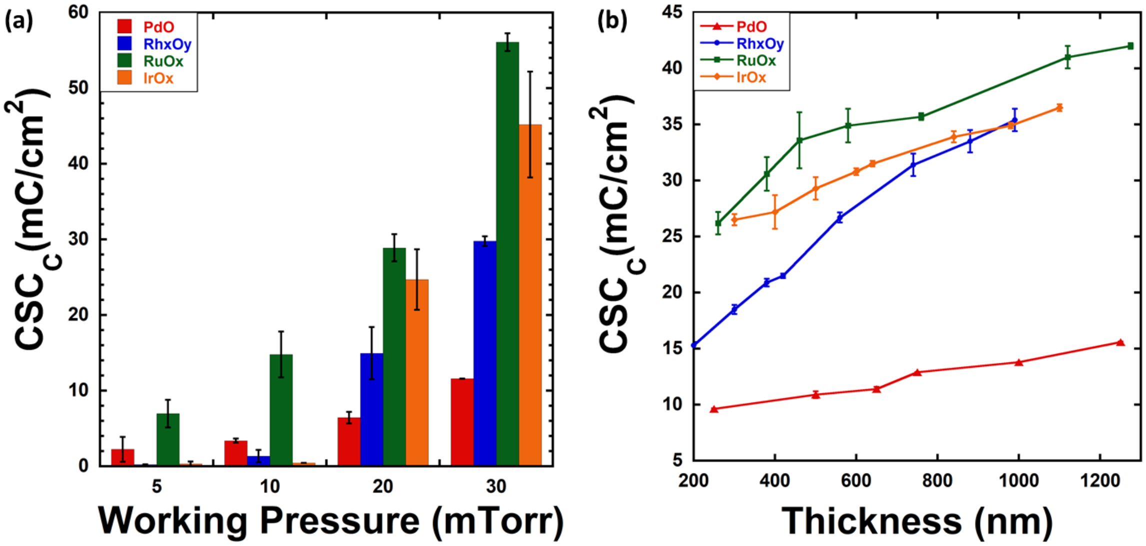

Figure 5.49. (a) The CSC_C of the single metal oxide thin films synthesized at 20% OPP as a function (a) WP. (b) The CSC_C as a function of coating thickness for the single metal oxide films synthesized at 20% OPP and 30 mTorr WP.

Table 5.13

Electrochemical Performance of Single Metal Oxides [a]

Binary Oxide[a]	WP (mTorr)	CSC_C (mC/cm^2)	Max Impedance (Ω)
IrO_x	5	0.33 ± 0.033	210410
PdO	5	2.3 ± 1.6	104100
Rh_xO_y	5	0.24 ± 0.013	434330
RuO_x	5	7.0 ± 1.8	85414
IrO_x	10	0.46 ± 0.0042	155210
PdO	10	3.4 ± 0.27	62986
Rh_xO_y	10	1.4 ± 0.82	180000
RuO_x	10	15 ± 3.0	3617
IrO_x	20	25 ± 4.0	4756
PdO	20	6.4 ± 0.77	34271
Rh_xO_y	20	15 ± 3.4	4178
RuO_x	20	29 ± 1.8	1385
IrO_x	30	45 ± 7.01	1036
PdO	30	11.6 ± 0.53	6072
Rh_xO_y	30	30 ± 0.72	1447
RuO_x	30	56 ± 1.2	942

[a] *Films synthesized at 20% OPP*

Table 5.14

Linear Fit Parameters for Single Metal Oxide Thin Films[a]

Binary Metal Oxide[a]	Intercept	Slope	R
IrO_x	22.8	0.013x	0.993
PdO	7.96	0.006x	0.989
Rh_xO_y	10.9	0.026x	0.992
RuO_x	25.3	0.014x	0.959

[a] *Films synthesized at 20% OPP and 30mTorr WP*

Chapter 6

Binary Metal Oxide Thin Films

This chapter contains the results for the $Ir_{(1-x)}M_x$ (M = Pd, Rh, Ru) binary metal oxide systems. Films were first characterized by identifying microstructures and the range of compositions that were deposited by a combinatorial method. In addition, the solute concentrations of the M metals were identified which suppress nanoflake microstructure. Films were then electrochemically characterized via CV. The results are presented as the CSC_C as function of composition (ratio of metals present in the coating or atomic percent oxygen content). The CSC_C of the single metal endmember oxides synthesized under identical sputtering pressure conditions are included for comparison.

6.1 $Ir_{(1-x)}Pd_x$ Oxide Thin Films

In the following sections the characterization of $Ir_{(1-x)}Pd_xO_y$ thin films deposited by combinatorial synthesis as outlined in section 3.4.2 are discussed. Approximately 60 compositions were selected and characterized from one deposition. The CSC_C of the 30 mTorr WP and 20% OPP coatings were measured on the as-deposited $Ir_{(1-x)}Pd_xO_y$ films deposited on 316 SS substrates. The thicknesses of the films were estimated from a secondary deposition. Due to the inexact nature of the estimations, a standard least squares regression model was performed with JMP® software to assist with thickness estimation.

6.1.1 Results and Discussion

Representative microstructures of the $Ir_{(1-x)}Pd_xO_y$ films are presented in Figs. 6.1. $Ir_{(1-x)}Pd_xO_y$ films with low Pd content ($x = 0.14$) develop nano-spherical grains which cluster into large irregular shapes as shown in Fig. 6.1a. The microstructure is reminiscent to that of the 20% OPP and 30 mTorr WP IrO_x films (Fig. 5.8a) but with more tightly packed grain clusters. At these high Ir concentrations some evidence of nanoflake microstructure is present as noted in Fig. 6.1a. However, the incorporation of Pd is largely able to suppress nanoflake growth. Between $0.14 < x < 0.90$ the microstructure is dominated by nano-spherical grains that combine into small clusters as shown in Fig. 6.1b. At Pd concentrations around $x \geq 0.90$ $Ir_{(1-x)}Pd_xO_y$ films begin to adopt microstructure that resembles that of the endmember PdO as shown in Fig. 6.1c. The microstructure in this zone features large irregularly shaped polygonal grains which grow from surfaces composed of the nano-spherical grains observed in the intermediate solid solution region ($0.14 < x < 0.90$).

The changes in microstructure are reflected in the changes XRD patterns for $Ir_{(1-x)}Pd_xO_y$ deposited at 10 mTorr shown in Fig. 6.2. Above approximately $x = 0.92$ the crystal structure of the $Ir_{(1-x)}Pd_xO_y$ films adopts that of the PdO endmember. Over the intermediate range of compositions ($0.92 < x < 0.18$), films lack any long-range structural ordering except for a small (011) peak observed in the XRD patterns. Above $x = 0.18$, films likely adopt the IrO_x crystal structure, as indicated by the nanoflake growth at approximately $x = 0.14$ observed in the 30 mTorr WP samples.

This structural evolution is notable as it suggests that initially Pd is substitutionally replaced by Ir at high Pd concentrations ($x \geq 0.90$) in the PdO crystal structure making it a primary solid solution. This is followed by the growth of an intermediate solid solution over the compositional ranges $0.14 < x < 0.90$. The crystal structure over this intermediate region is disordered and deviates from the structure of either of the single metal oxide endmembers. Finally, at Pd concentrations of approximately $x \leq 0.14$ films are again primary solid solutions as indicated by the presence of nanoflake-like microstructure. At this compositional region however, the IrO_x crystal structure is primary with Pd substituting into the Ir-lattice sites.

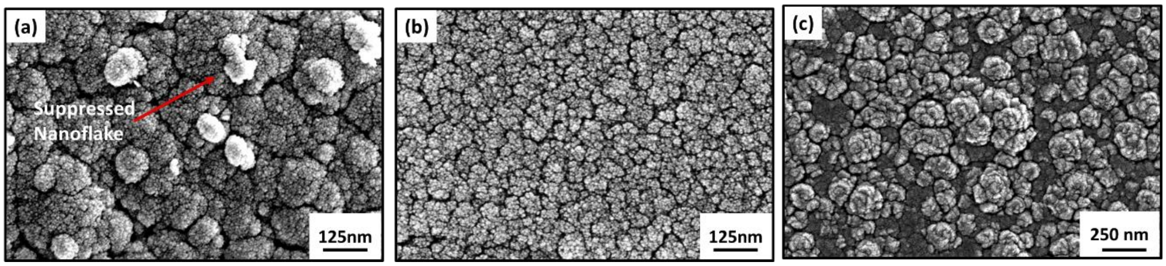

Figure 6.1. SEM micrographs of $Ir_{(1-x)}Pd_xO_y$ deposited on 316 SS substrates synthesized at 30 mTorr and 20% OPP with Pd content of (a) x = 0.16 (b) x = 0.50 and (c) x = 0.90.

The solubility limit of each metal into the others oxide lattice can be inferred from the micrographs, XRD patterns, and knowledge of their respective compositions (Fig. 6.3a). The Hume-Rothery rules, which describe the solubility of an element into a metal to form a solid solution can be applied to metal oxide systems with some additional considerations(184). The Hume-Rothery rules state the following:

1. Accommodation in appreciable quantities of a solute atom into a solvent (substitutionally) can be achieved if the atomic size difference of each of the atoms is no more than 15%. For oxides which involve cations (metals) and anions (oxygen) this is changed to the ionic radius. For this thesis we consider the ionic radius based on the assumed oxidation states of the metals (shown in Table 2.2).
2. Both materials must possess the same crystal structure.
3. Each element must have similar electronegativity. The larger the difference in electronegativity the greater likelihood of forming an intermetallic compound (crystal structure of the compound differs from that of both the endmembers).
4. Elements should have identical valency; However, metals with higher valency are more likely to be accommodated.

With these considerations and the elemental values provided in Table 2.2, it can be assumed that there will be limited solubility of Pd into IrO_x and *vice-versa*. For instance, Pd^{2+} dissolving into the lattice position of Ir^{4+} will result in a cation vacancy (185) and a non-neutral crystal structure with two uncompensated electrons (*i.e.*, one O^{2-}). As a consequence, adjacent Ir^{+4} could be reduced to Ir^{3+} to maintain charge neutrality. Alternatively, the creation of vacancies could also occur. Additionally, the size factor and valency (considering the ionic radii of the assumed oxidation states) are also likely to play a meaningful role in the solubility of the metals.

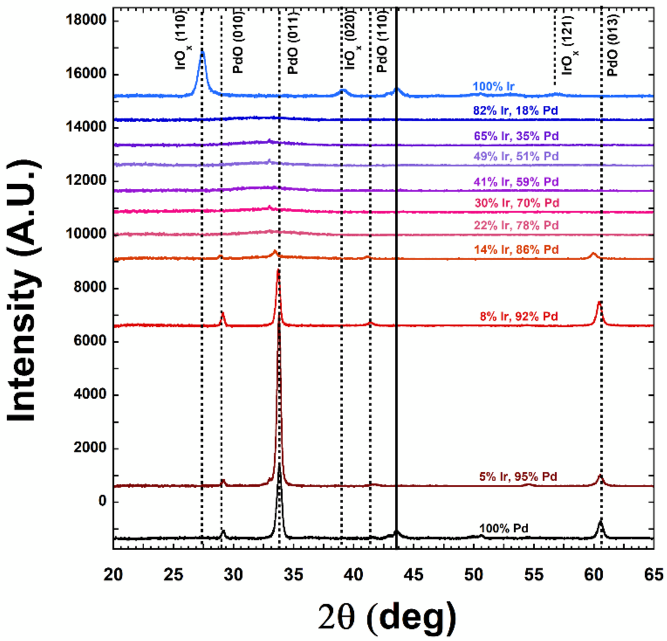

Figure 6.2. X-ray diffraction patterns of $Ir_{(1-x)}Pd_xO_y$ films synthesized at 10mTorr and 20% OPP.

A standard least squares model was used to predict film thicknesses that could not be matched with measurements determined from the secondary binary metal oxide deposition. To identify key relations between parameters, a full factorial design was selected which took into consideration the metallic ratio of metals, oxygen content (at. %), and CSC_C of the single and binary metal oxides. The known thicknesses of the single and binary metal oxide films were also included to approximate unknown film thicknesses.

Regardless of the underlying mechanics behind the suppression of nanoflake growth, the resultant microstructures possess desirable mechanical characteristics. To completely evaluate the suitability of these films for neural interfacing applications the electrochemical properties of the films were measured via CV. The CSC_C as a function of thickness for the $Ir_{(1-x)}Pd_xO_y$ films deposited at 30 mTorr and 20% OPP is presented in Fig. 6.3b. Only $Ir_{(1-x)}Pd_xO_y$ films which possessed similar metallic concentrations within a tolerance of $x \pm 0.01$ and had different thicknesses are reported. Furthermore, the CSC_C as a function of thickness that was previously presented for the single metal oxides in Section 5.6 for the IrO_x and PdO endmembers are included for comparison. The linear fit of the data was used for better comparison between the compositions and systems. Furthermore, the endmember single metal oxides possessed a linear-like thickness dependence when synthesized under similar conditions, thus it is assumed that a similar characteristic should manifest in the binary metal oxide films. Generally, the CSC_C trends upward with decreasing Pd-concentrations with all compositions possessing superior electrochemical performance when compared to that of the PdO endmember. On the other hand, only compositions where $x \geq 0.23$ possess superior electrochemical performance over the IrO_x endmember. The CSC_C data also suggests that at compositions where Pd is assumed to be close to its solubility limit in the IrO_x metal lattice sites *i.e.*, $x \approx 0.15$, the CSC_C exceeds all other compositions for thicknesses greater than or equal to 800 nm. The difference in the gradient observed at $x \approx 0.15$ may be related to changes in film morphology and microstructure that occur at this threshold. This behavior is similar to that observed in the Rh_xO_y films when its CSC_C was compared to the other single metal oxides as a function of thickness.

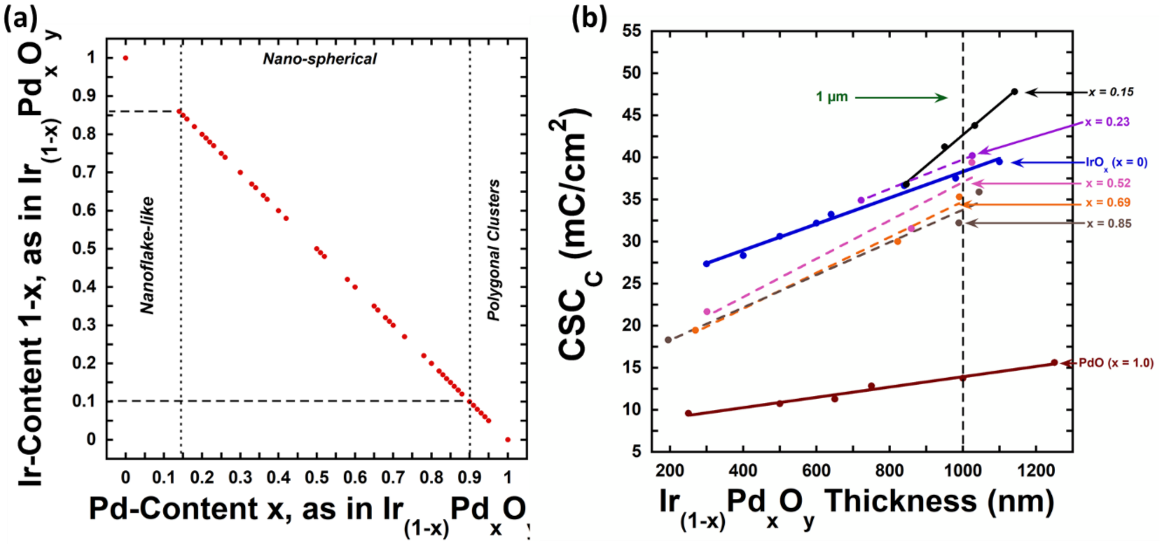

Figure 6.3. (a) Composition of $Ir_{(1-x)}Pd_xO_y$ films synthesized at 20% OPP and 30 mTorr WP based on relative metallic content and expected microstructural characteristics. (b) CSC_C as a function of film thickness of $Ir_{(1-x)}Pd_xO_y$ which developed a thickness gradient. The results from the single metal oxides endmembers of PdO and IrO_x (non-nanoflake) are included for comparison.

6.1.2. Summary and Conclusions

The incorporation of Pd into the lattice of IrO_x completely suppressed nanoflake growth at $Ir_{(1-x)}Pd_xO_y$ concentrations of $x > 0.14$ resulting in high performing coatings with favorable microstructural properties. This Pd concentration coincides with what is believed to be the approximate primary solid solution solubility limit of Pd into IrO_x *i.e.*, the limit where the $Ir_{(1-x)}Pd_xO_y$ system still adopts the crystal structure of IrO_x. This was determined qualitatively by comparing the SEM micrographs, compositional data, and XRD patterns of various $Ir_{(1-x)}Pd_xO_y$ compositions. The $Ir_{(1-x)}Pd_xO_y$ microstructures that develop over approximately $0.14 \leq x < 0.90$ consisted of nano-spherical grain clusters of various sizes. Through similar consideration of the primary solid solution range, the $Ir_{(1-x)}Pd_xO_y$ system over this compositional range is assumed to be an intermediary solid solution wherein the resultant crystal structure differs from either of the endmember oxides. Above x ≥ 0.90 Pd concentrations, $Ir_{(1-x)}Pd_xO_y$ films grew large polygonal-like grains which were reminiscent of the PdO endmember microstructure (Fig. 5.19). A large range of $Ir_{(1-x)}Pd_xO_y$ compositions (x ≥ 0.14) were shown to grow favorable microstructures for implantable neural interfacing applications.

The various compositional and thickness gradients that naturally develop as a result of the combinatorial method used enabled an investigation of the CSC_C as a function of thickness and composition. Results showed for all compositions which developed a thickness dependence, the electrochemical properties of the $Ir_{(1-x)}Pd_xO_y$ films were superior to that of the PdO endmember. On the other hand, only $Ir_{(1-x)}Pd_xO_y$ compositions with x ≤ 0.23 possessed improved electrochemical performance over the non-nanoflake dominated IrO_x endmember.

6.2. $Ir_{(1-x)}Ru_x$ Oxide Thin Films

In the following sections the characterization of $Ir_{(1-x)}Ru_xO_y$ thin films deposited by combinatorial synthesis as outlined in section 3.4.2 are discussed. Approximately 60 compositions were characterized from one deposition. The CSC_C of the 30 mTorr WP and 20% OPP coatings were measured on the as-deposited $Ir_{(1-x)}Ru_xO_y$ films deposited on 316 SS substrates. The endmember oxides synthesized under identical sputtering conditions are included for comparison. The thicknesses of the films were estimated from a secondary deposition. Due to the inexact nature of the estimations, a standard least squares regression model was implemented as described in Section 6.1.1 with JMP® software to assist with thickness estimation.

6.2.1. Results and Discussion

Representative microstructures of $Ir_{(1-x)}Ru_xO_y$ films over a range of compositions are shown in Fig. 6.4. Nanoflake-like microstructure (not shown) begins to grow in $Ir_{(1-x)}Ru_xO_y$ films at approximately $x < 0.34$. As the Ru content x approaches 0.34, the microstructure adopts the familiar nano-spherical grain clustering that has been observed in some other oxide systems. Mirroring the $Ir_{(1-x)}Pd_xO_y$ system, the $Ir_{(1-x)}Ru_xO_y$ similarly develops nano-spherical grains in the intermediary compositional solid solution ranges ($0.34 > x > 0.7$) as depicted in Fig. 6.4b. As shown in Fig.6.5c for high Ru concentrations ($x \geq 0.70$) the $Ir_{(1-x)}Ru_xO_y$ system grains become increasingly polygonal, reminiscent of the RuO_x films synthesized at 20% OPP and 30 mTorr WP. At these higher Ru concentrations, the $Ir_{(1-x)}Ru_xO_y$ surfaces consist of nano-spherical grains that cluster into irregularly shaped polygonal structures. These polygonal-like grain clusters are apparently much more angular than that of the RuO_x endmember counterpart. The range of compositions based on the atomic ratio of Ir/Ru and the corresponding distinguishing microstructural characteristics are summarized in Fig. 6.5a.

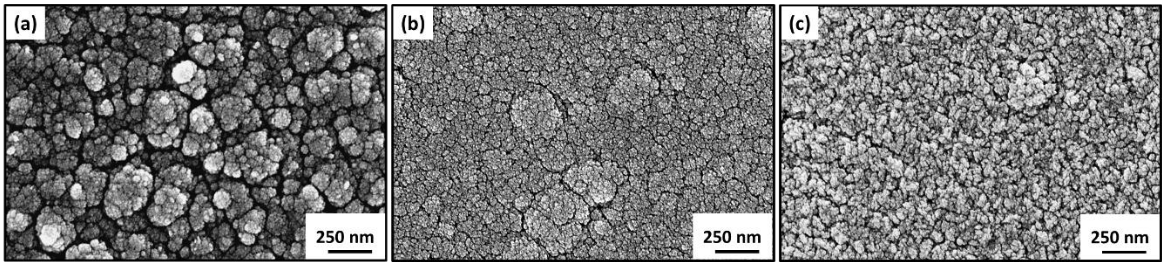

Figure 6.4. SEM micrographs of $Ir_{(1-x)}Ru_xO_y$ deposited on 316 SS substrates synthesized at 30 mTorr and 20% OPP with Ru content of (a) $x = 0.34$ (b) $x = 0.50$ and (c) $x = 0.70$.

The CSC_C for the $Ir_{(1-x)}Ru_xO_y$ films as function of composition and thickness is presented in Fig. 6.5b. The slope of the CSC_C as a function of thickness of each composition of $Ir_{(1-x)}Ru_xO_y$ was greater than that of the single metal oxide endmembers. Additionally, the cross-over thicknesses where the binary metal oxide system exceeds the electrochemical performance of the endmember oxides were approximately 600 nm, and 600-700 nm, for IrO_x and RuO_x, respectively. At 1 µm the electrochemical performance of the $Ir_{(1-x)}Ru_xO_y$ films was considerably greater than that of either of the single metal oxide endmembers. Furthermore, the CSC_C improved as Ru content in the films increased.

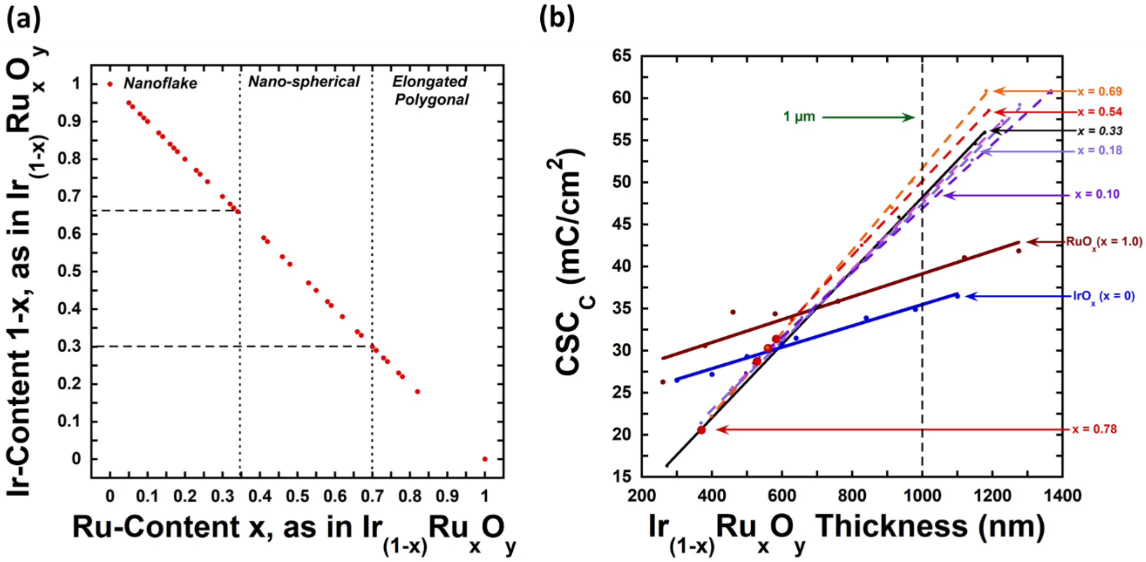

Figure 6.5. (a) Composition of $Ir_{(1-x)}Ru_xO_y$ based on relative metallic content and expected microstructural characteristics. (b) CSC_C as a function of film thickness of $Ir_{(1-x)}Ru_xO_y$ which developed a thickness gradient. The results from the single metal oxide endmembers of RuO_x and IrO_x are included for comparison.

6.2.2 Summary and Conclusions

Similar to the other binary metal oxide systems, the microstructural features of the $Ir_{(1-x)}Ru_xO_y$ system are determined by metallic concentration suggesting that performance can be tailored. Among the microstructures present are the previously discussed nanoflakes which grow at $x < 0.34$ (not shown), the transitionary microstructure characterized by large grain clusters at $x \approx 0.34$, the intermediary microstructure consisting of small clusters of nano-spherical grains at $0.34 < x < 0.7$, and the polygonal-like grains at $x \geq 0.70$. Thus, the approximate primary solid solution limits based on relative metallic concentration for the $Ir_{(1-x)}Ru_xO_y$ system are approximately $x = 0.34$ for Ru into IrO_x is $x \approx 0.34$, and $1-x = 0.30$ for Ir into RuO_x.

Generally, the electrochemical performance of the $Ir_{(1-x)}Ru_xO_y$ films eclipse that of the single metal oxide endmembers at film thicknesses 700 nm. Notably, films which grew nanoflake microstructure ($x < 0.34$) possessed lower performance when compared to their non-nanoflake counterparts. Furthermore, electrochemical performance improved as Ru content x increased in films. Additionally, non-nanoflake $Ir_{(1-x)}Ru_xO_y$ films possessed higher electrochemical performance over the nanoflake $Ir_{(1-x)}Ru_xO_y$ films. For the $Ir_{(1-x)}Ru_xO_y$ system, depending on film composition and thickness, it has been shown that the electrochemical performance of films can be enhanced over the single metal oxide endmembers while maintaining desirable microstructures.

6.3 $Ir_{(1-x)}Rh_x$ Oxide Thin Films

In the following sections the characterization of $Ir_{(1-x)}Rh_xO_y$ thin films deposited by combinatorial synthesis as outlined in section 3.4.2 are discussed. Approximately 60 compositions were characterized from one deposition. The CSC_C of the 30 mTorr WP and 20% OPP coatings were measured on the as-deposited $Ir_{(1-x)}Rh_xO_y$ films deposited on 316 SS substrates. The results from the single metal oxide endmembers synthesized under identical sputtering conditions are included for comparison. The thicknesses of the films were estimated from a secondary deposition. Due to the inexact nature of the estimations, a standard least squares regression model as described in Section 6.1.1 was performed with JMP® software to assist with thickness estimations.

6.3.1 Results and Discussion

Representative microstructures which grow at various compositions of $Ir_{(1-x)}Rh_xO_y$ are presented in Fig. 6.6. At x concentrations < 0.50, the $Ir_{(1-x)}Rh_xO_y$ films grow nanoflake (not shown) and mixed nano-spherical/flake microstructure as shown in Fig. 6.1a. $Ir_{(1-x)}Rh_xO_y$ with Rh concentrations of approximately $x \approx 0.50$ grow variably sized tightly packed clusters of nano-spherical grains as shown in Fig. 6.6a. Between $0.50 < x < 0.85$, $Ir_{(1-x)}Rh_xO_y$ films develop nano-spherical grains which grow into small clusters as shown in Fig. 6.6c. At $x = 0.85$ (Fig. 6.6d), films grow nano-spherical grains clustered similarly to that of the Rh_xO_y endmember. The range of compositions based on the metallic ratio of metals and expected microstructures are shown in Fig. 6.7a. The complete suppression of nanoflake growth was observed to be at Rh concentrations of $x \geq 0.50$.

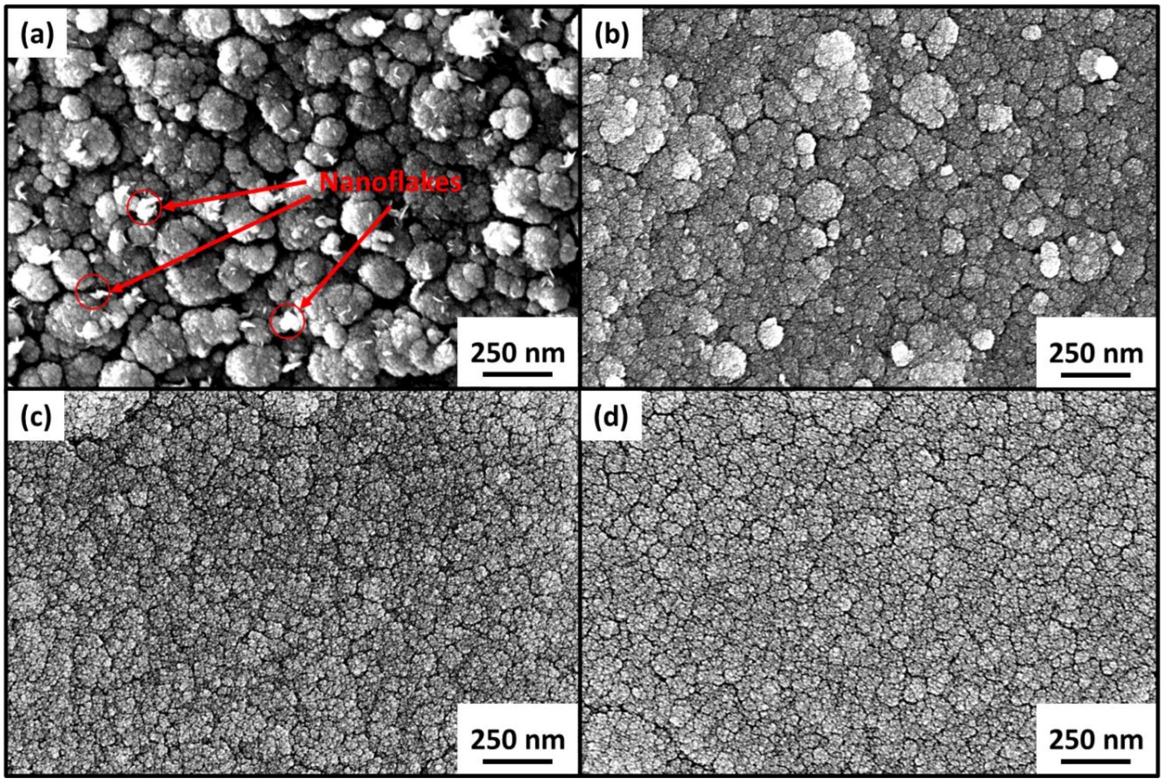

Figure 6.6. SEM micrographs of $Ir_{(1-x)}Rh_xO_y$ deposited on 316 SS substrates synthesized at 30 mTorr and 20% OPP with Rh content of (a) x = 0.42 (b) x = 0.50 and (c) x = 0.80 (d) x = 0.85.

The CSC_C as a function of thickness and composition of the $Ir_{(1-x)}Rh_xO_y$ films is presented in Fig. 6.7. The $Ir_{(1-x)}Rh_xO_y$ solid solutions possessed superior electrochemical performance when compared to either of the endmember single metal oxides at thicknesses above 750 nm. Generally, as the Rh content is increased the electrochemical performance is reduced in the $Ir_{(1-x)}Rh_xO_y$. The highest performing films are those that are dominated by nanoflake growth (x = 0.08 and 0.24). Films which are dominated by nano-spherical growth but possessed some nanoflake microstructure (x = 0.43) had similar electrochemical performance to films which grew large clusters of nanospherical grains

($x \approx 0.50$). The slope of the CSC_C as a function of thickness is shown to change at a rate in between that of the endmember oxides.

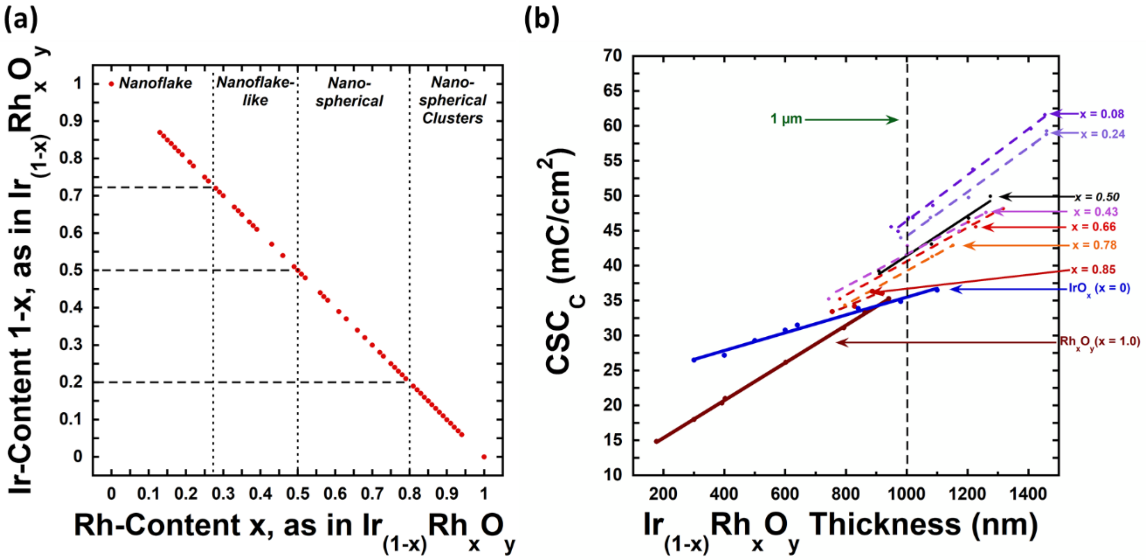

Figure 6.7. (a) Composition of $Ir_{(1-x)}Rh_xO_y$ based on relative metallic content and expected microstructural characteristics. (b) CSC_C as a function of film thickness of $Ir_{(1-x)}Rh_xO_y$ which developed a thickness gradient. The results from the single metal oxide endmembers of Rh_xO_y and IrO_x are included for comparison.

6.3.2 Summary and Conclusions

Based on the composition and microstructural changes of the $Ir_{(1-x)}Rh_xO_y$ films, Rh has a larger primary substitutional solubility window ($x \approx 0.50$) into the IrO_x lattice than the other two binary metal oxide systems evaluated. On the other hand, the substitution of Ir into the Rh_xO_y lattice is much more limited and is believed to be around Ir concentrations 1 – x of approximately 0.20. Regardless of composition the $Ir_{(1-x)}Rh_xO_y$ films had enhanced electrochemical performance in comparison to either of the single metal endmember oxides. However, unlike the $Ir_{(1-x)}Ru_xO_y$ system, increasing the concentration of Rh reduced electrochemical performance. Additionally, the electrochemical performance of $Ir_{(1-x)}Rh_xO_y$ films which were dominated by nanoflake growth were the highest performing of the various compositions overall.

6.4 Binary Metal Oxide Thin Films Summary and Conclusions

The compositional ranges for each of the binary metal $Ir_{(1-x)}M_xO_y$ have been identified which suppress nanoflake growth while maintaining high electrochemical performance, and a summary of the results are presented in Table 6.1. Each binary metal oxide system required different solute concentrations in order to transition from a primary solid solution which possessed the IrO_x nanoflake structure to an intermediate solid solution structure which possessed an apparent different crystal structure. Similar concentration limits have been identified for Ir into the MO_x lattice. The solute concentrations required for the microstructural transitions to occur are broadly described by the Hume-Rothery rules (with additional considerations for ceramic systems) and Schottky defect effects. Among the three binary metal oxide systems the $Ir_{(1-x)}Pd_xO_y$ required the least ($x \approx 0.14$), while the $Ir_{(1-x)}Rh_xO_y$ system required the greatest ($x \approx 0.50$) amount of M_x metal for nanoflake growth to be suppressed. In both cases, these values are likely related to the substitutional solubility limits of each element into the others lattice site.

Table 6.1

Resultant Microstructures Based on M-Content for $Ir_{(1-x)}M_xO_y$ [a]

Microstructure Type	Nanoflake	Intermediate	M_x Endmember
$Ir_{(1-x)}Pd_xO_y$	$x < 0.14$	$0.14 \leq x \leq 0.90$	$x > 0.90$
$Ir_{(1-x)}Ru_xO_y$	$x < 0.34$	$0.34 \leq x \leq 0.70$	$x > 0.70$
$Ir_{(1-x)}Rh_xO_y$	$x < 0.50$	$0.50 \leq x \leq 0.80$	$x > 0.80$

[a] *Films synthesized at 20% OPP and 30mTorr WP*

The electrochemical performance of all binary metal oxides improved with increased coating thickness. Additionally, the slope of the CSC_C as a function of thickness for each binary metal oxide systems was higher than that of their endmember single metal oxide counterparts. As a consequence, film thickness had a greater contribution to electrochemical performance such that the binary metal oxides were only able to outperform their single metal oxide endmembers if grown above specific thicknesses. For the $Ir_{(1-x)}Rh_xO_y$ and $Ir_{(1-x)}Ru_xO_y$ systems, all compositions outperformed their single metal oxide endmembers if grown to thicknesses ≥ 750 nm. However, only two compositions (x = 0.15 and 0.23) for the $Ir_{(1-x)}Pd_xO_y$ system were able to electrochemically outperform both endmembers and only if grown at thicknesses ≥ 800 nm. Comparatively, the electrochemical performance of the binary metal oxides at compositions near or at the assumed primary solubility limits of the M metal (Fig. 6.8) indicate that the $Ir_{(1-x)}Ru_x$, $Ir_{(1-x)}Pd_x$, and $Ir_{(1-x)}Rh_x$ oxides are the highest to lowest performing at 1 µm, respectively. Additionally, Fig. 6.8 shows the difference in gradient and CSC_C between the binary metal and single metal oxide endmembers. These differences indicate that in addition to the microstructural changes that were observed, the electrochemical properties of the binary metal oxides may meaningfully deviate from their endmember single metal oxide counterparts.

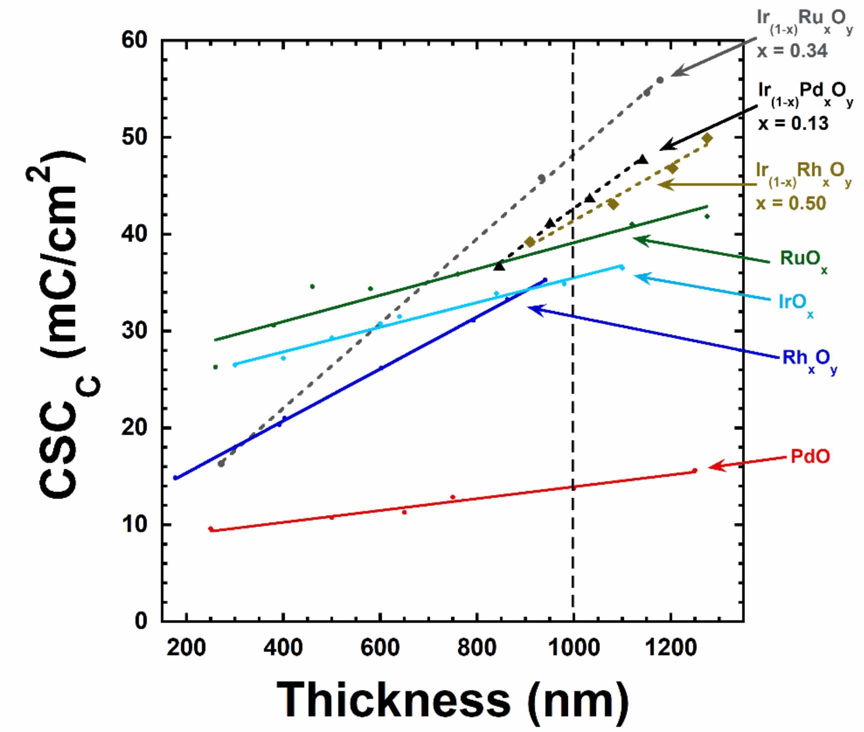

Figure 6.8. CSC_C as a function of film thickness for the primary solubility limit compositions of the binary metal oxides. The results from the single metal oxide endmembers are included for comparison. The vertical dashed line denotes 1 µm film thickness.

Chapter 7

Ternary Metal Oxide Thin Films

This chapter contains the results for the $Ir_{(1-x)}M_xM'_z$ (M = Pd, Rh, Ru) ternary metal oxide systems. Films were first characterized by identifying microstructure and the range of compositions that were developed from utilizing the combinatorial method. In addition, the solute concentration of the $M_xM'_z$ metals were identified which suppress nanoflake microstructure. Films were then electrochemically characterized by CV.

7.1 $Ir_{(1-x-z)}Pd_xRu_z$ Oxide Thin Films

In the following sections the characterization of $Ir_{(1-x-z)}Pd_xRu_zO_y$ thin films deposited via combinatorial synthesis as outlined in section 3.4.3 is discussed. Approximately 60 unique compositions were characterized from one deposition. The CSC_C was measured on the as-deposited $Ir_{(1-x-z)}Pd_xRu_zO_y$ films deposited on 316 SS substrates.

7.1.1 Results and Discussion

Representative microstructures for various compositions of $Ir_{(1-x-z)}Pd_xRu_zO_y$ are presented in Fig. 7.1a-c. The presence of Pd considerably suppressed nanoflake growth in the $Ir_{(1-x-z)}Pd_xRu_zO_y$ system. The resultant microstructure with the highest Ir-content that possessed no evidence of nanoflake formation occurs at x = 0.16 and z = 0.05 and is shown in Fig. 7.1a. The microstructure is characterized by nanosized spherical grains which cluster into particles of various sizes. The microstructure of the $Ir_{(1-x-z)}Pd_xRu_zO_y$ films is shown to adopt that of the closest single/binary metal oxide when in primary solid solution compositional regions. This behavior similarly to what was observed in the binary metal oxide systems. For instance, for the highest Ru content film shown in Fig. 7.1b with x = 0.30 and z = 0.50, the microstructure has features resembling the polygonal grains observed in higher Ru content $Ir_{(1-x)}$ Ru_xO_y and the RuO_x endmember. $Ir_{(1-x-z)}Pd_xRu_zO_y$ films possessing higher Pd content (x = 0.90 and z = 0.020) (Fig. 7.1c) displayed microstructural characteristics resembling those of the high Pd content $Ir_{(1-x)}Pd_xO_y$ and PdO films synthesized under similar conditions. Similar to the binary metal oxide intermediate microstructures, the intermediate solid solution microstructure for the $Ir_{(1-x-z)}Pd_xRu_zO_y$ ternary metal oxides shown in Fig. 7.2 is characterized by small clusters of nano-spherical grains.

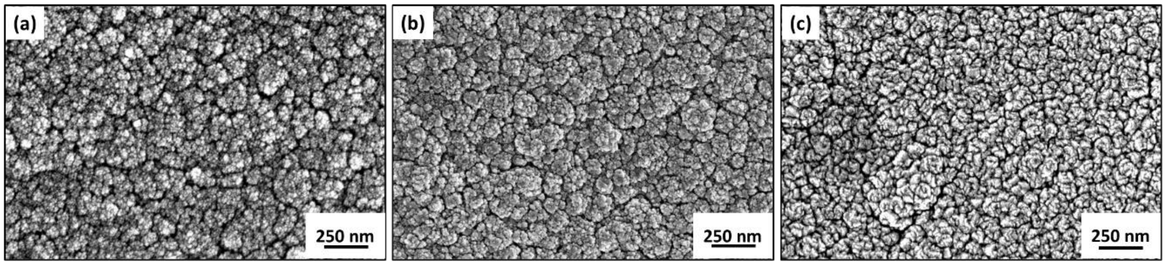

Figure 7.1. SEM micrographs of $Ir_{(1-x-z)}Pd_xRu_zO_y$ deposited on 316 SS substrates with (a) x = 0.16, z = 0.05 (b) x = 0.30, z = 0.59 and (c) x = 0.90, z =0.02.

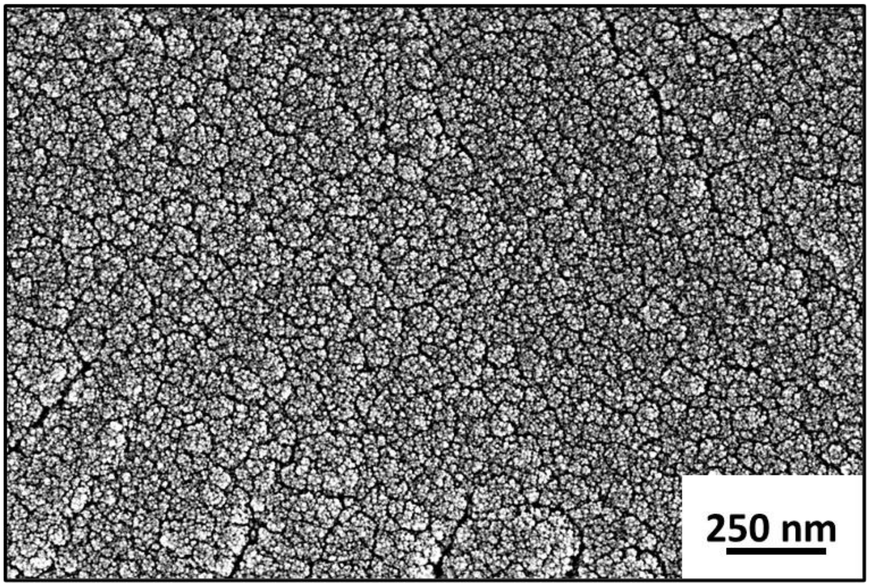

Figure 7.2. SEM micrographs of $Ir_{(1-x-z)}Pd_xRu_zO_y$ deposited on 316 SS substrates with x = 0.36 and z = 0.30.

The ternary density CSC_C plot for $Ir_{(1-x-z)}Pd_xRu_zO_y$ is shown in Fig. 7.3. The aforementioned zone which possessed the highest Ir concentration without any nanoflake microstructural features (x = 0.16, z = 0.05) is shown to have moderately high CSC_C in the range of 49-56 mC/cm^2. It should be emphasized that this plot does not account for variable coating thickness. Several other regions of high CSC_C exist. These include x = 0.37 and z = 0.05, and x = 0.7 and z = 0.08. However, for this thesis the zones which contain a majority Ir are of primary interest due to the well-established role of IrO_x in implantable neural interfacing applications.

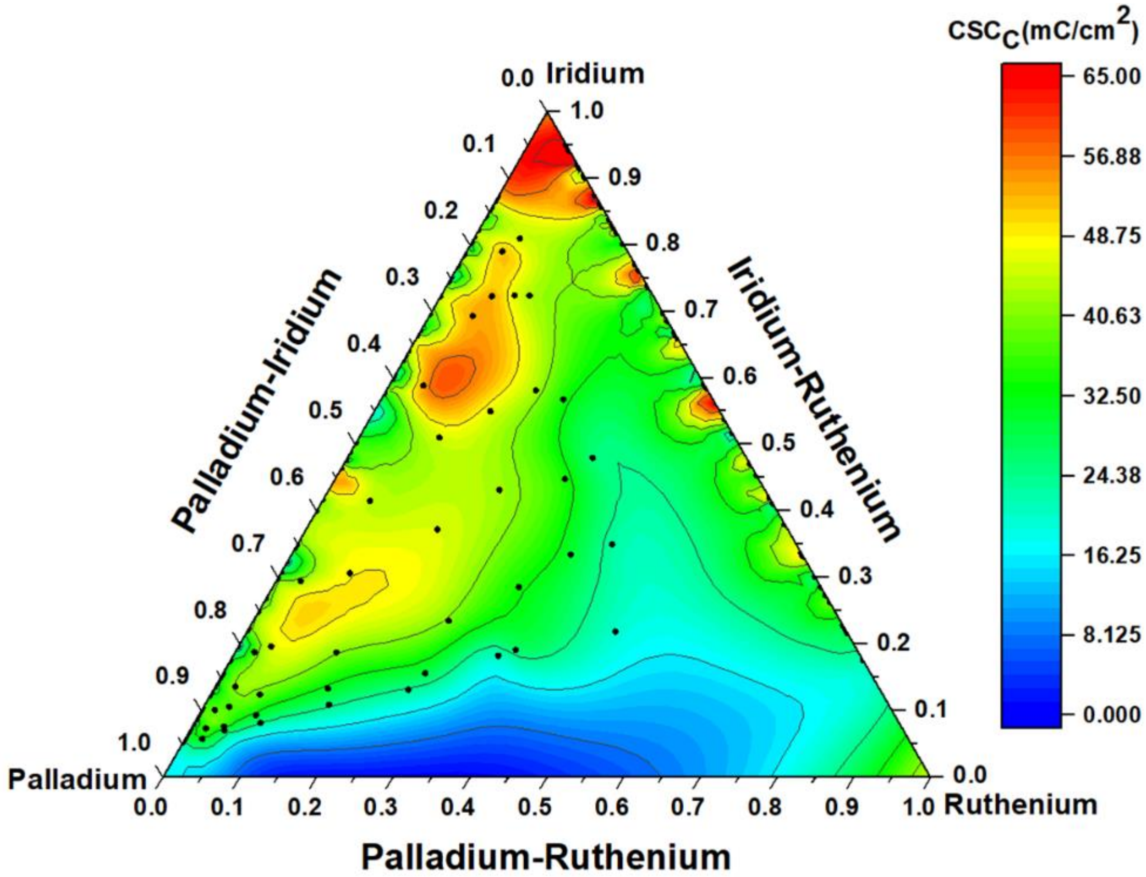

Figure 7.3. Ternary density plot CSC$_C$ for the Ir$_{(1\text{-}x\text{-}z)}$Pd$_x$Ru$_z$O$_y$ coatings measured on 316 SS substrates.

7.1.2 Summary and Conclusions

The microstructures and electrochemical performance have been examined for the Ir$_{(1\text{-}x\text{-}z)}$Pd$_x$Ru$_z$O$_y$ system. Similar to the ternary oxides the films adopt the microstructure of the nearest endmember oxide when in terminal solid solution range. Additionally, the presence of Pd was successful in preventing the domination of nanoflake growth in the range of compositions synthesized.

7.2 $Ir_{(1-x-z)}Pd_xRh_z$ Oxide Thin Films

In the following sections the characterization of $Ir_{(1-x-z)}Pd_xRh_zO_y$ thin films deposited by combinatorial synthesis as outlined in section 3.4.3 is discussed. Approximately 50 unique compositions were characterized from one deposition. The CSC_C was measured on the as-deposited $Ir_{(1-x-z)}Pd_xRh_zO_y$ films deposited on 316 SS substrates.

7.2.1 Results and Discussion

The range of microstructures that develop in the $Ir_{(1-x-z)}Pd_xRh_zO_y$ ternary metal oxide system is represented in Figs. 7.4. In all measured compositions, the growth of nanoflake microstructure was diminished (as shown in Fig. 7.4a) or suppressed altogether, as shown in Fig. 7.4a. The resultant microstructure is similar to the previously observed mixed nano-spherical/nanoflake grain clusters for films close to this primary solubility limit line. Thus, for $Ir_{(1-x-z)}Pd_xRh_zO_y$ compositions where $x < 0.12$, nanoflake microstructure would likely dominate. This value is near the other primary solubility limits observed for Pd containing binary and ternary metal oxides. More favorable microstructures grow at higher Rh concentrations ($x \geq 0.13$, $z \geq 0.12$) as shown in Fig. 7.4b. This intermediary microstructure, similar to that of the other binary and ternary metal oxide systems is characterized by small clusters of nano-spherical grains. Similar to previous observations in the binary and ternary metal oxides, the microstructure of the $Ir_{(1-x-z)}Pd_xRh_zO_y$ adopts that of closest endmember single or binary metal oxide at the primary solid solution ranges. This is shown in the Figs. 7c and 7d, which demonstrate that the $Ir_{(1-x-z)}Pd_xRh_zO_y$ films adopt microstructural characteristics resembling that of the single and binary metal Pd and Rh oxides, respectively.

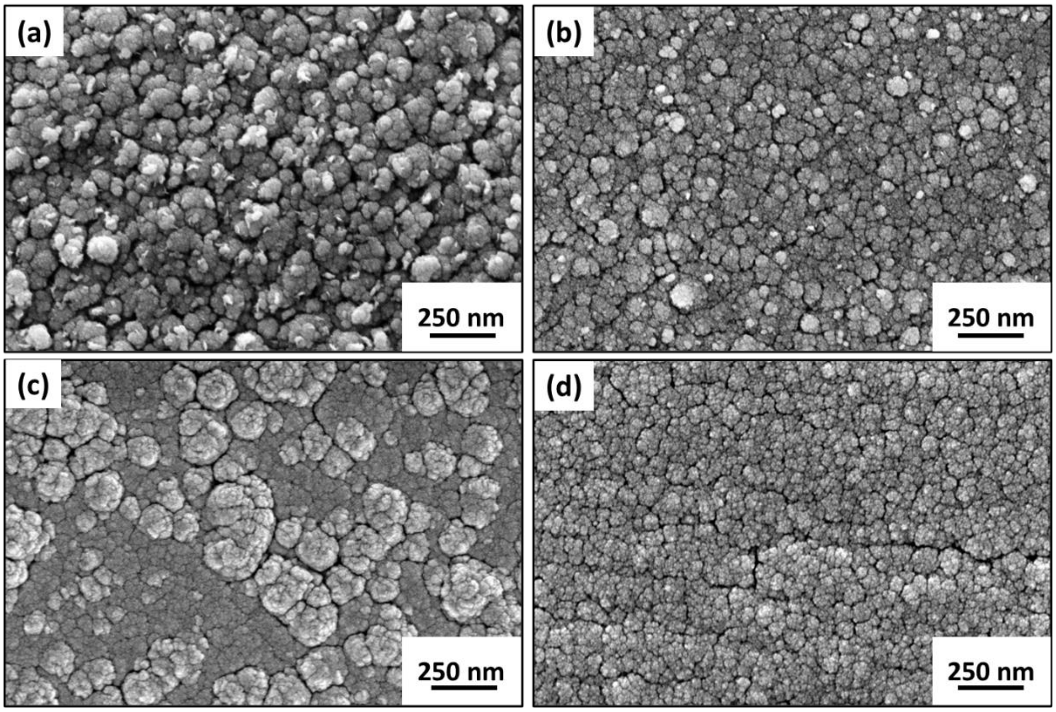

Figure 7.4. SEM micrographs of $Ir_{(1-x-z)}Pd_xRh_zO_y$ deposited on 316 SS substrates with (a) x = 0.12, z = 0.07 (b) x = 0.13, z = 0.12, (c) x = 0.92, z =0.02, and (d) x = 0.21, z = 0.59.

The CSC_C of the various compositions of $Ir_{(1-x-z)}Pd_xRh_zO_y$ are presented in the ternary density plot shown in Fig. 7.5. The high CSC_C region in which Ir is the dominant metal are identified to be between $0.13 \leq x \leq 0.40$, and $= 0.04 \leq z \leq 0.20$. This region has microstructure similar to what is presented in Fig. 7.4a and 7.4b, and the intermediate solid solution microstructures (*i.e.*, Fig. 7.2). An additional high CSC_C compositional region of interest where Pd is the dominant metal exists between $0.50 < x < 0.60$ and

$0.03 < z < 0.16$, with microstructure resembling the intermediate solid solution microstructure depicted in Fig. 7.2.

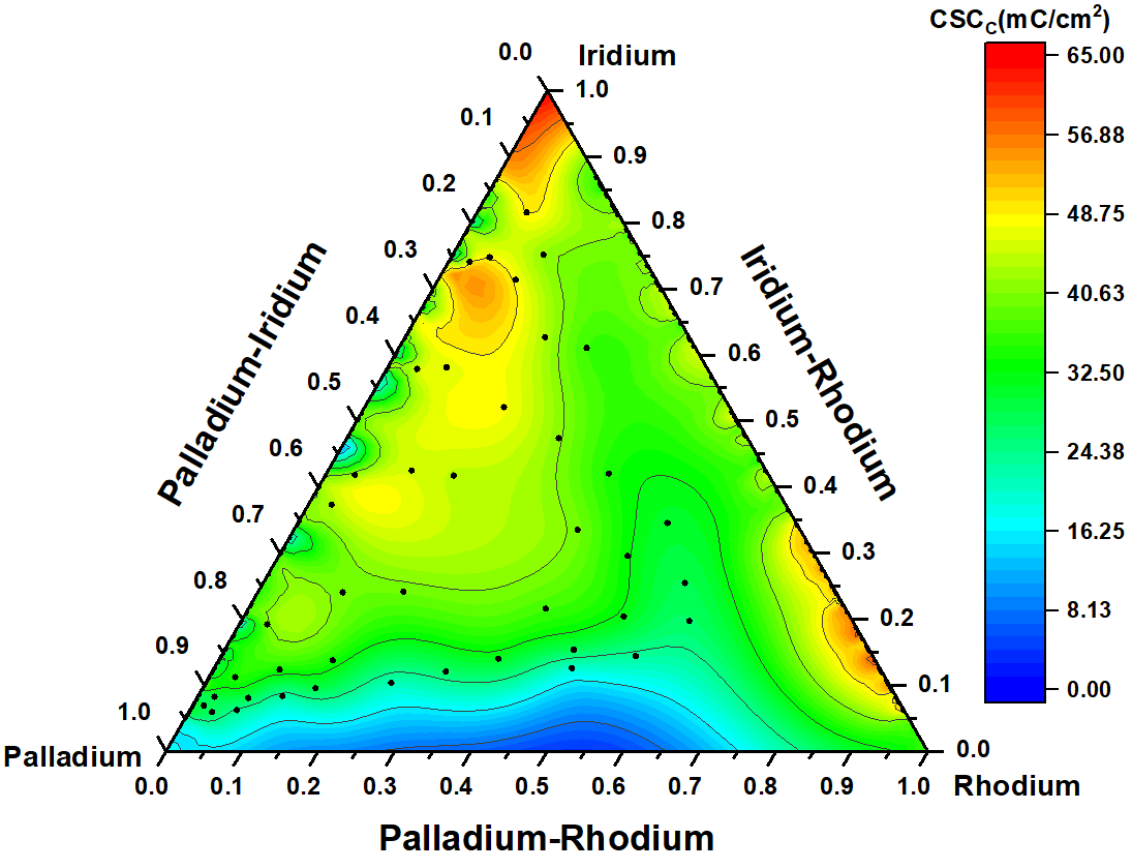

Figure 7.5. Ternary density plot CSC$_C$ for the $Ir_{(1-x-z)}Pd_xRh_zO_y$ coatings measured on 316 SS substrates.

7.2.2 Summary and Conclusions

Similar to the $Ir_{(1-x-z)}Pd_xRu_zO_y$ system, the $Ir_{(1-x-z)}Pd_xRh_zO_y$ system is able to suppress nanoflake growth partially or completely in all compositions investigated. The low solute concentrations required for nanoflake suppression is presumably due to the presence of Pd. The mechanisms behind the microstructural changes are believed to be largely identical to those previously described for the binary metal oxide films (Section 6.1.1). Additionally, when $x \geq 0.13$ nanoflake microstructure is suppressed completely in the $Ir_{(1-x-z)}Pd_xRh_zO_y$ system. The range of compositions and corresponding microstructures which have exceptional electrochemical performance have been identified to be $13 \leq x \leq 0.40$, and $= 0.04 \leq z \leq 0.20$ for Ir-dominant compositions, and $0.50 \leq x \leq 0.60$, and $0.03 \leq z \leq 0.16$ for Pd-dominant compositions.

7.3 $Ir_{(1-x-z)}Ru_xRh_z$ Oxide Thin Films

In the following sections the characterization of $Ir_{(1-x-z)}Ru_xRh_zO_y$ thin films deposited by combinatorial synthesis as outlined in section 3.4.3 is discussed. Approximately 90 unique compositions were characterized from two depositions. The CSC_C was measured on the as-deposited $Ir_{(1-x-z)}Ru_xRh_zO_y$ films deposited on 316 SS substrates.

7.3.1 Results and Discussion

The microstructures representative of the $Ir_{(1-x-z)}Ru_xRh_zO_y$ system are presented in Fig. 7.6. For a large range of compositions, the microstructure is dominated by nanoflake or a combination of nanoflake and nano-spherical grain growth as is depicted in Fig. 7.6a. Intermediary compositions where $x > 0.15$ and $z < 0.15$, and $x > 0.20$ and $z < 0.34$ develop the familiar nanosized grain clusters shown in Fig. 7.6b. The $Ir_{(1-x-z)}Ru_xRh_zO_y$ films begin to adopt the microstructure of the single and binary metal oxide endmembers as composition approaches the primary solid solution range as shown in Fig. 7.6c and 7.6d, for high Ru and high Rh content, respectively.

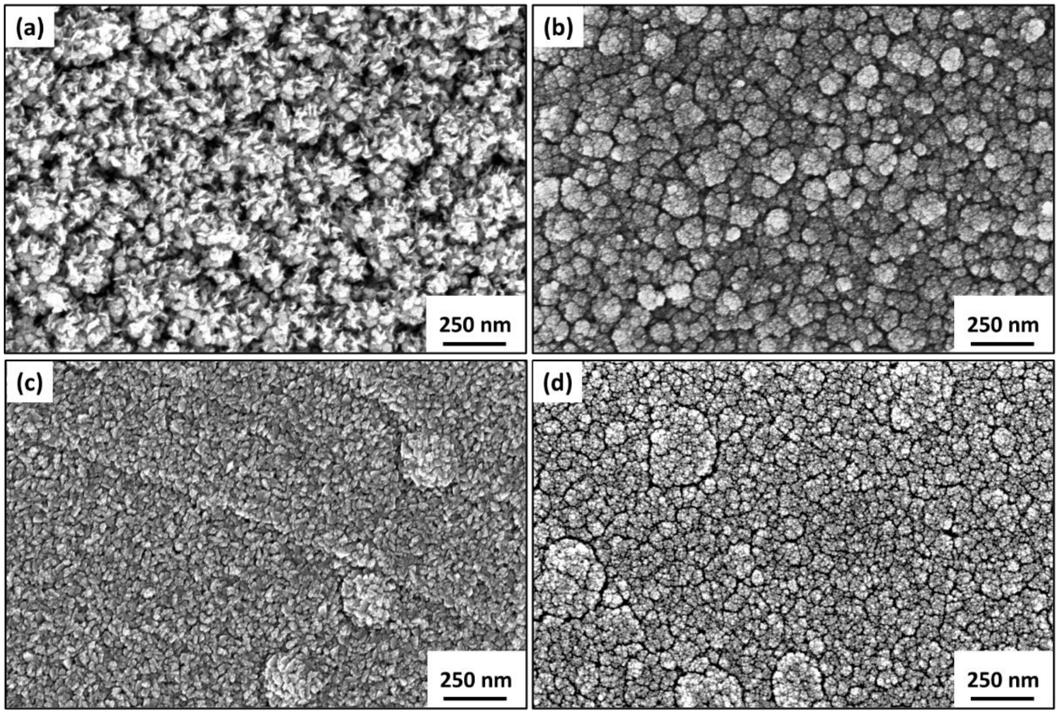

Figure 7.6. SEM micrographs of $Ir_{(1-x-z)}Ru_xRh_zO_y$ deposited on 316 SS substrates synthesized at 30 mTorr and 20% OPP with Ru_xRh_z content of (a) $x = 0.08$, $z = 0.34$ (b) $x = 0.17$, $z = 0.33$, (c) $x = 0.82$, $z = 0.06$, and (d) $x = 0.08$, $z = 0.55$.

A large amount of the $Ir_{(1-x-z)}Ru_xRh_zO_y$ compositions develop nanoflake microstructure. This compositional range is depicted in the shaded regions of the ternary CSC_C diagram shown in Fig. 7.7. Many of the $Ir_{(1-x-z)}Ru_xRh_zO_y$ compositions which contain a majority of Ir are within the shaded region. Despite this, four compositional ranges are identified which still possess exceptional electrochemical characteristics with only one containing a majority Ir content. These ranges include $0.2 \le x \le 0.27$ and $0.14 \le z \le 0.24$ (majority Ir), $0.36 \le x \le 0.45$ and $0.25 \le z \le 0.47$, $0.01 \le x \le 0.15$ and $0.52 \le z \le 0.71$, and $0.04 \le x \le 0.10$ and $0.74 \le z \le 0.82$. The high CSC_C found at higher Rh content is promising as it may suggests that the Rh benefits electrochemically from both Ir and Ru substituting into its lattice sites.

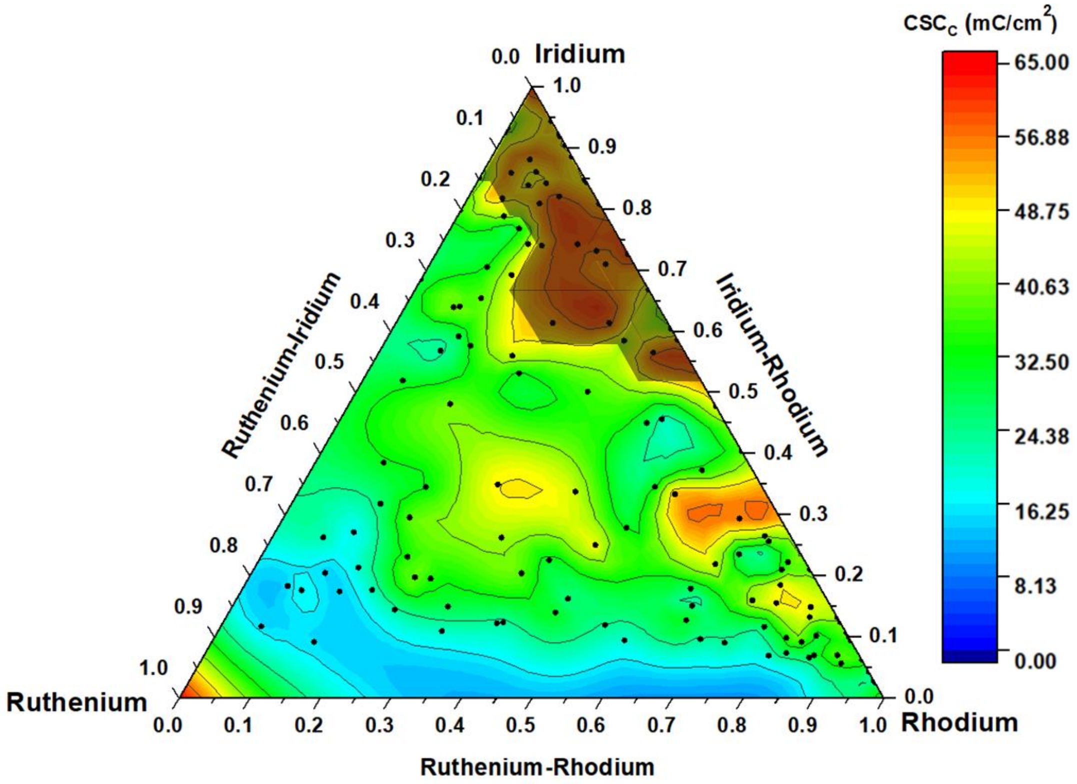

Figure 7.7. Ternary density plot CSC$_C$ for $Ir_{(1-x-z)}Ru_xRh_zO_y$ measured on 316 SS substrates. The shaded region depicts regions where nanoflake and nanoflake-like microstructure develops.

7.3.2 Summary and Conclusions

The $Ir_{(1-x-z)}Ru_xRh_zO_y$ system possesses many compositional regions which show excellent electrochemical performance; however, this is hindered by the simultaneous development of nanoflake microstructure in many of these zones. For an Ir-based electrode/microelectrode coating the $Ir_{(1-x-z)}Ru_xRh_zO_y$ system is not ideal due to the prevalence of the mechanically unfavorable nanoflake microstructure. Nonetheless many regions have been identified which do not develop nanoflake microstructure while still maintaining high electrochemical performance. These include a region where Ir has a slight majority in composition, an intermediate region where materials are well mixed, and two regions where Rh-content is dominant.

7.4 Ternary Metal Oxide Thin Films Summary and Conclusions

Several compositional regions in the ternary metal oxide systems were overlooked as a consequence of the gradient limits of the combinatorial method used. A few notable regions include the higher Ir content and higher Ru content regions for the $Ir_{(1-x-z)}Pd_xRu_zO_y$ system and the higher Ir-Rh and higher Rh content regions for the $Ir_{(1-x-z)}Pd_xRh_zO_y$ system. Nonetheless, the compositions that were investigated suggest that the ternary metal oxides can provide favorable microstructure and enhanced electrochemical properties over their single metal oxide endmembers. However, the compositional space where films possess favorable properties is considerably smaller for the $Ir_{(1-x-z)}Ru_xRh_zO_y$ system due to prolific nanoflake growth. This is contrasted by the much larger favorable compositional space in the ternary metal oxide systems which contain Pd. This tendency for the Pd-containing ternary metal oxide systems is owed to the fact that much lower solute concentrations are required to induce non-nanoflake growth. Thus, the presence of Pd is considered to be a key component for the enhancement of film properties for the ternary metal oxides. The compositional regions which outright suppress nanoflake microstructure have been identified and are provided in Table 7.1. As previously stated, these ranges are particularly sizable in systems which contain Pd due to its demonstrated ability to suppress nanoflake growth at comparatively lower solute concentrations.

Of the three ternary metal oxide systems investigated, the $Ir_{(1-x-z)}Pd_xRu_zO_y$ shows the most promise as an implantable neural interface coating due to its high electrochemical performance and desirable microstructure, this is followed by $Ir_{(1-x-z)}Pd_xRh_zO_y$ system for similar reasons, and least of all the $Ir_{(1-x-z)}Ru_xRh_zO_y$ system due to the prevalence of nanoflake growth over large compositional ranges. While not explicitly investigated, the CSC_C as a function of thickness for the ternary metal oxide films is likely to follow a similar trend to those observed in the binary metal oxide films. This assumption is based on the microstructural similarities observed between the binary and ternary metal oxide systems. However, it is uncertain whether the combination of three PGMs would further the enhance the electrochemical performance of films over the binary metal oxide systems.

Table 7.1

Non-Nanoflake Compositional Regions for $Ir_{(1\text{-}x\text{-}z)}M_xM'_zO_y$ [a]

Ternary System	Non-Nanoflake Regions
$Ir_{(1-x-z)}Pd_xRu_zO_y$	$x \geq 0.16$, $z \geq 0.05$
$Ir_{(1-x-z)}Pd_xRh_zO_y$	$x \geq 0.14$, $z \geq 0.04$
$Ir_{(1-x-z)}Ru_xRh_zO_y$	$x \geq 0.23$ or $z \geq 0.50$

[a] *Films synthesized at 20% OPP and 30mTorr WP*

Chapter 8

Summary, Future Work, and Concluding Remarks

8.1 Summary

In this thesis, four single metal PGM oxides, three binary metal oxide systems, and three ternary metal oxide systems were synthesized by reactive magnetron sputtering. Of the materials investigated, PdO and Rh_xO_y, as well as the binary and ternary metal oxide have not been previously considered or investigated for use as electrode coatings for implantable neural interface applications. Additionally, the synthesis of the binary and ternary metal oxides by reactive magnetron sputtering have never been reported.

All single metal oxide films demonstrated a qualitative increase in porosity and thereby an increase in the ESA when synthesized at higher WPs. These microstructural changes were confirmed by SEM, EIS, and was further supported by ECM. As a result, the electrochemical performance was considerably improved and was shown to have a strong thickness dependence. Thus, across all single metal oxide systems, synthesis at 30 mTorr WP and 20% OPP and lower power densities (≤ 4.9 W/cm^2) are considered to be the optimum synthesis parameters. Furthermore, preliminary cytotoxicity testing suggests that all single metal oxide materials are non-cytotoxic *in-vitro*. This is an important first step to fully assessing the biocompatibility of the materials. Among the single metal oxides investigated, the RuO_x, IrO_x, Rh_xO_y, and PdO were the highest to lowest performing electrochemically as measured by their CSC_C and impedance.

The use of the combinatorial sputtering method allowed for the rapid synthesis of hundreds of compositions of materials between the binary and ternary metal oxides from only a handful of depositions. The compositional ranges in which suppressed nanoflake growth in the binary and ternary metal oxide solid solutions were identified. It is believed these values are related to the solubility limits of the alloying metals and thereby the transition from a primary to an intermediary solid solution. Regardless of the underlying mechanism behind nanoflake suppression, the films were found to have exceptional electrochemical properties and favorable microstructures. Film thickness was shown to have a greater influence on electrochemical performance than their single metal oxide endmembers. As a result, the binary metal oxide films had to be grown at thicknesses generally ≥ 750 nm in order to outperform their single metal oxide endmembers. Among the binary metal oxides investigated, it is determined that due to the lower concentration of solute needed to suppress nanoflake microstructure while still maintaining high electrochemical performance, the $Ir_{(1-x)}Pd_xO_y$ and $Ir_{(1-x)}Ru_xO_y$ systems show significant promise for implantable neural interfacing applications.

The ternary metal oxides add an additional degree of complexity over the binary metal oxide systems. Despite this, similar compositional ranges which suppress nanoflake growth while maintaining high electrochemical performance were identified, among the three systems the $Ir_{(1-x-z)}Pd_xRu_zO_y$ and the $Ir_{(1-x-z)}Pd_xRh_zO_y$, and $Ir_{(1-x-z)}Ru_xRh_zO_y$ are more favored due to their near complete suppression of nanoflake microstructure over a sizeable range of compositions analyzed.

8.2 Future Work

A considerable amount of research was performed in the investigation of the PGM oxides and their mixtures. Despite the scope of the research performed, there is much more to be done. Fortunately, this thesis provides a strong foundation to move forward in many directions. This research demonstrated that viability of many newly investigated and developed PGM oxide materials for neural interfacing applications synthesized over a large parameter space. To this end, the following sections provide several routes to further investigate these materials.

8.2.1 Microelectrode Development

Ultimately the goal for the materials investigated in this thesis is to use them as neural interface electrode/microelectrode coatings to enhance charge exchange between the electrode-tissue interface. To this end the oxides investigated in this thesis must still be investigated for use on microelectrodes. In order to fully demonstrate the viability as implantable neural interface coatings it is critical to develop industrially relevant microelectrode and microelectrode arrays to fully test the feasibility of these materials.

8.2.2 Biocompatibility Testing

The research presented in this thesis would benefit from further biocompatibility testing. This could come in several forms. The first is an *in-vitro* fibroblast study in order to understand how the body may heal around an electrode coated with the many newly investigated and developed materials presented in this thesis. The second is pulse testing at biologically relevant pulse widths and intensities, as well as recording of relevant tissues and cells *in-vitro*. The final phase would be *in-vivo* testing of the materials from both a cytotoxic perspective as well as a from a functional device aspect, effectively a combination of phases one and two *in-vivo*.

8.2.3 Ternary Metal Oxide Thickness Dependence

The compositional ranges of the ternary metal oxides which suppress nanoflake growth with high CSC have been identified. It is this author opinion however that the ternary metal oxides are largely redundant. Nonetheless, in order to fully compare the single, binary, and ternary metal oxides, additional depositions are recommended to study the thickness dependence of the ternary metal oxides.

8.3 Concluding Remarks

As standalone oxides, the IrO_x and RuO_x systems are the most viable while the Rh_xO_y and PdO are least viable for neural interfacing applications based on electrochemical performance and ignoring the presence of nanoflake microstructure. However, the viability of the materials does change when considering the binary and ternary metal oxide systems. This is especially the case for the comparatively low performing PdO, which becomes pivotal in suppressing nanoflake growth in the binary and ternary metal oxide systems while maintaining high electrochemical performance. As a consequence, Pd is an invaluable alloying metal for the development of the binary and ternary metal oxide electrode coatings. RuO_x and $Ir_{(1-x)}Ru_xO_y$ had the highest electrochemical performance for the single and binary metal oxides, respectively. The performance in addition to the desirable microstructural characteristics demonstrates these materials are worthwhile further investigating.

Until this moment the cost of materials has been excluded from any discussion in this thesis. However, from a scalability standpoint it should be noted that the cost of Rh metal is substantially greater than the other three precursor PGMs (186). Considering the electrochemical performance of Rh_xO_y as a standalone single metal oxide, and the high concentrations required to suppress nanoflake growth in the binary and ternary metal oxides, along with its cost, the Rh_xO_y and Rh containing binary and ternary metal oxide systems are considered to be the least viable materials for use an electrode/microelectrode coating for implantable neural interfacing applications.

From an industrial and scalability standpoint, the oxide materials can be synthesized by reactive magnetron sputtering by many different magnetron configurations. The magnetron configuration utilized is normally dependent upon the geometry of the electrode. For instance, planar electrodes can be coated using high throughput planar (187,188) and cylindrical rotating cathode systems (189,190). More complicated geometries such as a stent electrode can be coated with a hollow cathode system (191,192).

References

1. Printable Periodic Table [Internet]. Chemistry Nexus. 2012 [cited 2021 Apr 11]. Available from: https://www.webelements.com/nexus/printable-periodic-table/

2. Matthey J. Relativistic Phenomena in the Chemistry of the Platinum Group Metals [Internet]. Johnson Matthey Technology Review. [cited 2021 Apr 11]. Available from: https://www.technology.matthey.com/article/44/4/146-155/

3. Hoffman DC, Lee DM. Chemistry of the Heaviest Elements- One Atom at a Time. J Chem Educ. 1999 Mar 1;76(3):331.

4. William Smith, Hashemi Javad. Foundations of Materials Science and Engineering. 6th ed. McGraw Hill; 2019. 139–140 p.

5. Takadoum J. Materials and Surface Engineering in Tribology. Wiley;

6. Sree H. Principles of Vapor Deposition of Thin Films [Internet]. Elsevier; 2006 [cited 2021 Apr 23]. Available from: https://linkinghub.elsevier.com/retrieve/pii/B9780080446998X50001

7. Milton Ohring. Materials Science of Thin Films Deposition & Structure. 2nd ed. Academic Press; 2020. 791 p.

8. Thornton JA. Structure-Zone Models Of Thin Films. In: Modeling of Optical Thin Films [Internet]. International Society for Optics and Photonics; 1988 [cited 2020 May 22]. p. 95–105. Available from: https://www.spiedigitallibrary.org/conference-proceedings-of-spie/0821/0000/Structure-Zone-Models-Of-Thin-Films/10.1117/12.941846.short

9. Allen J. Bard and Larry R. Faulkner, Electrochemical Methods: Fundamentals and Applications, New York: Wiley, 2001, 2nd ed. Russian Journal of Electrochemistry. 2002 Dec 1;38(12):1364–5.

10. Cyclic Voltammetry Explained: Basic Principles & Set Up [Internet]. Ossila. [cited 2021 Apr 21]. Available from: https://www.ossila.com/pages/cyclic-voltammetry

11. ARMICRON. English: Bragg Diffraction Planes [Internet]. 2010 [cited 2021 Apr 22]. Available from: https://commons.wikimedia.org/wiki/File:Bragg_diffraction.svg

12. Birkholz M, Fewster PF, Genzel C. Thin film analysis by X-ray scattering. Weinheim: Wiley-VCH; 2006. 356 p.

13. D01 Committee. Test Methods for Measuring Adhesion by Tape Test [Internet]. ASTM International; [cited 2021 Apr 22]. Available from: http://www.astm.org/cgi-bin/resolver.cgi?D3359-09

14. Shining Light on Sulfide Perovskites: LaYS3 Material Properties and Solar Cells | Chemistry of Materials [Internet]. [cited 2021 Jun 8]. Available from: https://pubs.acs.org/doi/10.1021/acs.chemmater.9b00478

15. Perovskite Oxide Based Materials for Energy and Environment-Oriented Photocatalysis | ACS Catalysis [Internet]. [cited 2021 Jun 8]. Available from: https://pubs.acs.org/doi/10.1021/acscatal.0c02947

16. Radovic M, Barsoum MW. MAX phases: Bridging the gap between metals and ceramics. MAX phases. 92(3):8.

17. Gonzalez-Julian J. Processing of MAX phases: From synthesis to applications. Journal of the American Ceramic Society. 2021;104(2):659–90.

18. Barsoum M, El-Raghy T. The MAX Phases: Unique new Carbide and Nitride Materials. American Scientist - AMER SCI. 2001 Jan 1;89.

19. Towards the computational design of solid catalysts | Nature Chemistry [Internet]. [cited 2021 Jun 8]. Available from: https://www.nature.com/articles/nchem.121

20. Fu Y, Poizeau S, Bertei A, Qi C, Mohanram A, Pietras JD, et al. Heterogeneous electrocatalysis in porous cathodes of solid oxide fuel cells. Electrochimica Acta. 2015 Mar;159:71–80.

21. Pancrazio JJ, Deku F, Ghazavi A, Stiller AM, Rihani R, Frewin CL, et al. Thinking Small: Progress on Microscale Neurostimulation Technology. Neuromodulation. 2017 Dec;20(8):745–52.

22. Cogan SF, Ehrlich J, Plante TD, Smirnov A, Shire DB, Gingerich M, et al. Sputtered iridium oxide films (SIROFs) for neural stimulation electrodes. Conference proceedings : . Annual International Conference of the IEEE Engineering in Medicine and Biology Society IEEE Engineering in Medicine and Biology Society Conference. 2004;6:4153.

23. Graphene active sensor arrays for long-term and wireless mapping of wide frequency band epicortical brain activity | Nature Communications [Internet]. [cited 2021 Apr 29]. Available from: https://www.nature.com/articles/s41467-020-20546-w

24. Alkawadri R. Brain–Computer Interface (BCI) Applications in Mapping of Epileptic Brain Networks Based on Intracranial-EEG: An Update. Front Neurosci [Internet]. 2019 [cited 2021 Apr 29];13. Available from: https://www.frontiersin.org/articles/10.3389/fnins.2019.00191/full

25. Bourrier A. Graphene bioelectronics for long term neuronal interfacing in-vivo. :199.

26. Kemnitz J, Winter J, Vester EG, Peters J. Transcutaneous cardiac pacing in patients with automatic implantable cardioverter defibrillators and epicardial patch electrodes. Anesthesiology. 1992 Aug;77(2):258–62.

27. Mulpuru SK, Madhavan M, McLeod CJ, Cha Y-M, Friedman PA. Cardiac Pacemakers: Function, Troubleshooting, and Management: Part 1 of a 2-Part Series. J Am Coll Cardiol. 2017 Jan 17;69(2):189–210.

28. Schaldach M, Hubmann M, Hardt R, Weikl A. [Titanium nitride cardiac pacemaker electrodes]. Biomed Tech (Berl). 1989 Aug;34(7–8):185–90.

29. Stevenson I, Voskoboinik A. Cardiac rhythm management devices. Aust J Gen Pract. 2018 May;47(5):264–71.

30. Ouyang H, Liu Z, Li N, Shi B, Zou Y, Xie F, et al. Symbiotic cardiac pacemaker. Nature Communications. 2019 Apr 23;10(1):1821.

31. Sánchez G, Dalchiele E, Alles A. Electrical characterization of titanium nitride surfaces for pacing electrodes. Journal of Materials Science. 2006 Jun 1;41:3241–7.

32. Sunny TD, Aparna T, Neethu P, Venkateswaran J, Vishnupriya V, Vyas PS. Robotic Arm with Brain – Computer Interfacing. Procedia Technology. 2016 Jan 1;24:1089–96.

33. Lebedev MA, Nicolelis MAL. Brain-machine interfaces: past, present and future. Trends Neurosci. 2006 Sep;29(9):536–46.

34. Musk E, Neuralink. An Integrated Brain-Machine Interface Platform With Thousands of Channels. Journal of medical Internet research. 2019;21(10):e16194.

35. Collinger JL, Foldes S, Bruns TM, Wodlinger B, Gaunt R, Weber DJ. Neuroprosthetic technology for individuals with spinal cord injury. J Spinal Cord Med. 2013 Jul;36(4):258–72.

36. Bradberry TJ, Gentili RJ, Contreras-Vidal JL. Reconstructing Three-Dimensional Hand Movements from Noninvasive Electroencephalographic Signals. J Neurosci. 2010 Mar 3;30(9):3432–7.

37. Deer TR, Mekhail N, Provenzano D, Pope J, Krames E, Leong M, et al. The Appropriate Use of Neurostimulation of the Spinal Cord and Peripheral Nervous System for the Treatment of Chronic Pain and Ischemic Diseases: The Neuromodulation Appropriateness Consensus Committee. Neuromodulation: Technology at the Neural Interface. 2014;17(6):515–50.

38. Barolat G. Chapter 27 - Spinal Cord Stimulation for Painful Neuropathies. In: Krames ES, Peckham PH, Rezai AR, editors. Neuromodulation [Internet]. San Diego: Academic Press; 2009 [cited 2020 Apr 24]. p. 377–84. Available from: http://www.sciencedirect.com/science/article/pii/B9780123742483000288

39. Eldabe S, Buchser E, Duarte RV. Complications of Spinal Cord Stimulation and Peripheral Nerve Stimulation Techniques: A Review of the Literature. Pain Med. 2016 Feb;17(2):325–36.

40. Epstein LJ, Palmieri M. Managing chronic pain with spinal cord stimulation. Mt Sinai J Med. 2012 Feb;79(1):123–32.

41. Benabid AL. Deep brain stimulation for Parkinson’s disease. Current Opinion in Neurobiology. 2003 Dec 1;13(6):696–706.

42. Akhtar H, Bukhari F, Nazir M, Anwar MN, Shahzad A. Therapeutic Efficacy of Neurostimulation for Depression: Techniques, Current Modalities, and Future Challenges. Neurosci Bull. 2016 Jan 19;32(1):115–26.

43. Delaloye S, Holtzheimer PE. Deep brain stimulation in the treatment of depression. Dialogues Clin Neurosci. 2014 Mar;16(1):83–91.

44. Flora ED, Perera CL, Cameron AL, Maddern GJ. Deep brain stimulation for essential tremor: A systematic review. Movement Disorders. 2010;25(11):1550–9.

45. Davis P, Gaitanis J. Neuromodulation for the Treatment of Epilepsy: A Review of Current Approaches and Future Directions. Clin Ther. 2020 Jul;42(7):1140–54.

46. Smith JR, Fountas K, Murro AM, Park YD, Jenkins PD, Greene DA, et al. Closed-Loop Stimulation in the Control of Focal Epilepsy. Neuromodulation. 2009 Dec 1;657–62.

47. Vonck K, Herdt V de, Sprengers M, Ben-Menachem E. Chapter 58 - Neurostimulation for epilepsy. In: Stefan H, Theodore WH, editors. Handbook of Clinical Neurology [Internet]. Elsevier; 2012 [cited 2020 Apr 24]. p. 955–70. (Epilepsy; vol. 108). Available from: http://www.sciencedirect.com/science/article/pii/B978044452899500040X

48. Wang C, Brunton E, Haghgooie S, Cassells K, Lowery A, Rajan R. Characteristics of electrode impedance and stimulation efficacy of a chronic cortical implant using novel annulus electrodes in rat motor cortex. J Neural Eng. 2013 Aug;10(4):046010.

49. Normann RA, Greger BA, House P, Romero SF, Pelayo F, Fernandez E. Toward the development of a cortically based visual neuroprosthesis. J Neural Eng. 2009 Jun;6(3):035001.

50. Thanos S, Heiduschka P, Stupp T. Implantable visual prostheses. In: Sakas DE, Simpson BA, editors. Operative Neuromodulation: Volume 2: Neural Networks Surgery [Internet]. Vienna: Springer; 2007 [cited 2020 Dec 19]. p. 465–72. (Acta Neurochirurgica Supplements). Available from: https://doi.org/10.1007/978-3-211-33081-4_53

51. Shepherd RK, Shivdasani MN, Nayagam DAX, Williams CE, Blamey PJ. Visual prostheses for the blind. Trends Biotechnol. 2013 Oct;31(10):562–71.

52. Wellman SM, Eles JR, Ludwig KA, Seymour JP, Michelson NJ, McFadden WE, et al. A Materials Roadmap to Functional Neural Interface Design. Adv Funct Mater [Internet]. 2018 Mar 21 [cited 2020 Apr 24];28(12). Available from: https://www.ncbi.nlm.nih.gov/pmc/articles/PMC5963731/

53. Geddes LA, Roeder R. Criteria for the Selection of Materials for Implanted Electrodes. Annals of Biomedical Engineering. 2003 Jul 1;31(7):879–90.

54. Dee KC, Puleo DA, Bizios R. An Introduction to Tissue-Biomaterial Interactions. John Wiley & Sons; 2003. 251 p.

55. Ratner B. Biomaterials Science, Second Edition: An Introduction to Materials in Medicine. Vol. xii. 2003.

56. Sillay KA, Ondoma S, Wingeier B, Schomberg D, Sharma P, Kumar R, et al. Long-Term Surface Electrode Impedance Recordings Associated with Gliosis for a Closed-Loop Neurostimulation Device. Ann Neurosci. 2018 Dec;25(4):289–98.

57. Paasche G, Tasche C, Stöver T, Lesinski-Schiedat A, Lenarz T. The Long-Term Effects of Modified Electrode Surfaces and Intracochlear Corticosteroids on Postoperative Impedances in Cochlear Implant Patients. Otology & Neurotology. 2009 Aug;30(5):592–8.

58. Zhang K, Bhatia S, Oh MY, Cohen D, Angle C, Whiting D. Long-term results of thalamic deep brain stimulation for essential tremor: Clinical article. Journal of Neurosurgery. 2010 Jun 1;112(6):1271–6.

59. Wang Y, Vaddiraju S, Gu B, Papadimitrakopoulos F, Burgess DJ. Foreign Body Reaction to Implantable Biosensors: Effects of Tissue Trauma and Implant Size. J Diabetes Sci Technol. 2015 Aug 25;9(5):966–77.

60. Sheikh Z, Brooks PJ, Barzilay O, Fine N, Glogauer M. Macrophages, Foreign Body Giant Cells and Their Response to Implantable Biomaterials. Materials (Basel). 2015 Aug 28;8(9):5671–701.

61. Horie M, Nishio K, Fujita K, Endoh S, Miyauchi A, Saito Y, et al. Protein adsorption of ultrafine metal oxide and its influence on cytotoxicity toward cultured cells. Chem Res Toxicol. 2009 Mar 16;22(3):543–53.

62. Aronson S, Geddes LA. Electrode potential stability. IEEE Trans Biomed Eng. 1985 Nov;32(11):987–8.

63. Ragheb T, Geddes LA. The polarization impedance of common electrode metals operated at low current density. Ann Biomed Eng. 1991 Mar 1;19(2):151–63.

64. Boehler C, Carli S, Fadiga L, Stieglitz T, Asplund M. Tutorial: guidelines for standardized performance tests for electrodes intended for neural interfaces and bioelectronics. Nature Protocols. 2020 Nov;15(11):3557–78.

65. Chapman CAR, Chen H, Stamou M, Biener J, Biener MM, Lein PJ, et al. Nanoporous gold as a neural interface coating: effects of topography, surface chemistry, and feature size. ACS Appl Mater Interfaces. 2015 Apr 8;7(13):7093–100.

66. Vafaiee M, Vossoughi M, Mohammadpour R, Sasanpour P. Gold-Plated Electrode with High Scratch Strength for Electrophysiological Recordings. Scientific Reports. 2019 Feb 27;9(1):2985.

67. Cui H, Xie X, Xu S, Chan LLH, Hu Y. Electrochemical characteristics of microelectrode designed for electrical stimulation. BioMedical Engineering OnLine. 2019 Aug 1;18(1):86.

68. Harris AR, Newbold C, Carter P, Cowan R, Wallace GG. Measuring the effective area and charge density of platinum electrodes for bionic devices. J Neural Eng. 2018 Aug 1;15(4):046015.

69. Kumsa D, Bhadra N, Hudak E, Kelley S, Untereker D, Mortimer J. Electron transfer processes occurring on platinum neural stimulating electrodes: a tutorial on the i (V e) profile. Journal of Neural Engineering. 2016 Oct 1;13:052001.

70. Harris AR, Newbold C, Carter P, Cowan R, Wallace GG. Using Chronopotentiometry to Better Characterize the Charge Injection Mechanisms of Platinum Electrodes Used in Bionic Devices. Front Neurosci. 2019 Apr 24;13:380.

71. Johnson MD, Langhals NB, Kipke DR. Neural Interface Dynamics Following Insertion of Hydrous Iridium Oxide Microelectrode Arrays. In: 2006 International Conference of the IEEE Engineering in Medicine and Biology Society. 2006. p. 3178–81.

72. Ereifej ES, Khan S, Newaz G, Zhang J, Auner GW, VandeVord PJ. Comparative assessment of iridium oxide and platinum alloy wires using an in vitro glial scar assay. Biomed Microdevices. 2013 Dec;15(6):917–24.

73. Cassar IR, Yu C, Sambangi J, Lee CD, Whalen JJ, Petrossians A, et al. Electrodeposited platinum-iridium coating improves in vivo recording performance of chronically implanted microelectrode arrays. Biomaterials. 2019 Jun;205:120–32.

74. Dymond AM, Kaechele LE, Jurist JM, Crandall PH. Brain tissue reaction to some chronically implanted metals. J Neurosurg. 1970 Nov;33(5):574–80.

75. Phagocytic and metabolic reactions to chronically implanted metal brain electrodes - ScienceDirect [Internet]. [cited 2020 Apr 24]. Available from: https://www.sciencedirect.com/science/article/pii/0014488684901791

76. Gulino M, Kim D, Pané S, Santos SD, Pêgo AP. Tissue Response to Neural Implants: The Use of Model Systems Toward New Design Solutions of Implantable Microelectrodes. Front Neurosci [Internet]. 2019 [cited 2021 Apr 29];13. Available from: https://www.frontiersin.org/articles/10.3389/fnins.2019.00689/full

77. Shepherd RK, Carter PM, Dalrymple AN, Enke YL, Wise AK, Nguyen T, et al. Platinum dissolution and tissue response following long-term electrical stimulation at high charge densities. J Neural Eng. 2021 Apr 1;18(3):036021.

78. Cogan SF. Neural stimulation and recording electrodes. Annu Rev Biomed Eng. 2008;10:275–309.

79. Grdeń M, Łukaszewski M, Jerkiewicz G, Czerwiński A. Electrochemical behaviour of palladium electrode: Oxidation, electrodissolution and ionic adsorption. Electrochimica Acta. 2008 Nov 1;53(26):7583–98.

80. Gross G. Multielectrode arrays. Scholarpedia. 2011 Jan 1;6:5749.

81. Göbbels K, Kuenzel T, van Ooyen A, Baumgartner W, Schnakenberg U, Bräunig P. Neuronal cell growth on iridium oxide. Biomaterials. 2010 Feb;31(6):1055–67.

82. Kim YH, Kim GH, Baek NS, Han YH, Kim A-Y, Chung M-A, et al. Fabrication of multi-electrode array platforms for neuronal interfacing with bi-layer lift-off resist sputter deposition. J Micromech Microeng. 2013 Aug;23(9):097001.

83. Merrill DR, Bikson M, Jefferys JGR. Electrical stimulation of excitable tissue: design of efficacious and safe protocols. Journal of Neuroscience Methods. 2005;28.

84. Cogan SF, Ludwig KA, Welle CG, Takmakov P. Tissue damage thresholds during therapeutic electrical stimulation. J Neural Eng. 2016 Apr;13(2):021001.

85. Shannon RV. A model of safe levels for electrical stimulation. IEEE Trans Biomed Eng. 1992 Apr;39(4):424–6.

86. Chen Y-M, Chung T-W, Wu P-W, Chen P-C. A cost-effective fabrication of iridium oxide films as biocompatible electrostimulation electrodes for neural interface applications. Journal of Alloys and Compounds. 2017 Jan 25;692:339–45.

87. Jang H, Lee J. Iridium oxide fabrication and application: A review. Journal of Energy Chemistry. 2020 Jul 1;46:152–72.

88. Chen P-C, Chen Y-C, Huang C-N. Free-standing iridium oxide nanotube array for neural interface electrode applications. Materials Letters. 2018 Jun 15;221:293–5.

89. Amini S, Hettinger JD, Taylor G. Thin Film Coating [Internet]. 2020 [cited 2020 Dec 19]. Available from: https://patentscope.wipo.int/search/en/detail.jsf?docId=WO2020240193&tab=PCTBIBLIO&_cid=P22-KI9023-43389-1

90. Atmaramani R, Chakraborty B, Rihani RT, Usoro J, Hammack A, Abbott J, et al. Ruthenium oxide based microelectrode arrays for in vitro and in vivo neural recording and stimulation. Acta Biomaterialia. 2020 Jan 1;101:565–74.

91. Burdett C. Characterization of Ruthenium Electrodes for Implantable Neurostimulation Applications. :2.

92. Leber M, Bhandari R, Mize J, Warren DJ, Shandhi MMH, Solzbacher F, et al. Long term performance of porous platinum coated neural electrodes. Biomed Microdevices. 2017 Sep;19(3):62.

93. Kim R, Nam Y. Novel platinum black electroplating technique improving mechanical stability. Annu Int Conf IEEE Eng Med Biol Soc. 2013;2013:184–7.

94. Mandal HS, Kastee JS, McHail DG, Rubinson JF, Pancrazio JJ, Dumas TC. Improved Poly(3,4-Ethylenedioxythiophene) (PEDOT) for Neural Stimulation. Neuromodulation. 2015 Dec;18(8):657–63.

95. Fan L-Z, Maier J. High-performance polypyrrole electrode materials for redox supercapacitors. Electrochemistry Communications. 2006 Jun 1;8(6):937–40.

96. Tamm J, Alumaa A, Hallik A, Sammelselg V. Redox properties of polypyrrole bilayers. Electrochimica Acta. 2001 Aug 24;46(26):4105–12.

97. Guitchounts G, Markowitz JE, Liberti WA, Gardner TJ. A carbon-fiber electrode array for long-term neural recording. J Neural Eng. 2013 Aug;10(4):046016.

98. Melmer M, Stangler T, Premstaller A, Lindner W. Effects of the redox state of porous graphitic carbon on the retention of oligosaccharides. Journal of Chromatography A. 2010 Sep 24;1217(39):6097–101.

99. Marasine NR, Sankhi S, Lamichhane R, Marasini NR, Dangi NB. Self-Reported Antidepressant Drug Side Effects, Medication Adherence, and Its Associated Factors among Patients Diagnosed with Depression at the Psychiatric Hospital of Nepal. Depress Res Treat [Internet]. 2020 Oct 17 [cited 2021 Mar 26];2020. Available from: https://www.ncbi.nlm.nih.gov/pmc/articles/PMC7593732/

100. Cartwright C, Gibson K, Read J, Cowan O, Dehar T. Long-term antidepressant use: patient perspectives of benefits and adverse effects. Patient Prefer Adherence. 2016 Jul 28;10:1401–7.

101. Baldini A, Von Korff M, Lin EHB. A Review of Potential Adverse Effects of Long-Term Opioid Therapy: A Practitioner's Guide. Prim Care Companion CNS Disord [Internet]. 2012 [cited 2021 Mar 26];14(3). Available from: https://www.ncbi.nlm.nih.gov/pmc/articles/PMC3466038/

102. Cascade E, Kalali AH, Kennedy SH. Real-World Data on SSRI Antidepressant Side Effects. Psychiatry (Edgmont). 2009 Feb;6(2):16–8.

103. Ferguson JM. SSRI Antidepressant Medications: Adverse Effects and Tolerability. Prim Care Companion J Clin Psychiatry. 2001 Feb;3(1):22–7.

104. Kang K, Shay J. Blue sputtered iridium oxide films (blue SIROF's). Electrochemical Society. 1983;30:766–9.

105. Klein JD, Clauson SL, Cogan SF. Morphology and charge capacity of sputtered iridium oxide films. Journal of Vacuum Science & Technology A. 1989 Sep 1;7(5):3043–7.

106. Meyer RD, Cogan SF, Nguyen TH, Rauh RD. Electrodeposited iridium oxide for neural stimulation and recording electrodes. IEEE Trans Neural Syst Rehabil Eng. 2001 Mar;9(1):2–11.

107. Robblee L, Mangaudis M, Lasinksky E, Kimball A, Brummer S. Charge injection properties of thermally-prepared iridium oxide films. Materials Research Society Symposium Proceedings. 1986;(56):303–10.

108. Fierro S, Kapałka A, Comninellis C. Electrochemical comparison between IrO2 prepared by thermal treatment of iridium metal and IrO2 prepared by thermal decomposition of H2IrCl6 solution. Electrochemistry Communications. 2010 Jan 1;12(1):172–4.

109. Wessling B, Mokwa W, Schnakenberg U. RF-sputtering of iridium oxide to be used as stimulation material in functional medical implants. J Micromech Microeng. 2006 May;16(6):S142–8.

110. Maeng J, Chakraborty B, Geramifard N, Kang T, Rihani RT, Joshi-Imre A, et al. High-charge-capacity sputtered iridium oxide neural stimulation electrodes deposited using water vapor as a reactive plasma constituent. Journal of Biomedical Materials Research Part B: Applied Biomaterials. 2020;108(3):880–91.

111. Negi S, Bhandari R, Rieth L, Solzbacher F. Effect of sputtering pressure on pulsed-DC sputtered iridium oxide films. Sensors and Actuators B: Chemical. 2009 Mar 28;137(1):370–8.

112. Eshraghi AA, Nazarian R, Telischi FF, Rajguru SM, Truy E, Gupta C. The cochlear implant: Historical aspects and future prospects. Anat Rec (Hoboken). 2012 Nov;295(11):1967–80.

113. Wessling B. Sputter deposition of Iridium and Iridium Oxide for stimulation electrode coatings. 2007 [cited 2020 Jun 10]; Available from: https://core.ac.uk/display/36429124

114. Liu D-Q, Yu S-H, Son S-W, Joo S-K. Electrochemical Performance of Iridium Oxide Thin Film for Supercapacitor Prepared by Radio Frequency Magnetron Sputtering Method. ECS Transactions. 2008 Dec 17;16.

115. Matthey J. Platinum Group Metals Technology [Internet]. Johnson Matthey Technology Review. [cited 2021 Apr 11]. Available from: https://www.technology.matthey.com/article/33/1/21-23/

116. Lanthanide Contraction [Internet]. Chemistry LibreTexts. 2013 [cited 2021 Apr 11]. Available from: https://chem.libretexts.org/Bookshelves/Inorganic_Chemistry/Modules_and_Websites_(Inorganic_Chemistry)/Descriptive_Chemistry/Elements_Organized_by_Block/4_f-Block_Elements/The_Lanthanides/aLanthanides%3A_Properties_and_Reactions/Lanthanide_Contraction

117. Chapter 2_PGM_Guide.pdf [Internet]. [cited 2021 Apr 29]. Available from: https://ipa-news.com/assets/sustainability/IPA_Guidance/Chapter%202_PGM_Guide.pdf

118. Renner H, Schlamp G, Kleinwächter I, Drost E, Lüschow HM, Tews P, et al. Platinum Group Metals and Compounds. In: Ullmann's Encyclopedia of Industrial Chemistry [Internet]. American Cancer Society; 2001 [cited 2020 Apr 24]. Available from: https://onlinelibrary.wiley.com/doi/abs/10.1002/14356007.a21_075

119. Seehra MS, Bristow AD. Introductory Chapter: Overview of the Properties and Applications of Noble and Precious Metals. Noble and Precious Metals - Properties, Nanoscale Effects and Applications [Internet]. 2018 Jul 4 [cited 2021 Apr 11]; Available from: https://www.intechopen.com/books/noble-and-precious-metals-properties-nanoscale-effects-and-applications/introductory-chapter-overview-of-the-properties-and-applications-of-noble-and-precious-metals

120. 25_applications_of_pgms_ipa_fact_sheet_final.pdf [Internet]. [cited 2021 Apr 12]. Available from: https://ipa-news.de/assets/applications/25_applications_of_pgms_ipa_fact_sheet_final.pdf

121. Shuang H, Chen H, Wu F, Li J, Cheng C, Li H, et al. Catalytic dehydrogenation of hydrogen-rich liquid organic hydrogen carriers by palladium oxide supported on activated carbon. Fuel. 2020 Sep 1;275:117896.

122. Ullah N, Omanovic S. Large charge-storage-capacity iridium/ruthenium oxide coatings as promising material for neural stimulating electrodes. Materials Chemistry and Physics. 2015 Jun 1;159:119–27.

123. Lashgari M, Matloubi D. Atomistic understanding of hydrogen loading phenomenon into palladium cathode: A simple nanocluster approach and electrochemical evidence. J Chem Sci. 2015 Mar;127(3):575–81.

124. Osmium | Os (Element) - PubChem [Internet]. [cited 2021 Apr 29]. Available from: https://pubchem.ncbi.nlm.nih.gov/element/Osmium#section=Atomic-Mass-Half-Life-and-Decay

125. Alfonso E, Olaya J, Cubillos G. Thin Film Growth Through Sputtering Technique and Its Applications. Science and Technology. :37.

126. Baptista A, Silva F, Porteiro J, Míguez J, Pinto G. Sputtering Physical Vapour Deposition (PVD) Coatings: A Critical Review on Process Improvement and Market Trend Demands. Coatings. 2018 Nov;8(11):402.

127. Group TM. Optical Coatings Technology [Internet]. [cited 2021 Apr 29]. Available from: https://www.techbriefs.com/component/content/article/tb/supplements/pit/features/applications/35160

128. Rossnagel SM. Sputter deposition for semiconductor manufacturing. IBM Journal of Research and Development. 1999 Jan;43(1.2):163–79.

129. Das A, Ko DH, Chen C-H, Chang L-B, Lai C-S, Chu F-C, et al. Highly sensitive palladium oxide thin film extended gate FETs as pH sensor. Sensors and Actuators B: Chemical. 2014 Dec 15;205:199–205.

130. Jakob MH, Gutsch S, Chatelle C, Krishnaraja A, Fahlteich J, Weber W, et al. Flexible thin film pH sensor based on low-temperature atomic layer deposition. physica status solidi (RRL) – Rapid Research Letters. 2017;11(7):1700123.

131. Yang L, Ruan C, Li Y. Detection of viable Salmonella typhimurium by impedance measurement of electrode capacitance and medium resistance. Biosensors and Bioelectronics. 2003 Dec 30;19(5):495–502.

132. Matthey J. Platinum Group Metals and their Oxides in Semiconductor Photosensitisation [Internet]. Johnson Matthey Technology Review. [cited 2020 Apr 24]. Available from: https://www.technology.matthey.com/article/47/1/2-12/

133. Stevens JE, Lohn AJ, Decker SA, Doyle BL, Mickel PR, Marinella MJ. Reactive sputtering of substoichiometric Ta2Ox for resistive memory applications. Journal of Vacuum Science & Technology A. 2013 Nov 4;32(2):021501.

134. Laughlin KR, Jamieson S, Pearson AC, Wang H, Vanfleet RR, Davis RC, et al. Thin-Film Carbon Nanofuses for Permanent Data Storage. ACS Omega. 2017 Jun 2;2(6):2432–8.

135. Slavcheva EP. Magnetron sputtered iridium oxide as anode catalyst for PEM hydrogen generation. Macedonian Journal of Chemistry and Chemical Engineering. 2011 Jun 15;30(1):45–54.

136. Gasda MD, Teki R, Lu T-M, Koratkar N, Eisman GA, Gall D. Sputter-Deposited Pt PEM Fuel Cell Electrodes: Particles vs Layers. J Electrochem Soc. 2009 Mar 24;156(5):B614.

137. Group TM. Sputter Deposition of Catalysts for Fuel-Cell Electrodes [Internet]. [cited 2021 Apr 29]. Available from: https://www.techbriefs.com/component/content/article/tb/pub/techbriefs/materials/29835

138. Mráz S, Schneider JM. Influence of the negative oxygen ions on the structure evolution of transition metal oxide thin films. Journal of Applied Physics. 2006 Jul 15;100(2):023503.

139. Bradley RM, Harper JME, Smith DA. Theory of thin-film orientation by ion bombardment during deposition. Journal of Applied Physics. 1986 Dec 15;60(12):4160–4.

140. Marinov M. Effect of ion bombardment on the initial stages of thin film growth. Thin Solid Films. 1977 Nov 1;46(3):267–74.

141. Grigorov GI, Grigorov KG, Sporken R, Caudano R. Ion-induced densification of pvd films—a choice of the optimum density of ion bombardment. Appl Phys A. 1996 Oct 1;63(4):399–401.

142. Mahieu S, Leroy WP, Aeken KV, Depla D. Modeling the flux of high energy negative ions during reactive magnetron sputtering. Journal of Applied Physics. 2009 Nov 4;106(9):093302.

143. Dodd R, You S, Bryant PM, Bradley JW. Negative Ion Density Measurements in Reactive Magnetron Sputtering. Plasma Processes and Polymers. 2009;6(S1):S615–9.

144. Kim D, Jang J, Yoon S, Hong M. Effects of bombardment of negative oxygen ions on amorphous indium gallium zinc oxide thin films by superimposed rf/dc magnetron sputtering. Appl Phys Express. 2014 Mar 7;7(3):031401.

145. Bikowski A, Welzel T, Ellmer K. The impact of negative oxygen ion bombardment on electronic and structural properties of magnetron sputtered ZnO:Al films. Applied Physics Letters. 2013 Jun 1;102:242106.

146. Dulmaa A, Vrielinck H, Khelifi S, Depla D. Sputter deposition of copper oxide films. Applied Surface Science. 2019 Oct 30;492:711–7.

147. Chason E, Karlson M, Colin JJ, Magnfält D, Sarakinos K, Abadias G. A kinetic model for stress generation in thin films grown from energetic vapor fluxes. Journal of Applied Physics. 2016 Apr 13;119(14):145307.

148. Depla D, De Gryse R. Target poisoning during reactive magnetron sputtering: Part II: the influence of chemisorption and gettering. Surface and Coatings Technology. 2004 May 24;183(2):190–5.

149. Belkind A, Zhao Z, Hoboken NJ, Carter D, Mahoney L, McDonough G, et al. Pulsed-DC reactive sputtering of dielectrics: Pulsing parameter effects. Proceedings of the SVC 43th Annual Technical Conference. 2000 Jan 1;86–90.

150. Arnell RD, Kelly PJ, Bradley JW. Recent developments in pulsed magnetron sputtering. Surface and Coatings Technology. 2004 Nov 1;188–189:158–63.

151. Ludwig A. Discovery of new materials using combinatorial synthesis and high-throughput characterization of thin-film materials libraries combined with computational methods. npj Computational Materials. 2019 Jul 10;5(1):1–7.

152. Nagata T. (Invited) Development of New High-Dielectric Constant Thin Films By Combinatorial Synthesis. ECS Trans. 2020 Apr 24;97(1):61.

153. Deng YP, Guan YF, Fowlkes JD, Wen SQ, Liu FX, Pharr GM, et al. A combinatorial thin film sputtering approach for synthesizing and characterizing ternary ZrCuAl metallic glasses. Intermetallics. 2007 Sep 1;15(9):1208–16.

154. Scabarozi T, Gennaoui C, Roche J, Flemming T, Wittenberger K, Hann P, et al. Combinatorial investigation of (Ti1−xNbx)2AlC. 2009;

155. Yu J-S, Kim M-S, Kim JH. Combinatorial discovery of new methanol-tolerant non-noble metal cathode electrocatalysts for direct methanol fuel cells. Phys Chem Chem Phys. 2010 Nov 16;12(46):15274–81.

156. Lu J, Lee CG. Numerical estimates for energy of sputtered target atoms and reflected Ar neutrals in sputter processes. Vacuum. 2012 Feb 29;86(8):1134–40.

157. Basics of EIS: Electrochemical Research-Impedance [Internet]. [cited 2021 Jun 6]. Available from: https://www.gamry.com/application-notes/EIS/basics-of-electrochemical-impedance-spectroscopy/

158. Introduction to Buffers [Internet]. Chemistry LibreTexts. 2017 [cited 2021 Apr 21]. Available from: https://chem.libretexts.org/Bookshelves/Physical_and_Theoretical_Chemistry_Textbook_Maps/Supplemental_Modules_(Physical_and_Theoretical_Chemistry)/Acids_and_Bases/Buffers/Introduction_to_Buffers

159. ICDD Database Search – ICDD [Internet]. [cited 2021 Jun 10]. Available from: https://www.icdd.com/pdfsearch/

160. Degen T, Sadki M, Bron E, König U, Nénert G. The HighScore suite. Powder Diffraction. 2014 Dec;29(S2):S13–8.

161. Nečas D, Klapetek P. Gwyddion: an open-source software for SPM data analysis. centr.eur.j.phys. 2012 Feb 1;10(1):181–8.

162. ISO 25178-2:2012(en), Geometrical product specifications (GPS) — Surface texture: Areal — Part 2: Terms, definitions and surface texture parameters [Internet]. [cited 2020 Nov 28]. Available from: https://www.iso.org/obp/ui/#iso:std:iso:25178:-2:ed-1:v1:en

163. Energy-Dispersive X-ray Spectroscopy (EDS) [Internet]. Chemistry LibreTexts. 2019 [cited 2021 Jun 7]. Available from: https://chem.libretexts.org/Courses/Franklin_and_Marshall_College/Introduction_to_Materials_Characterization__CHM_412_Collaborative_Text/Spectroscopy/Energy-Dispersive_X-ray_Spectroscopy_(EDS)

164. EDS Principle | West Campus Materials Characterization Core [Internet]. [cited 2021 Jun 7]. Available from: https://ywcmatsci.yale.edu/edx-principle

165. Moseley's Law - Explanation, Henry Moseley, Moseley's Experiment [Internet]. BYJUS. [cited 2021 Jun 7]. Available from: https://byjus.com/physics/moseleys-law/

166. ISO 10993-5:2009(en), Biological evaluation of medical devices — Part 5: Tests for in vitro cytotoxicity [Internet]. [cited 2020 Dec 20]. Available from: https://www.iso.org/obp/ui#iso:std:iso:10993:-5:ed-3:v1:en

167. Takasu Y, Sugimoto W, Nishiki Y, Nakamatsu S. Structural analyses of RuO2–TiO2/Ti and IrO2–RuO2–TiO2/Ti anodes used in industrial chlor-alkali membrane processes. Journal of Applied Electrochemistry. 2010 Oct 1;40.

168. Prouzet E. Multiple-scattering contribution in extended X-ray absorption fine structure for iridium oxide IrO2. J Phys: Condens Matter. 1995 Oct;7(41):8027–33.

169. Meyer H-J, Müller-Buschbaum HK. Eine neue durch oxidspuren stabilisierte form des palladiums. Journal of the Less Common Metals. 1980 Dec 1;76(1):293–8.

170. Waser J, Levy HA, Peterson SW. The structure of PdO. Acta Crystallographica. 1953;6(7):661–3.

171. Pueschel G. Beitrag zur Kenntnis des Systems Pd O H2 O. Zeitschrift für anorganische und allgemeine Chemie. 1955;281:44–53.

172. Aeken KV, Mahieu S, Depla D. The metal flux from a rotating cylindrical magnetron: a Monte Carlo simulation. J Phys D: Appl Phys. 2008 Oct;41(20):205307.

173. Depla D, Leroy WP. Magnetron sputter deposition as visualized by Monte Carlo modeling. Thin Solid Films. 2012 Aug 1;520(20):6337–54.

174. Hoffman DW, Thornton JA. The compressive stress transition in Al, V, Zr, Nb and W metal films sputtered at low working pressures. Thin Solid Films. 1977 Sep 1;45(2):387–96.

175. The impact of negative oxygen ion bombardment on electronic and structural properties of magnetron sputtered ZnO:Al films: Applied Physics Letters: Vol 102, No 24 [Internet]. [cited 2020 May 12]. Available from: https://aip.scitation.org/doi/10.1063/1.4811647

176. Xia J, Liang W, Miao Q, Depla D. The effect of energy and momentum transfer during magnetron sputter deposition of yttrium oxide thin films. Applied Surface Science. 2018 May 1;439:545–51.

177. Drese RJ, Wuttig M. Stress evolution during growth in direct-current-sputtered zinc oxide films at various oxygen flows. Journal of Applied Physics. 2005 Oct 1;98(7):073514.

178. Meng F, Ge F, Chen Y, Xu G, Huang F. Local structural changes induced by ion bombardment in magnetron sputtered ZnO: Al films: Raman, XPS, and XAS study. Surface and Coatings Technology. 2019 May 15;365:2–9.

179. Fairose S, Ernest S, Daniel S. Effect of Oxygen Sputter Pressure on the Structural, Morphological and Optical Properties of ZnO Thin Films for Gas Sensing Application. Sens Imaging [Internet]. 2018 [cited 2020 Jun 24];19(1). Available from: https://www.ncbi.nlm.nih.gov/pmc/articles/PMC5747580/

180. Patterson AL. The Scherrer Formula for X-Ray Particle Size Determination. Physical Review. 1939 Nov 1;56:978–82.

181. Zhang Z, Cserfalvi T, Gratzl M. pH dependent voltammetry at partially oxidized palladium and its potential for voltammetry-based pH sensing. Journal of Electroanalytical Chemistry. 2019 Jul 15;845:1–5.

182. Shannon RD, Prewitt C. Synthesis and structure of a new high pressure form of Rh2O3. Golden Book of Phase Transistions. 2002;

183. 23.9: Electrolysis of Water [Internet]. Chemistry LibreTexts. 2016 [cited 2021 May 1]. Available from: https://chem.libretexts.org/Bookshelves/Introductory_Chemistry/Book%3A_Introductory_Chemistry_(CK-12)/23%3A_Electrochemistry/23.09%3A_Electrolysis_of_Water

184. Callister W. Fundamentals of Materials Science and Engineering. 1st ed. Wiley; 2020.

185. Schmool D. Solid State Physics [Internet]. Bloomfield, UNITED STATES: Mercury Learning & Information; 2016 [cited 2021 Apr 27]. Available from: http://ebookcentral.proquest.com/lib/rowan/detail.action?docID=4895124

186. Price tables - PMM [Internet]. [cited 2020 Dec 19]. Available from: http://www.platinum.matthey.com/prices/price-tables

187. Benefits of Planar Cathode Placement During Sputtering [Internet]. Denton Vacuum. 2019 [cited 2021 May 31]. Available from: https://www.dentonvacuum.com/benefits-of-planar-cathode-placement-during-sputtering/

188. Magnetron – Angstrom Science Linear Sputtering Magnetron [Internet]. [cited 2021 May 31]. Available from: https://www.angstromsciences.com/linear-magnetron

189. Cylindrical and Rotating Magnetron Sputtering – Vacuum Technology & Coating Blog [Internet]. [cited 2021 May 31]. Available from: https://vtcmagblog.com/cylindrical-and-rotating-magnetron-sputtering/

190. Cylindrical Magnetron – Angstrom Science Cylindrical Sputtering Magnetron [Internet]. [cited 2021 May 31]. Available from: https://www.angstromsciences.com/cylindrical-magnetron

191. Cuomo JJ, Rossnagel SM. Hollow-cathode-enhanced magnetron sputtering. Journal of Vacuum Science & Technology A. 1986 May 1;4(3):393–6.

192. Glocker DA. Principles and Applications of Hollow Cathode Magnetron Sputtering Sources. :5.

193. A history of deep brain stimulation: Technological innovation and the role of clinical assessment tools [Internet]. [cited 2021 Feb 2]. Available from: https://www.ncbi.nlm.nih.gov/pmc/articles/PMC3785222/

194. A Brief History of Materials Science & Engineering [Internet]. [cited 2021 Apr 4]. Available from: https://www.owlnet.rice.edu/~msci301/HistoryOfMS&E.htm

Appendix

Curriculum Vita

Gregory V. Taylor

EDUCATION

Rowan University, Department of Physics and Astronomy **Glassboro, NJ**

- Ph.D. in Materials Science and Engineering May 2021
  Johnson Matthey Graduate Research Assistantship

Rowan University, **Glassboro, NJ**

- B.S., Physics 2013-2015

AWARDS AND HONORS

- *Bernard Henry AIMCAL-SVC Scholarship* Dec. 2020
  Society of Vacuum Coaters Foundation

- *2019 CBP/MED Poster Award* Nov. 2019
  National Society of Black Physicists/Morgan State University

- *Brookhaven National Laboratory Award* Feb. 2015
  National Society of Black Physicists

- *NASA NJ Space Grant Consortium Fellowship* Feb. 2015
  New Jersey Space Grant Consortium

RESEARCH EXPERIENCE

Rowan University **Glassboro, NJ**
Graduate Research Assistant 2017-2021

- Synthesis and characterization of PGM oxides for neural interfacing applications.

- Reactive magnetron sputtering of Ir, Ru, Rh, and Pd binary, ternary oxides under various conditions.

- Electrochemical characterization of oxides including cyclic voltammetry, EIS, voltage transient measurements, and development of equivalent circuit models.

- Physical and morphological characterization of thin films using AFM, XRD, XRR, EDS, SEM, WD-XRF, Raman Spectroscopy, ICP, Contact Angle, Stylus Profilometry, Four-probe Resistivity using a PPMS

Signature Science LLC. Egg Harbor Twp., NJ

Department of Homeland Security: Transportation Security Laboratory 2016-2017
Associate Physicist

- Infrared flash thermography of polymers and secondary high explosives
- X-ray tomography of explosive simulants and standard materials for explosives detection.
- X-ray analysis of electron density and effective nuclear charge to identify explosive simulants
- Stress analysis of inert explosive simulants via compression testing

Thorlabs, Newton, NJ

Applications Engineer 2015-2016

- Development of experimental setups and troubleshooting of various optics and photonics parts experiments for customers, including lenses, fiber optics, and coherent sources.
- Internal development of new experimental setups with team with the goal of finding new techniques and use for new and existing equipment.

Rowan University Glassboro, NJ

Undergraduate Researcher 2015-2016

- Synthesis of thin film carbides via pulsed DC reactive magnetron and subsequent acid etching at various temperatures in a tube furnace to create porous carbon electrode supercapacitors.
- Absorption spectroscopy on various rock samples using laser induced breakdown spectroscopy (LIBS) with a Q-Pulse Nd-YAG laser system

SKILLS and TECHNIQUES

- **Physical Vapor Deposition:** DC and Pulsed DC reactive and non-reactive magnetron sputtering of Noble metals (Ir, Ru, Rh, Pd, Au, Ag), PGM (Ir, Ru, Rh, Pd) oxides, refractory metal carbides
- **Electrochemical analysis:** EIS, ECM, CV, chrono-potentiometry
- **X-ray analysis:** XRD, XRR, WD-XRF, EDX (EDS), X-Ray Tomography
- **Quantitative and qualitative surface analysis**: AFM, SEM, Contact Angle, WLI, Raman Spectroscopy

- **Other:** ICP-MS, 4-Probe resistivity, Stylus profilometry

LEADERSHIP EXPERIENCE

Rowan University College of Science and Mathematics Glassboro, NJ
Adjunct Physics Lab Instructor 2019-Present

Instructed students on introductory physics concepts including electricity and magnetism, and classical mechanics in laboratory settings

United States Air Force/United States Air Force Reserve JB-MDL,NJ
Aerial Transportation Specialist Supervisor (E-5) 2010-2018

Supervised, trained, and ensured competency of airmen. Planned and executed missions including certifying, handling, and transportation of mission critical personnel, munitions, and equipment Ensured maintenance and readiness of equipment and personnel through tracking of maintenance logs and inspections

POSTER PRESENTATION ABSTRACTS

G. Taylor, D. Jacobs, A. Marty, R. Paladines, A. Fones, H. Hamilton, S. Amini, and J. Hettinger. Electrochemical Properties of Novel Thin-Film Platinum Group Metal Oxide Solid Solutions. SVC TechCon 2021. Coatings and Processes for Biomedical Applications.

G. Taylor, D. Jacobs, A. Marty, R. Paladines, A. Fones, H. Hamilton, S. Amini, and J. Hettinger. Electrochemical Properties of Novel Thin-Film Platinum Group Metal Oxide Solid Solutions. Fall 2020 Materials Research Society Fall Meeting and Exhibit. Symposium: F.FL01: Bioelectronic Materials for Neural Interfaces—Stimulation, Sensing, Power and Packaging, F.FL01.

G. Taylor, D. Jacobs, S. Amini, J. Hettinger. Synthesis and Characterization of Reactively Sputtered Platinum Group Metal Oxides for Biomedical Applications. National Society of Black Physicists Conference 2019. NSBP 2019 CBP/MED.

G. Taylor, Z. Norris, C. Lunk, L. Yu, J. Hettinger. Role of Thermal Energy in the Conversion of Tantalum and Niobium Containing Binary Carbides to Carbide Derived Carbon. National Society of Black Physicists Conference 2015.

G. Taylor, Z. Norris, C. Lunk, L. Yu, J. Hettinger. Role of Thermal Energy in the Conversion of Tantalum and Niobium Containing Binary Carbides to Carbide Derived Carbon. NASA New Jersey Space Grant Consortium 2015.

L.G.B Camargo, B. Palazzo, G. Taylor, Z. Norris, Y. Patel, J. Hettinger, and L. Yu. “Electrochemically Synthesized CDC for Supercapacitors and Performance in Ionic Liquid Electrolytes. 227th ECS Meeting 2015.

ORAL PRESENTATION ABSTRACTS

G. Taylor, N. Page, D. Jacobs, A. Marty, R. Paladines, A. Fones, H. Hamilton, S. Amini, and J. Hettinger. Synthesis and Characterization of Reactively Sputtered Platinum Group Metal Oxides for Biomedical Applications. SVC TechCon 2019. Coatings and Processes for Biomedical Applications BT6.

G. Taylor, D. Jacobs, A. Marty, R. Paladines, A. Fones, H. Hamilton, S. Amini, and J. Hettinger. Enhancement of Electrochemical Properties of Platinum Group Metal Oxides through PVD Methods. National Society of Black Physicists Conference 2020. NSBP 2020 CMMP.

PATENTS

S. Amini, J. Hettinger, G. Taylor; Johnson-Matthey Public Limited; Thin Film Coating. WO/2020/240193. 03.12.2020.

PUBLICATIONS

P. Atsu, G. Taylor, J. Hettinger, and G. Thompson. Neurotoxicity and Cytotoxicity of Reactively Magnetron Sputtered Rhodium Oxide, Palladium Oxide, Ruthenium Oxide, and Iridium Oxide. (in preparation)

G. Taylor, D. Jacobs, S. Tint, A. Fones, H. Hamilton, and J. Hettinger. Effects of Power Density and Pulsed DC Parameters on Reactively Sputtered Iridium Oxide Thin Films Synthesized at High Oxygen Partial Pressure. (submitted)

G. Taylor, R. Paladines, A. Marti, S. Johnson, S. Tint, A. Fones, H. Hamilton, L. Yu, S. Amini, and J. Hettinger. High Performing Reactively Sputtered Rhodium Oxide, Ruthenium Oxide, and Iridium Oxide Thin Films for Neural Interfacing Applications. (Submitted)

G. Taylor, R. Paladines, A. Marti, S. Johnson, S. Tint, A. Fones, H. Hamilton, L. Yu, S. Amini, and J. Hettinger. Effect of Oxygen Partial Pressure and Chamber Working Pressure on the Properties of Palladium Oxide Thin Films for Neural Interfacing Applications. (Submitted)

M. Essner, D. Walczyk, B. Palazzo, Z. Norris, G. Taylor, J. Carroll, T. Pham, J. Hettinger, and L. Yu. Electrochemical Oxidation of Metal Carbides in Aqueous Solutions, Journal of the Electrochemistry Society. Electrochem. Soc. 165 H3107.

L.G.B Camargo, B. Palazzo, G. Taylor, Z. Norris, Y. Patel, J. Hettinger, and L. Yu. Carbide-Derived Carbon by Electrochemical Etching of Vanadium Carbides, Journal of the Electrochemistry Society. J. Electrochem. Soc. 162 H811